Development of an Electron Cyclotron Resonance Plasma Source with an Internal Antenna for Carbon Film Deposition

A dissertation submitted in partial fulfillment
of the requirements for the degree of
Doctor of Engineering

The Graduate School of Science and Engineering
Doshisha University

Camille Faith P. Romero

Kyoto, Japan
March, 2018

"Those who hope in the LORD will renew their strength.
They will soar on wings like eagles;
they will run and not grow weary, they walk and not be faint."

Isaiah 40:31

Synopsis

Development of an Electron Cyclotron Resonance Plasma Source with an Internal Antenna for Carbon Film Deposition

Camille Faith Romero

Electron cyclotron resonance (ECR) sources are of great interest in materials processing due to their capacity to produce high-density, low-ion-energy plasmas at low gas pressures. Microwave power is typically coupled to the resonance zone across a dielectric window. However, with dielectric windows, issues of contamination and accumulation of sputtered materials require frequent cleaning and maintenance of the plasma source. In addition, large-area materials processing demands for a thick dielectric window which can reduce the power transfer efficiency to the plasma. For this reason, a "windowless" high-density ECR source which couples microwave to the plasma using an internal antenna was developed in this study. Series of experiments were done to investigate the novel use of an internal antenna made of carbon material in coupling microwave power to ECR plasmas used for carbon film deposition.

The brief introduction given in chapter 1 is followed by a theoretical background in chapter 2 which covers ECR plasma excitation, microwave propagation and power absorption in magnetized plasmas. Chapter 3 gives detailed descriptions of the experimental materials and methods used to excite and evaluate the ECR plasmas.

Chapter 4 focuses on the performance of metal internal antennas in microwave coupling and ECR plasma generation. Microwave absorption was assessed by monitoring the reflected and transmitted powers simultaneously. Plasma parameters such as electron density, electron temperature and plasma potential were obtained using Langmuir probe analysis. The effects of antenna structure and configuration on plasma parameters and properties were investigated in various magnetic profiles. Good microwave coupling was obtained with insulated spiral antennas with fewer turns positioned about half the microwave free-space wavelength from the coaxial connector. Strong electrostatic coupling between the antenna and the plasma was reduced by shielding the connector and the antenna stem. Consequently, the connector shielding caused a low-density mode over a short range of magnet current, and a stable high-density mode at higher currents. The occurrence of a low-density mode is attributed to the transition of power coupling from inductive to capacitive mode.

Chapter 5 discusses the effects of experimental parameters, antenna structure and magnetic configuration on the properties of plasmas produced using carbon internal antennas. The position of the resonance zone relative to the antenna geometry was found to be the key factor that affects the plasma density and uniformity. Based on quantitative and qualitative characterizations, a coaxial-type carbon antenna demonstrates more efficient power transfer and sustains more stable and uniform plasmas, compared to a spiral-type carbon antenna.

Chapter 6 presents the performance of the ECR plasma system in hydrocarbon emission and carbon film deposition. Local-in situ diagnostics such as quadruple mass analysis (QMA) and non-invasive diagnostics like optical emission spectroscopy (OES) were used to characterize plasmas species both in ground and excited states. As observed, the ECR system requires remote plasma excitation to increase the production of

hydrocarbon radicals by chemical sputtering and reduce ion impact energy at the substrate region. The carbon coaxial antenna produced plasmas with good uniformity and sufficient CH:H and C_2:H ratios for carbon film deposition. By adding a magnetic flux return, hydrocarbon emission and plasma homogeneity were further enhanced. Carbon film was successfully formed on Si substrate by immersing a carbon target in ECR hydrogen plasma without supplying carbon precursor gas. The antenna realized stable operation for more than 5 h with 100 W input microwave power. The deposited films were characterized by using a scanning electron microscope (SEM), energy-dispersive X-ray spectroscopy (EDS) and X-ray diffraction analysis (XRD). As contamination from a tungsten heater and source chamber walls were detected in the films, additional carbon targets near these regions were installed, which had successfully reduced impurities on the subsequently formed films.

Finally, chapter 7 not only gives the general conclusions, but most importantly, provides the implications of the findings and recommendations for future works of improvement. These points can be strategically evaluated and employed for efficient film deposition using a plasma-immersed antenna made of a suitable material that serves not only as a microwave radiator but also a sputtering target.

Acknowledgements

Throughout my PhD journey, I have experienced the most difficult, humbling and mind-opening experiences (yet) in my life. I am thankful not only for all the "eureka" and "finally" moments, but most especially, for each problem and failure I have faced along the way. These experiences have molded me and taught me to endure, persevere and depend more on God – my hope and my help. I deeply appreciate all the people He had brought into my life to help me in every way.

To my sensei, Prof. Motoi Wada, I thank you for tirelessly mentoring and guiding me, and most especially for not giving up on me despite my shortcomings. Thank you for all the pieces of advice and encouragements.

I would like to thank Prof. Tadashi Ohachi for cheerfully giving your time to help me on XRD. To Prof. Mamiko Sasao, Dr. Naoki Miyamoto and Dr. Shigeo Goto, thank you for sharing me your knowledge and expertise.

To the members and alumni of Oubutsu laboratory, I am ever grateful to all of you for continually and hesitantly attending my "tetsudatte kudasai" and "onegaishimashu" every now and then. Thank you for your help.

To my dear friends, I appreciate how you have stayed with me in every situation, to cheer me up during my ups and downs. Your company "made my gray skies blue".

To my church family, your prayers and presence have been my comfort and my strength. I thank God for giving me a support group and refuge here in Japan.

To my mother and father, I am who I am because of you. I hope to honor both of you with my achievements.

Lastly, to my husband Jason, you have been the tangible love of God to me. Thank you for carrying my burdens with me, and for being there when I needed you the most.

Camille Faith P. Romero
Kyoto, Japan
March, 2018

Table of Contents

List of Tables

List of Figures

List of Abbreviations

AC	Alternating current
a-C:H	Hydrogenated amorphous carbon
CVD	Chemical vapor deposition
DC	Direct current
DSLR	Digital single-lens reflex
ECR	Electron cyclotron resonance
EDS	Energy dispersive X-ray spectroscopy
EM	Electromagnetic
FR	Flux return
LHP	Left-hand polarized
MW	Microwave
OES	Optical emission spectroscopy
PEF	Pentax electronic file
PPM	Portable pixmap format
QMA	Quadrupole mass analyzer
RF	Radio frequency
RGB	Red, Green, and Blue
RHP	Right-hand polarized
SEM	Scanning electron microscopy
TMP	Turbomolecular pump
XRD	X-ray diffraction

List of Symbols

$\boldsymbol{a}$	Acceleration (m/s^2)
A_p	Probe collecting area (m^2)
B	Magnetic field intensity (T)
$\boldsymbol{B}$	Magnetic field vector
b	Y-intercept of a line
d	Lattice spacing (Å)
D	Antenna position with respect to the flange (mm)
$\boldsymbol{E}$	Electric field vector
E_l	Left-hand polarized wave amplitude
E_r	Right-hand polarized wave amplitude
f	Frequency (Hz)
$\boldsymbol{F_L}$	Lorentz force (N)
I_B	Bohm ion current (A); Magnet current (A)
I_e	Electron current (A)
I_{esat}	Electron saturation current (A)
I_i	Ion current (A)
I_p	Probe current (A)
I_{sat}	Ion saturation current (A)
$\boldsymbol{k}$	Wave vector
k	Wave number (m^{-1})
L	Plasma dimension (m)
l_p	Exposed probe length (m)
m	Slope of a line; mass number
m_i	Ion mass (kg)
n	Plasma density (m^{-3}); number of turns; positive integer (Bragg's law)
N	Refractive index
n_c	Critical density (m^{-3})
n_e	Electron density (m^{-3})
n_i	Ion density (m^{-3})
p	Pressure (Pa)
P	Power (W)
P_f	Forward power (W)
P_{inc}	Incident power (W)
p_{min}	Minimum pressure
P_r	Reflected power (%)

q	Ion charge (C)
R	Resistance (Ω)
r_p	Probe radius (m)
T_e	Electron temperature (V)
T_{eK}	Electron temperature (K)
T_i	Ion temperature (V)
T_{iK}	Ion temperature (K)
u_B	Bohm velocity
V_f	Floating potential (V)
$\boldsymbol{v}$	Velocity of electron
$\bar{v}$	Electron average speed (m/s)
V_p	Probe voltage (V)
V_{pl}	Plasma potential (V)
V_s	Source voltage (V)
z	Charge number
z_{res}	Axial distance of the ECR zone from the antenna
δ	Skin depth (m)
ϵ	Relative permittivity
η	Efficiency factor
θ	Diffraction angle (°)
λ	Mean free path; wavelength (m)
λ_D	Debye length (m)
ν	Frequency of emitted photon (Hz)
ω	Radian wave frequency (rad/s)
ω_{ce}	Electron cyclotron frequency (rad/s)
ω_{ci}	Ion cyclotron frequency (rad/s)
ω_l	Left-hand cutoff (rad/s)
ω_{lh}	Lower hybrid frequency (rad/s)
ω_{pe}	Electron plasma frequency (rad/s)

List of Constants

Atomic mass unit	u	1.6605×10^{-27} kg
Boltzmann constant	k_B	1.3807×10^{-23} eV/K
Electron charge	e	1.6022×10^{-19} C
Electron mass	m_e	9.1095×10^{-31} kg
Permittivity of free space	ϵ_0	8.8542×10^{-12} F/m
Pi	π	3.1416
Planck's constant	h	6.6261×10^{-34} J s
Proton mass	M	1.6726×10^{-27} kg
Speed of light	c	2.9979×10^{8} m/s

Chapter 1

Background of the Study

1.1 Introduction

In the presence of a static magnetic field, electrons gyrate around the field lines due to the effect of the magnetic force. When the gyration frequency of the electrons is equal to the incident wave frequency, which is usually 2.45 GHz microwave, an *electron cyclotron resonance* (ECR) occurs. Because of this resonance, the electrons gain sufficient energy which allows ionization of a background gas. The efficient transfer of wave energy by resonant wave-particle interaction results in the production of high-density plasma.

Over the last several decades, plasma sources based on ECR technology have been extensively studied and used in plasma generation and processing. ECR technology was first applied in plasma generation in early 1960s for plasma fusion and acceleration researches. [1,2] The initial attempts to apply ECR technology in plasma materials processing were done in mid-1970s for silicon oxidation and etching. [3,4] However, during the next decade, ECR was used mainly for plasma fusion applications. In early 1980s, an ECR plasma source modified for plasma-enhanced chemical vapor deposition (PECVD) of thin films was introduced.[5] Since then, ECR plasma sources have been used for deposition of various materials such as carbon thin films, silicon dioxide films, boron nitride coatings, gallium arsenide, and metal oxide films.[6-11]

1.2 Motivations for the Study

Since the invention of high-power microwave generators in World War II, microwave-induced plasmas have been successfully produced. The use of ECR technology in microwave plasma sources allowed the production of high-density, low-ion-energy plasmas at low gas pressures. If the plasma density is sufficiently high, deposition rates can be increased. Moreover, if the ion energy is sufficiently low, damage to the sample can be prevented. Due to these unique properties of ECR plasmas, they are widely used in diamond-like, amorphous carbon and diamond thin film deposition.[12,13]

The incident microwave in ECR plasma sources is commonly launched into the vacuum chamber across a dielectric window to reduce the plasma sheath voltage. However, the use of dielectric windows in a plasma reactor has several disadvantages. Firstly, large-area materials processing requires wide and very thick dielectric window which is not only expensive to fabricate, but also reduces the power transfer efficiency between the microwave applicator and the plasma.[14] Second, the dielectric material is easily sputtered by the electrostatic coupling between the applicator and the plasma, resulting in impurities.[15] Lastly, when ECR systems are utilized for deposition of conductive thin layers, such as carbon films, ions and atoms tend to condense on the vacuum-side of the dielectric window reducing its transmittance efficiency over time.[16] The degradation of and deposition on the window requires frequent cleaning and maintenance cycles.[17]

Several techniques were done to avoid the disadvantages of dielectric windows. One idea is to transmit microwaves from both sides of the plasma chamber using a branched waveguide.[11] Although sputtered atoms that end up on the dielectric window are considerably reduced, the window still becomes covered with contaminants after long period of operation. This requires dismounting and reassembling of the loop waveguide,

which is fairly time-consuming. Therefore, further research and development of alternative methods and materials to overcome such obstacles and inconveniences are needed to be done.

1.3 Objectives of the Study

One way to exclude dielectric windows and complex waveguide systems from an ECR plasma source is to introduce power into the chamber through an internal antenna. Internal antenna is a type of antenna placed inside the vacuum chamber. As oppose to an external antenna, it does not have to be placed behind a dielectric window and is exposed directly into the plasma space. Internal antennas of different structures were developed and successfully used in ECR plasma sources for deposition and etching applications.[18-20] The antennas had transferred power into the ECR discharges efficiently. However, the antennas were subject to sputtering and could introduce impurities into the deposition plasma. Though insulating the internal antennas can reduce impurities, the insulating material inevitably becomes source of contaminants as it is still subject to sputtering. Therefore, it is strategic to cover the internal antenna with the same material being deposited. To explore such possibility, this study aims to develop and optimize a plasma source which couples microwave power to ECR plasmas using a carbon internal antenna for carbon film deposition. Firstly, the performance of metal and carbon internal antennas in power coupling and plasma excitation are tested. Secondly, the effects of experimental parameter, antenna structure and magnetic configuration on the plasma properties are investigated. And lastly, the performance of the ECR plasma source with an internal antenna in hydrocarbon emission and carbon film deposition are evaluated using qualitative and quantitative diagnostics.

Chapter 2

Principles of ECR Plasma Excitation

2.1 Introduction

Plasma is loosely defined as an ionized gas. However, since any gas has some small degree of ionization, it is more specific to define plasma as a quasineutral gas consisting of charged and neutral particles which exhibits collective behavior. Plasma is quasineutral in a sense that it is neutral enough to consider a common density for oppositely charged particles, $n \simeq n_i \simeq n_e$, where n, n_i and n_e are plasma, ion and electron densities, respectively. However, it is not so neutral that all significant electromagnetic forces vanish. [21]

In a gas, the dynamics of motion are determined by forces between its local regions. On the other hand, plasma behaves "collectively" in such a way that its motions depend not only on the local conditions but also on the condition of plasma in remote regions. The charge separation between ions and electrons produces electric fields, and current of charged particles produces magnetic fields. These electromagnetic fields give rise to an "action at a distance" effect in the plasma.[22]

In order to produce plasma, sufficiently high energy is needed to initiate ionization in which electrons are released from neutral atoms producing ions and free radicals. Required energy can be in a form of radiation, electric fields or caloric energy. Plasmas

lose energy to their surroundings by collision, diffusion and radiation processes; hence to sustain the plasma, there should be equilibrium between ionization and loss rates.

This study deals with weakly ionized plasma discharges in which the plasma density is only a small fraction of the neutral gas density. This type of plasma has the following features:[17]

1. They are driven electrically.
2. Charged particle collisions with neutral particles are important.
3. There are boundaries at which surface losses are important.
4. Ionization of neutrals sustains the plasma in the steady state.
5. The electrons are not in thermal equilibrium with the ions.

Sources that produce high-density plasmas are introduced in the next section. One of them is the electron cyclotron resonance (ECR) plasma source of which the characteristics and fundamentals are discussed in the succeeding sections.

2.2 High-density Plasma Sources

The need for high-density and low-pressure discharges for materials processing have led to the development of high-density plasma sources such as electron cyclotron resonance (ECR), helicon, helical resonant and inductive coupled sources. They are typically ignited and sustained by AC sources such as radio frequency (RF) (f = 13.56 MHz) and microwave frequency (f = 2450 MHz) sources.[17] The oscillating electric field of AC sources accelerates free electrons into simultaneous periodic oscillations. In this process, electrons collide with gas molecules randomly in which electrons gain sufficient energy to cause bond dissociation and ionization by picking up an increment of energy with each collision.[23] Typical parameters of high-density plasma compared to capacitively coupled RF discharges are shown in Table 2.1.

Table 2.1 Range of parameters of high-density and capacitively coupled plasmas (after Ref. 17).

Parameter	High-density plasma	Capactively coupled plasma
Pressure p (mTorr)	0.5–50	10–1000
Power P (W)	100–5000	50–2000
Frequency f (MHz)	0–2450	0.05–13.56
Magnetic field B (kG)	0–1	0
Plasma density n (cm^{-3})	10^{10}–10^{12}	10^{9}–10^{11}
Electron temperature T_e (V)	2–7	1–5

Typical configurations of high-density plasma systems are illustrated in Fig. 2.1. In these sources, RF or microwave power is commonly coupled to the plasma across a dielectric window for noncapacitive power transfer, but they differ in the means by which power is coupled to the plasma. ECR and helicon sources are commonly driven by microwave and RF power, respectively. Under an axial magnetic field, these sources

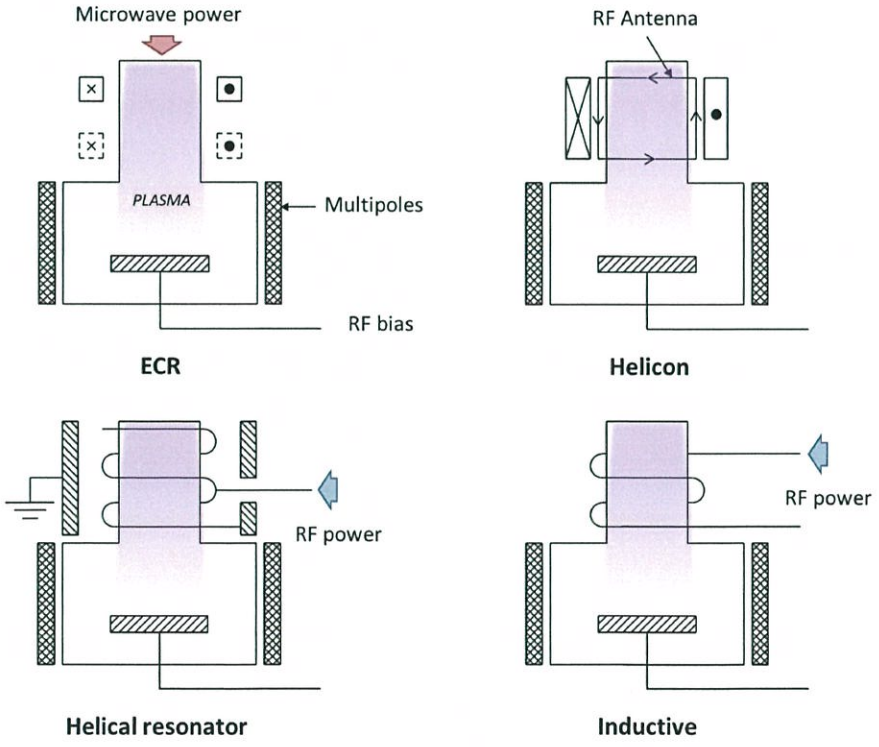

Fig. 2.1 Configurations of some high-density sources (after Ref. 17).

transfer the wave energy to the plasma by resonant wave-particle interaction. On the other hand, external magnetic field is not required in helical resonator and inductive sources. Helical resonator sources couple RF power to the plasma by exciting a resonant axial mode in a slow wave structure. Inductive coupled sources have RF coils around the dielectric source chamber, similar with helical resonator sources, which induce plasma coupling by transformer action.[17]

2.3 ECR Plasma Characteristics

If the radian frequency of an incident wave and the electron cyclotron (gyration) frequency are denoted by ω and ω_{ce}, respectively, then electron cyclotron resonance (ECR) occurs when $\omega = \omega_{ce}$. The frequencies ω and ω_{ce} are given by:

$$\omega = 2\pi f \tag{2.1}$$

$$\omega_{ce} = \frac{eB}{m_e} \tag{2.2}$$

where e, B, and m_e as the electron charge, magnetic field intensity, and electron mass, correspondingly. The commonly used microwave frequency is 2.45 GHz since magnetron sources are inexpensive and commercially available at that frequency. For f = 2.45 GHz, the wave absorption requires an external magnetic field of intensity B = 87.5 mT. The applied magnetic field produces a resonance zone in the discharge where electrons are accelerated and absorb about 95% of the microwave power.[24] The effective absorption of microwave power in the resonance zone ensures energy transfer to the electrons without depending much on collisions, which allows operation at low gas pressure. Such collisionless heating mechanism of ECR excitation produces plasma with low sheath voltage. When the sheath voltage is low, the bombarding energies of ions flowing to the substrate are also low.[17]

The presence of magnetic field not only promotes high power absorption but also allows operation at high-density plasma. Introduction of microwaves at high magnetic field region, $\omega_{ce} > \omega$, allows wave propagation even in *overdense* plasma with electron plasma frequency $\omega_{pe} > \omega$, and with electron density $n_e > n_c$ (critical density). ω_{pe} and n_c are given by,

$$\omega_{pe} = \sqrt{\frac{e^2 n_e}{m_e \epsilon_o}} \tag{2.3}$$

$$n_c = \frac{m_e \epsilon_0 \omega^2}{e^2} \tag{2.4}$$

where ϵ_o is the permittivity of free space. Unlike ECR plasmas, unmagnetized plasmas such as inductive coupled discharges have a density limit, $n_e \lesssim n_c$, for good field penetration and efficient power transfer to the plasma.[17] Deposition, sputter and etch rates can be substantially rapid if the plasma density is sufficiently high. Consequently, ECR plasma sources are widely used in laboratories and industries for materials processing due to the following characteristics:

1. They can operate at low gas pressures.
2. They produce plasmas with low ion energy.
3. They can operate at high plasma density range.

2.4 ECR Plasma Source Configurations

An ECR system is usually divided into two regions: the source chamber where most of the plasma production occurs, and the process chamber where the substrate is located. The chambers are typically made of stainless steel or aluminum. Shown in Fig. 2.2 is a typical ECR source configuration with high-aspect ratio, $l > r$, where l and r are the length and radius of the source chamber, respectively. Microwaves are introduced into the source chamber across a dielectric window along the divergent magnetic field. High field

intensity, $\omega_{ce} > \omega$, is needed near the dielectric window so that microwaves can propagate in the plasma and be absorbed in the resonance zone, where $\omega_{ce} \approx \omega$. The steady-state magnetic field is produced by one or more electromagnets surrounding the source chamber. A strong permanent magnet can also be used to generate a divergent axial magnetic field instead of electromagnets.

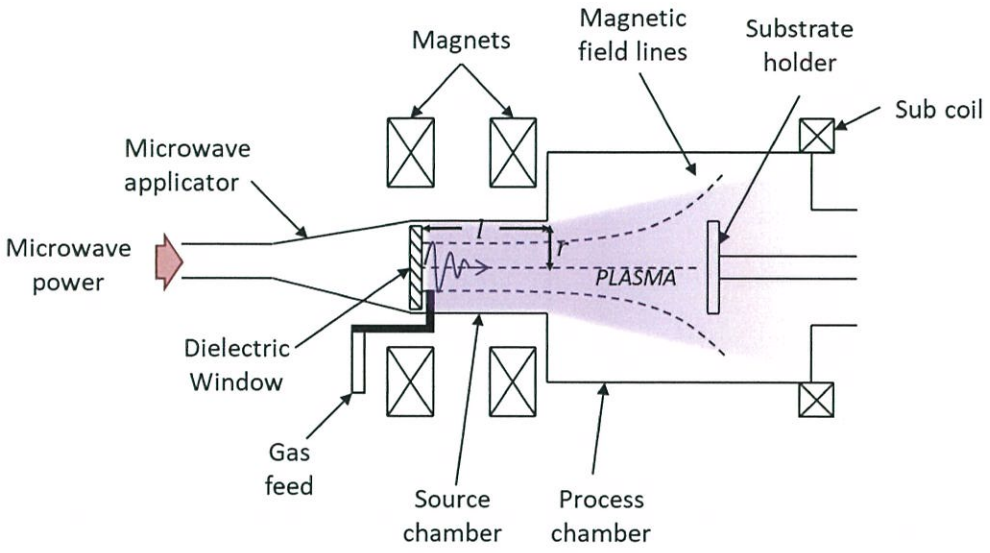

Fig. 2.2 A typical high-aspect ratio ECR configuration with divergent magnetic field (after Ref. 25).

As gas is introduced into the chamber, it breaks down and a plasma discharge forms. The plasma diffuses along the magnetic field lines into the process chamber where the substrate is located. Occasionally, electromagnets are added around the process chamber to modify plasma density and uniformity.[17,25]

Typical variations of ECR source configuration are illustrated in Fig. 2.3. In these configurations, microwave power is commonly coupled to the resonance zone across a dielectric window. High-aspect ratio system, shown in Fig. 2.3a, has its source region far from the substrate. The expansion of the plasma from the resonance zone to the substrate reduces ion flux and increases ion impact energy. To decrease plasma expansion, low-aspect ratio system had been developed (Fig. 2.3b) of which the resonance zone is within

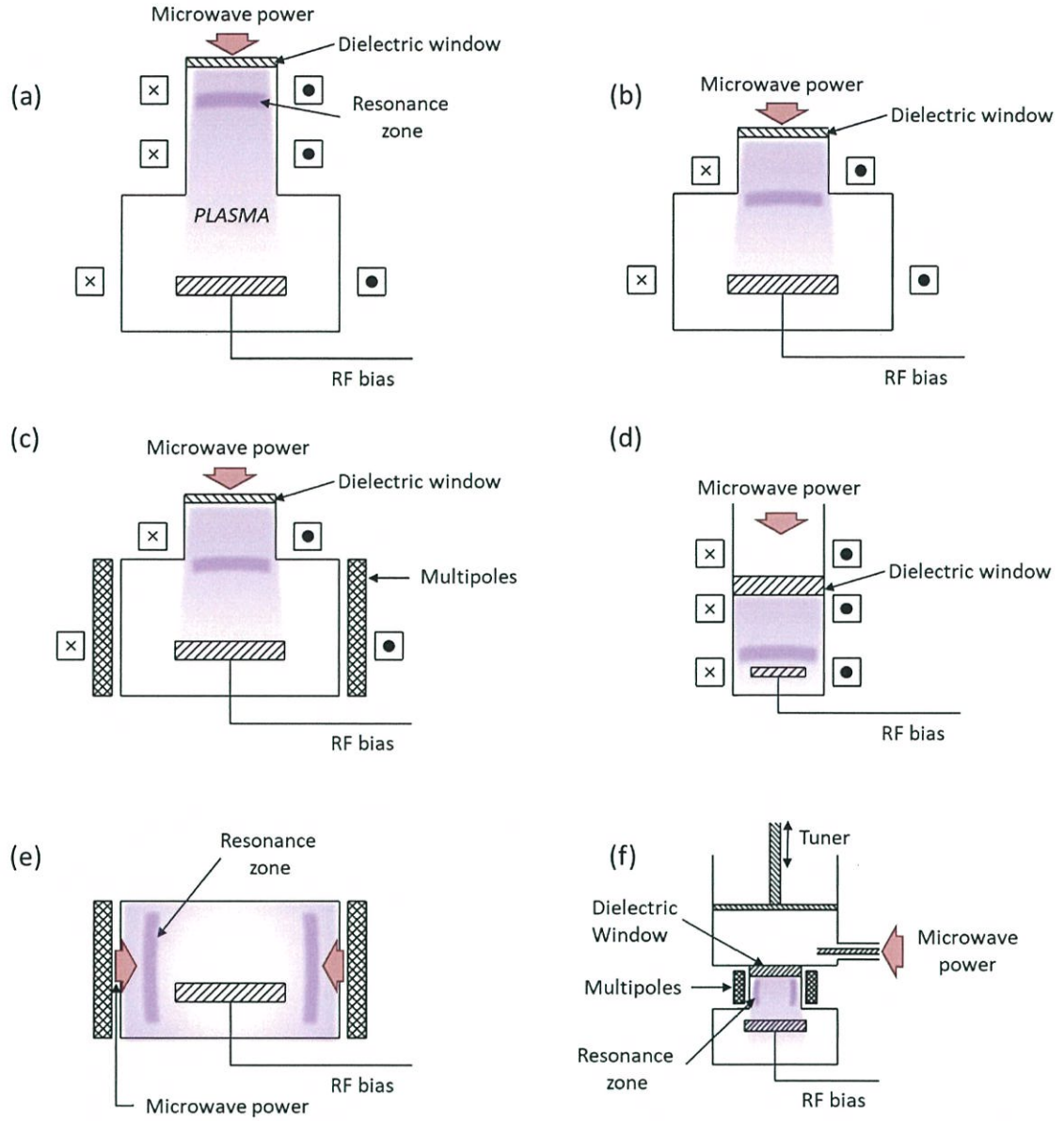

Fig. 2.3 Typical ECR configurations such as (a) high-aspect ratio, (b) low-aspect ratio, (c) low-aspect ratio with multipoles, (d) close-coupled, (e) distributed electron cyclotron resonance(DECR) and (f) microwave cavity excited (after Ref. 17).

the process chamber. Substrate holders are typically connected to an RF bias supply to control the energy of the bombarding ions on the substrate.

By adding linear multipole permanent magnets around the process chamber, as shown in Fig. 2.3c, the plasma density can be increased and the plasma uniformity can be further improved. Another way of improving the uniformity and density is to combine the

source and process chamber and position the resonance zone close to the substrate. Such configuration is called the close-coupled type of low-aspect ratio system (Fig. 2.3d).[17]

In the configurations described earlier, microwaves with direction of propagation $\boldsymbol{k}$ are introduced along the magnetic field vector $\boldsymbol{B}$ (wave vector $\boldsymbol{k} \parallel \boldsymbol{B}$), on the other hand, microwaves in the distributed ECR (DECR) configuration, shown in Fig. 2.3e, are injected perpendicular to $\boldsymbol{B}$ ($\boldsymbol{k} \perp \boldsymbol{B}$). In DECR, several microwave applicators are placed around the process chamber creating linear resonance zones near the chamber wall. Similar linear resonance zones are generated in the microwave cavity source shown in Fig. 2.3f, where a sliding short and a stub tuner on top and on the side, respectively, are used to tune the coaxial feed, which excites standing waves in the chamber.[17]

2.5 ECR Heating

The basic principle of ECR heating of electrons is illustrated in Fig. 2.4. Consider an incident microwave in sinusoidal steady state propagating along $\hat{z}$ and polarized along $\hat{x}$,

$$\boldsymbol{E}(\boldsymbol{r}, t) = Re\, \hat{x} E_x(\boldsymbol{r}) e^{j\omega t} \tag{2.5}$$

where the complex amplitude E_x is taken to be a pure real value. A linearly polarized wave can be decomposed into sum of two counter-rotating circularly polarized waves, as

$$\hat{x}E_x = (\hat{x} - j\hat{y})E_r + (\hat{x} + j\hat{y})E_l \tag{2.6}$$

where $\hat{x}$ and $\hat{y}$ are unit vectors along x and y-axes, and where E_r and E_l are the amplitudes of the right-hand polarized (RHP) and left-hand polarized (LHP) waves, with

$$E_r = E_l = \frac{E_x}{2} \tag{2.7}$$

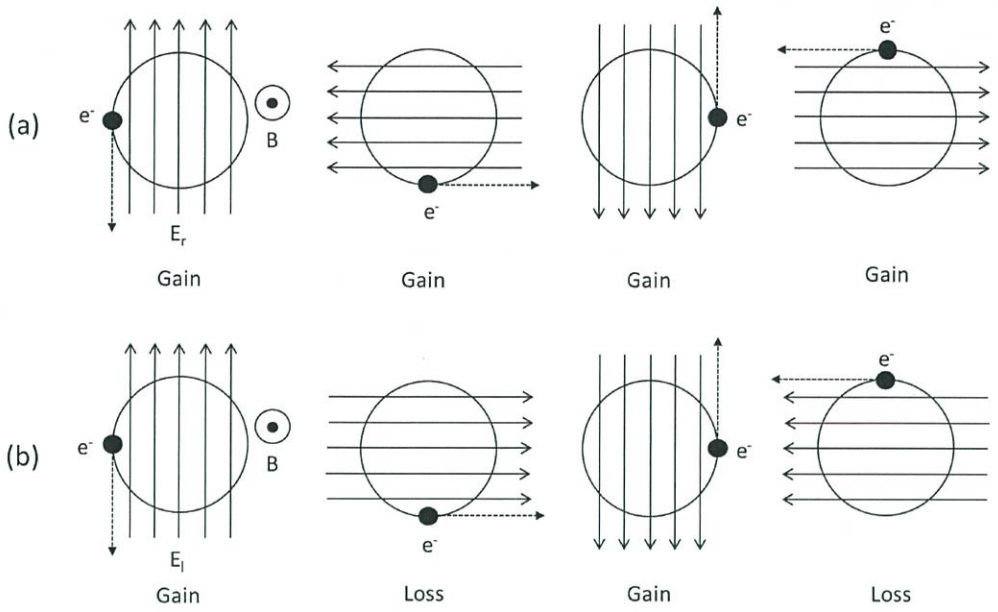

Fig. 2.4 Basic principle of ECR heating where there is (a) a continuous energy gain for RHP and (b) an oscillating energy for LHP waves (after Ref. 17).

The $\boldsymbol{B}$ vector The $\boldsymbol{E}$ vector of RHP and LHP waves rotate in right-hand and left-hand sense with respect to $\boldsymbol{B}$ at frequency ω, correspondingly. At the same time, electrons gyrate in right-hand sense at frequency ω_{ce} with respect to $\boldsymbol{B}$. Based on *Lorentz force* given by,[26]

$$\boldsymbol{F}_L = -e\boldsymbol{E} + (-e\boldsymbol{v} \times \boldsymbol{B}) \tag{2.8}$$

where **v** is the instantaneous velocity of an electron, the electric field of the resonant RHP wave exerts a force $-eE_r$ on the electron, as shown in Fig. 2.4a. It accelerates the electron along its circular orbit, resulting in a continuous transverse energy gain. Conversely, the LHP wave field, in Fig. 2.4b, produces an oscillating force of which the time average is zero, resulting in no energy gain.[17]

2.6 Microwave Propagation in Plasma

The following sections discuss how microwave propagation in plasma, unmagnetized or magnetized, depends on plasma density and magnetic field.

2.6.1 Propagation in Unmagnetized Plasma

As wave propagates through a dielectric medium, such as plasma, its phase velocity changes depending upon its wavelength. Such phenomenon is called *dispersion*. The effect of dispersion on wave properties is defined by a *dispersion relation*, which expresses wave frequency ω as a function of wave number k. This equation can be derived by substituting a plane wave solution into a wave equation, which is obtained from the Maxwell's equations. In unmagnetized plasma, the dispersion relation is,[27]

$$\omega^2 = \frac{c^2k^2}{\epsilon} = \omega_{pe}^2 + c^2k^2 \tag{2.9}$$

where c is the speed of light and ϵ is the relative permittivity of plasma given by,

$$\epsilon = 1 - \frac{\omega_{pe}^2}{\omega^2} \tag{2.10}$$

The refractive index N of a dispersive medium is defined as,

$$N^2 = \frac{c^2k^2}{\omega^2} \tag{2.11}$$

thus, from Eqs. (2.9) and (2.10),

$$\epsilon = 1 - \frac{\omega_{pe}^2}{\omega^2} \equiv N^2 \tag{2.12}$$

Equation (2.10) had been derived assuming that ions are infinitely massive, the collision frequency is zero and that electrons have no thermal motion. The incident wave propagates in the plasma only if N is real, hence, only when $\omega > \omega_{pe}$, otherwise, the wave is reflected on the boundary of the overdense plasma.[28] This leads to a critical density n_c given by Eq. (2.3). For an incident microwave with f = 2.45 GHz to be able to propagate in plasma, the electron density n_e should be less than 7.5×10^{16} m^{-3}. However, in the presence of a magnetic field, the situation is significantly changed. Magnetized plasma can support many wave modes that allow wave transmission even in dense plasmas. In the following sections, we will only discuss the properties of *principal* waves, which are

waves traveling parallel and perpendicular to $\boldsymbol{B}$, and only consider electron motions, taking the ions to be fixed, which is basically a cold plasma approximation.[27]

2.6.2 Propagation Parallel to Magnetic Field ($k \parallel B$)

For a wave propagating primarily along a steady-state magnetic field, the dispersion relation can be separated into a right-hand polarized (RHP) wave or *r* wave mode,

$$N_r^2 = 1 - \frac{\omega_{pe}^2}{\omega(\omega - \omega_{ce})} \tag{2.13}$$

and a left-hand polarized (LHP) wave or *l* wave mode:

$$N_l^2 = 1 - \frac{\omega_{pe}^2}{\omega(\omega + \omega_{ce})} \tag{2.14}$$

where ω_{ce} is defined to be explicitly positive. For *r* mode, $\boldsymbol{E}$ rotates in the same direction as the electron gyrate about $\boldsymbol{B}$, and opposite for the *l* mode. Based on Eqs. (2.13) and (2.14), the direction of rotation of $\boldsymbol{E}$ is independent of the sign of *k*. Thus, the polarization of $\boldsymbol{E}$ is not defined with respect to the direction of propagation $\boldsymbol{k}$ but on the direction of magnetic field $\boldsymbol{B}$.[21]

As wave propagates in plasma, it passes through regions with different ω_{pe} and ω_{ce}, where it may encounter *resonances* and *cutoffs*. A wave is generally absorbed at a resonance and reflected at a cutoff. A resonance occurs in plasma when $N \to \infty$; that is, when the wave number $k \to \pm\infty$. On the other hand, a cutoff occurs when $N \to 0$; that is, when $k \to 0$. For *r* wave, *N* becomes infinite when $\omega = \omega_{ce}$, which pertains to electron cyclotron resonance described in section 2.3. On the other hand, *l* wave does not have a resonance for positive ω. If ion motions were considered, the *l* wave rotates in the same direction as the ion gyrates about $\boldsymbol{B}$ and would have been found to have resonance at the ion cyclotron frequency ω_{ci}, given by,

$$\omega_{ci} = \frac{eB}{M} \tag{2.15}$$

with M as the proton mass. The cutoff frequencies are obtained by setting $k = 0$,

$$1 - \frac{\omega_{pe}^2}{\omega(\omega \mp \omega_{ce})} = 0 \tag{2.16}$$

Solving for ω, we obtain the cutoff of r wave,

$$\omega_r = \frac{\omega_{ce} + \sqrt{\omega_{ce}^2 + 4\omega_{pe}^2}}{2} \tag{2.17}$$

and the cutoff of l wave,

$$\omega_l = \frac{-\omega_{ce} + \sqrt{\omega_{ce}^2 + 4\omega_{pe}^2}}{2} \tag{2.18}$$

ω_r is higher than ω_l, such that ω_r is an upper cutoff frequency above ω_{pe} and ω_{ce}, and ω_l is a lower cutoff frequency below ω_{pe}. We should, however, be careful with very low frequencies where ion dynamics may be important.[17]

When the frequency of the incident wave ω is less than ω_{ce}, the r wave is referred to as the whistler wave, which propagates even in high-density plasmas, where $\omega < \omega_{pe}$. The whistler mode is used as the basis for some of the common ECR configurations (see section 2.4), which rely on a *magnetic beach* absorption, where low-frequency microwaves propagate from higher to lower magnetic field to the ECR zone.

2.6.3 Propagation Perpendicular to Magnetic Field ($k \perp B$)

For a wave propagating perpendicular to $\boldsymbol{B}$, it can either have its $\boldsymbol{E}$ vector parallel or perpendicular to $\boldsymbol{B}$, as shown in Fig. 2.5. If $\boldsymbol{E}$ is parallel to $\boldsymbol{B}$, ($\boldsymbol{E} \parallel \boldsymbol{B}$), it corresponds to a linearly polarized wave electric field lying along the magnetic field, so that the electron motion it induces is unaffected by $\boldsymbol{B}$. Such wave is called the *ordinary* (o) wave, and its dispersion relation is identical to that in unmagnetized plasma given by Eq. (2.9).

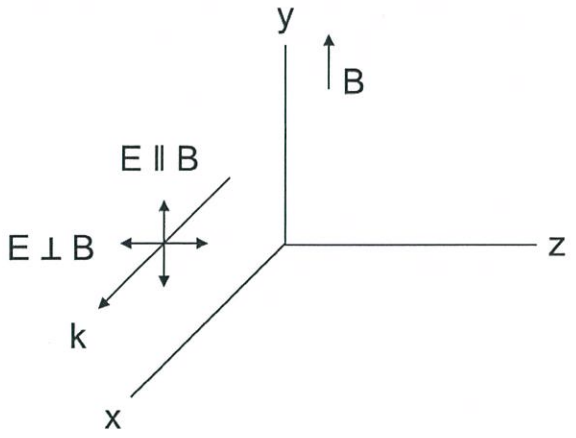

Fig. 2.5 Geometry for electromagnetic waves propagating perpendicular to $\boldsymbol{B}$ (after Ref. 21).

If $\boldsymbol{E}$ is perpendicular to $\boldsymbol{B}$, ($\boldsymbol{E} \perp \boldsymbol{B}$), the wave is then called the *extraordinary* (x) wave, where the electron motion is affected by $\boldsymbol{B}$. The dispersion relation for x wave is given by,

$$N_x^2 = \frac{c^2k^2}{\omega^2} = 1 - \frac{\omega_{pe}^2}{\omega^2}\frac{\omega^2 - \omega_{pe}^2}{\omega^2 - \omega_{uh}^2} \tag{2.19}$$

where ω_{uh} is the upper hybrid frequency:

$$\omega_{uh}^2 = \omega_{pe}^2 + \omega_{ce}^2 \tag{2.20}$$

The x wave is partly transverse and partly longitudinal electromagnetic wave; that is, $\boldsymbol{E}$ has components both parallel and perpendicular to $\boldsymbol{k}$, such that $\boldsymbol{E}$ traces out an eclipse in the xy plane.[27]

By setting $k = \infty$ in Eq. (2.19), it can be observed that the resonance of x wave occur at $\omega = \omega_{uh}$. As a wave with frequency ω approaches a resonance region, both its phase and group velocities approach zero, and the wave energy is converted into upper hybrid oscillations.[21] If ion dynamics are considered, a second resonance occur at the lower hybrid frequency ω_{lh}, given by,

$$\frac{1}{\omega_{lh}^2} \approx \frac{1}{\omega_{pi}^2} + \frac{1}{\omega_{ce}\omega_{ci}} \qquad \text{for } \omega_{ci} \ll \omega_{pi} \tag{2.21}$$

where ω_{pi} is the ion plasma frequency.

The cutoffs for x wave are found by setting $k = 0$ and then solving for ω. We then obtain the same equations, (2.17) and (2.18), as we had for the cutoffs of r and l waves.[17]

To summarize, the resonances, cutoffs and polarizations of the principal waves are listed in Table 2.2. The dispersion diagram for the principal waves in magnetized plasma is illustrated in Fig. 2.6, considering only the electron motion in this case. The diagram, however, is similar with the case with mobile ions for frequencies above the lower cutoff. Near the lower cutoff and below, the motion of ions can follow the periodic changes in $\boldsymbol{E}$, such that the incident waves are strongly modified by the ion dynamics.

Some of the important features of the dispersion diagram are: [21,17]

1. The RHP (r) wave has two regions of propagation separated by a stop band. First, the region where $\omega < \omega_{ce}$ (whistler mode), and second, the region where $\omega > \omega_r$.
2. The extraordinary (x) wave has also two regions of propagation separated by a stop band. First, the region between ω_l and ω_{uh}, and second, the region above ω_r.
3. As r wave reaches the resonance at $\omega = \omega_{ce}$, the phase and group velocities becomes zero ($k \rightarrow \infty$), which is due to the strong absorption of the wave energy in the resonance zone.
4. Similar phenomenon occurs for the x wave at the upper hybrid resonance, represented by the horizontal line at $\omega = \omega_{uh}$.
5. The LHP (l) wave behaves like the ordinary (o) wave except that the cutoff occurs at ω_l instead of ω_{pe}.

Table 2.2 Summary of Resonances and Cutoffs of the Principal Waves (after Ref. 21,17).

Wave	Resonances ($k = \infty$)	Cutoffs ($k = 0$)	Polarization
r wave	$\omega = \omega_{ce}$	$\omega_r = \dfrac{\omega_{ce} + \sqrt{\omega_{ce}^2 + 4\omega_{pe}^2}}{2}$	right-hand circularly polarized
l wave	$\omega = \omega_{ci}$	$\omega_l = \dfrac{-\omega_{ce} + \sqrt{\omega_{ce}^2 + 4\omega_{pe}^2}}{2}$	left-hand circularly polarized
x wave	$\omega_{uh}^2 = \omega_{pe}^2 + \omega_{ce}^2$ $\dfrac{1}{\omega_{lh}^2} \approx \dfrac{1}{\omega_{pi}^2} + \dfrac{1}{\omega_{ce}\omega_{ci}}$	Both as above	elliptically polarized
o wave	none	$\omega = \omega_{pe}$	linearly polarized

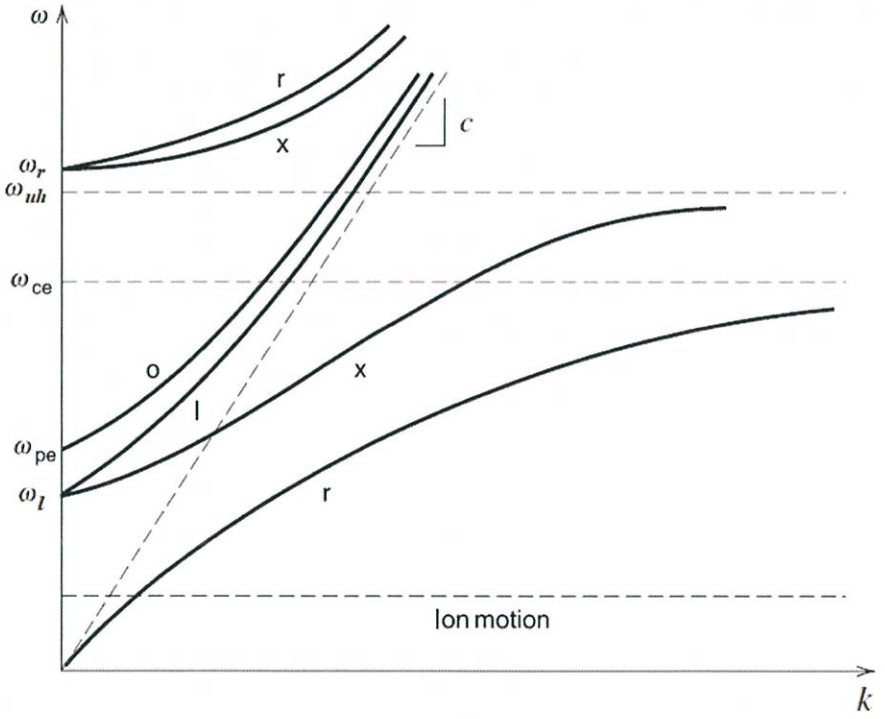

Fig. 2.6 Dispersion ω versus k for the principal waves in magnetized plasma for $\omega_{ce} > \omega_{pe}$, excluding ion motions (after Ref. 17).

2.7 Microwave Absorption in ECR sources

When microwaves propagate in magnetized plasmas, they can be completely or partially damped by various dissipative mechanisms, such as:[29]

1. Heating of electrons and ions with successive loss of their energy in elastic and inelastic collisions.
2. Diffusive loss of heated electrons and ions to plasma boundaries.
3. Transformation of microwaves into other waves that are absorbed in the plasma or reflected back or that propagate to the substrate area.

In ECR plasmas, the dominant power dissipation mechanism is through electron cyclotron heating in the resonance zone. The efficiency of microwave absorption in the resonance zone is dependent on experimental parameters such as pressure and incident power, as illustrated in Fig. 2.7. The boundaries are based on the solutions of the wave propagation through the resonance zone obtained by Budden.[30] The efficiency factor is

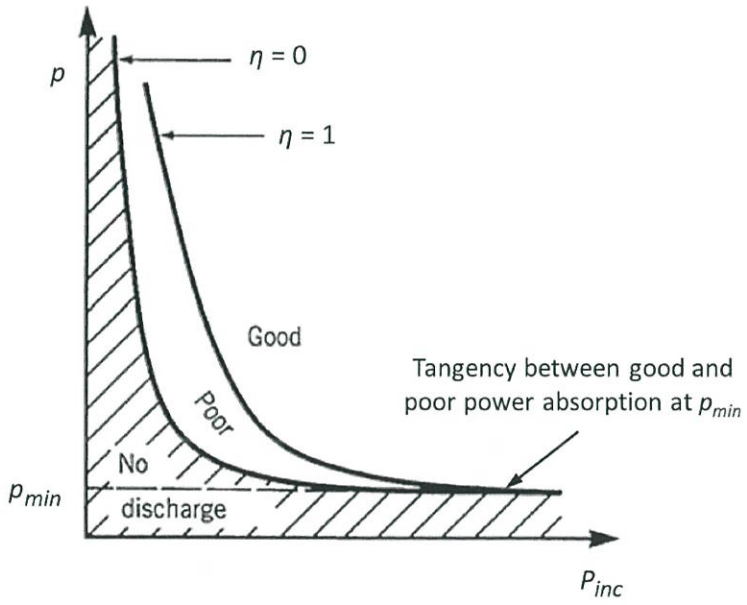

Fig. 2.7 Experimental parameters for good ECR source operation: pressure p versus incident power P_{inc} (after Ref. 17).

denoted by η, such that the region at which $\eta \geq 1$ signifies good power absorption. For parameters inside this region, the incident microwave power is efficiently absorbed over the entire cross section of the resonance zone. Operation outside this region results in large microwave power transmission into the main chamber. For good power absorption, a minimum pressure p_{min} is needed as in the case for an inductive discharge, in which there is a tangency between power absorbed and power lost versus density, at low density. Similar to inductive discharges, the plasma does not turn off immediately at the minimum pressure; instead, it exhibits transition to a considerably lower density state. At pressures below p_{min}, the plasma discharge extinguishes.[17]

Microwaves reflected in the plasma chamber can generate interference of waves that can greatly affect the power absorption. The variation of axial plasma density can cause upstream power reflection. In addition, radial density and magnetic field variations can cause microwave refraction, which may lead to a self-focusing effect to the microwave power profile as the wave propagates to the resonance zone.[17]

Chapter 3

Experimental Setup & Diagnostics

An electron cyclotron resonance plasma system with high-aspect ratio has been developed for carbon film deposition. Microwave power is coupled to the resonance zone using an internal antenna. The device utilizes a graphite sputtering target immersed in hydrogen plasma to supply hydrocarbon through ECR sputtering process. The succeeding sections give detailed description of the ECR sputtering system used in the experiment, followed by the diagnostics employed in this study and the principles behind them.

3.1 ECR Plasma System

The actual image and schematic diagram of the ECR plasma system utilized in this study are shown in Fig. 3.1 and Fig. 3.2, respectively. It consists of a vacuum system, microwave power and DC bias supplies, magnets, a gas injection unit, source and process chambers, a water-cooling system and plasma diagnostic equipment. The vacuum chamber and pumps are mounted on a stainless steel support frames with vibration damping pads underneath. The chamber walls are connected to the ground. In total, the system is about 1.10-m long, 0.50-m wide and 1.10-m high.

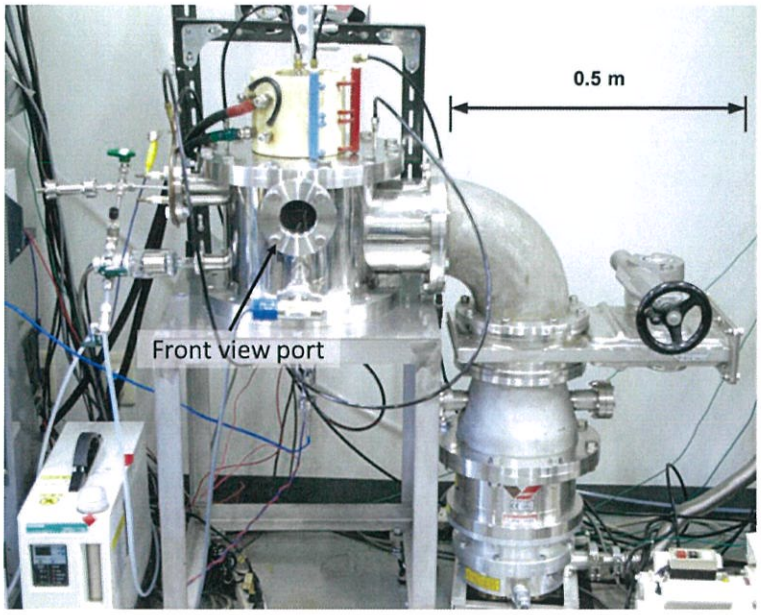

FRONT VIEW

Fig. 3.1 Photo of the experimental ECR plasma system

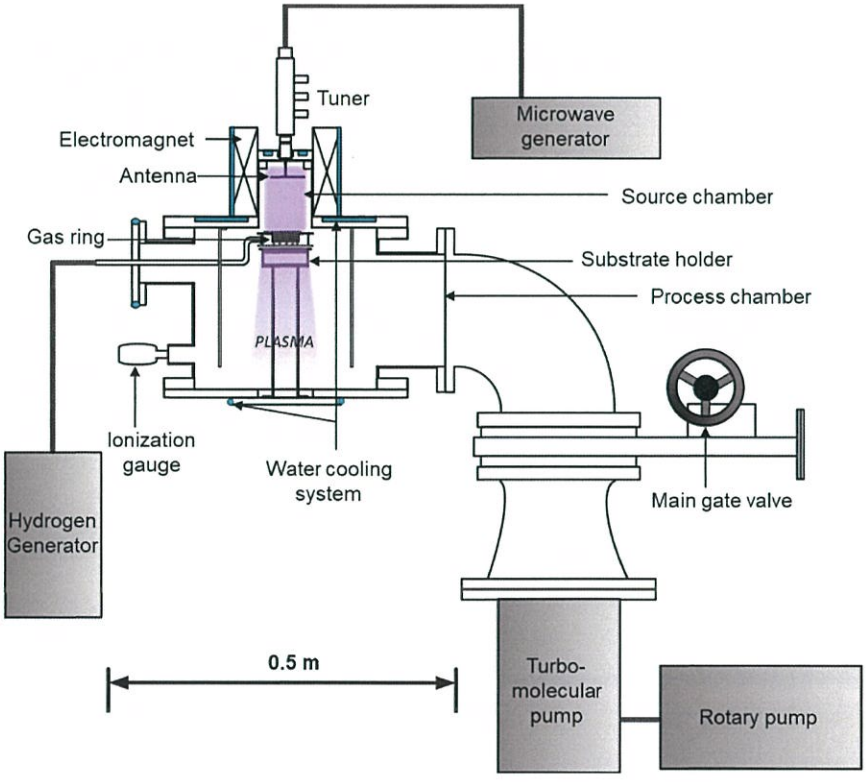

FRONT VIEW

Fig. 3.2 Schematic diagram of the experimental ECR plasma system

3.1.1 Vacuum System

The source and process vacuum chambers were evacuated by a rotary pump coupled to a 560 L/s turbomolecular pump (TMP) to a base pressure less than 8×10^{-5} Pa. A Pirani gauge, a type of thermal conductivity gauge, was used to monitor the pressure ranging from atmospheric pressure down to 0.4 Pa. For pressures below 1 Pa, down to about 1×10^{-6} Pa, a hot-filament-type ionization gauge was utilized.

A gate valve connecting the vacuum chamber to the inlet of the TMP was half closed to restrict the gas outflow and to keep the pressure in the chamber constant during the experiments.

3.1.2 Power supplies

Continuous microwave power with 2.45 GHz frequency was supplied to the internal antenna by an *Eiko Brain* MR-202 integrated power generator via a coaxial cable. The MW power generator can be operated up to 200 W forward power. A three-stub tuner connected to the antenna end of the line was used for impedance matching between the transmission line and the plasma. The tuner produces a standing wave between itself and the plasma discharge, increasing the coupling to the plasma and reducing the reflected power along the line.[31]

A *Texio* PSF-400H regulated DC power supply, which has maximum output voltage of 800 V, was used to bias the carbon sputtering target negatively with respect to the chamber. On the other hand, a *Kikusui* PAS500-1.2 DC supply, with 500 V maximum output, was used to bias the deposition substrate positively with respect to the chamber.

3.1.3 Magnets

Three types of magnets were used in the experiments: an electromagnet, a permanent magnet and a temporary magnet, as shown in Fig. 3.3.

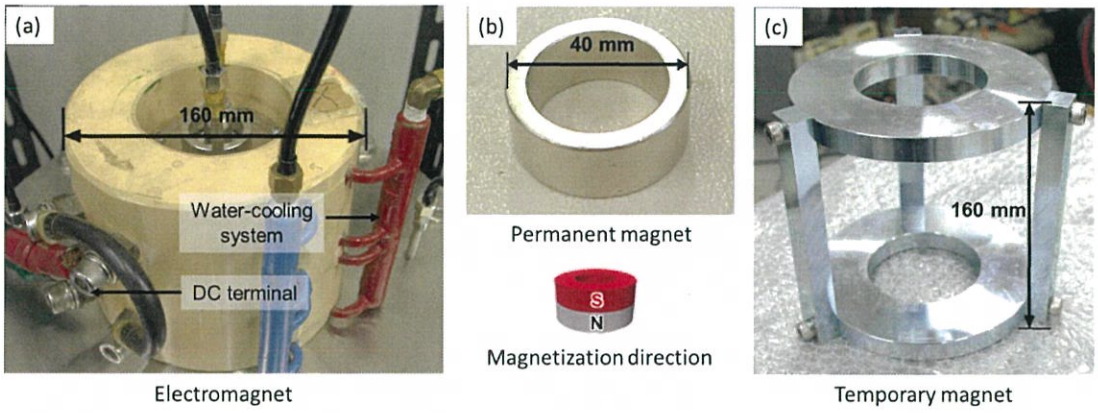

Fig. 3.3 Photo of (a) the electromagnet, (b) the permanent magnet and a diagram of its magnetization direction, and (c) the temporary magnet installed to the ECR plasma system.

The electromagnet, shown Fig. 3.3a, has 125-mm height, 160-mm outer diameter, and 80-mm inner diameter. It consists of two connected toroidal solenoids encased in an insulating covering. It is placed around the source chamber to generate a divergent magnetic field downward. The electromagnet has two terminals connected to a *Kikusui* PVS 12-220 regulated DC power supply, which can be operated up to 12 V. As the current applied to the electromagnet I_B was changed, the steady-state, spatially-varying magnetic field also changed in intensity. A water-cooling system is integrated into the electromagnet to prevent the coils from heating up during the experiments.

Displayed in Fig. 3.3b is a photo of the Neodymium-Iron-Boron (NdFeB) permanent magnet and its magnetization direction, which was placed around the N-type connector shown in Fig. 3.4. The permanent magnet has 16-mm height, 40-mm outer diameter, and 30-mm inner diameter. It was used to reduce diffusive loss of electrons to the flange where the antenna is mounted.

Later in the study (Chapter 5), temporary magnets made of carbon steel, shown in Fig. 3.3c, was attached around the electromagnet to serve as a magnetic flux return. A

temporary magnet acts like a permanent magnet only when they are within a strong magnetic field. It was used to swallow magnetic field away from the substrate region. The flux return consists of five pieces of temporary magnets: two ring-shaped and three rectangular components. The 160-mm-outer-diameter, 80-mm-inner-diameter, and 15-mm-thick ring-shaped magnets are placed on the top and at the bottom of the electromagnet. The 160-mm-high, 20-mm-long, and 15-mm-wide rectangular magnets are attached on the sides of the electromagnet, and are connected to the ring-shaped magnets on both ends with screws.

3.1.4 Source chamber

The cylindrical source chamber, shown in Fig. 3.4, is made of SUS 304 stainless steel with 77-mm inner diameter and 96-mm depth. The microwave antenna was attached to an 80-mm-diameter water-cooled flange, which is installed on top of the source chamber. The antenna was connected to the tuner through a vacuum-tight N-type connector. The structure of the antenna is described in more detail in Chapter 4. The source and process chambers are joined by fixing the 350-mm water-cooled flange on top of the process chamber with Rubber O-ring seal in between.

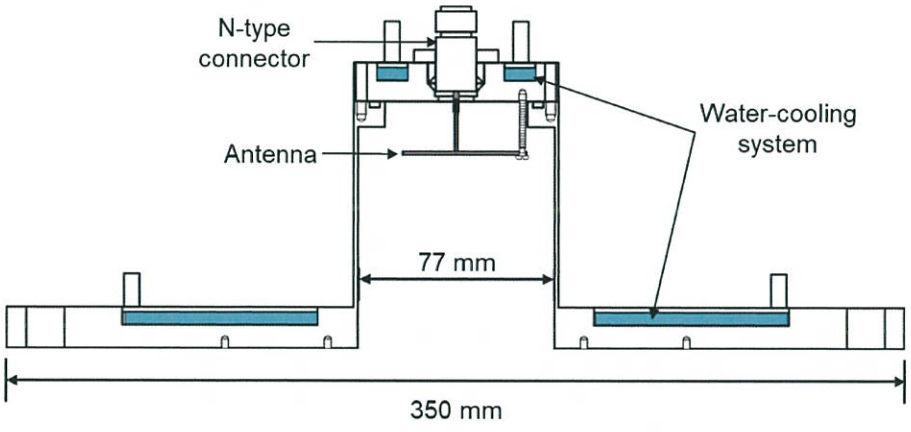

Fig. 3.4 Schematic diagram of the source chamber.

3.1.5 Process chamber

The process chamber is an SUS 304 stainless steel cylinder with 260-mm inner diameter and 230-mm depth, as shown in Fig. 3.5. A 215-mm-long, 65-mm-diameter substrate holder is inserted through the bottom slot of the process chamber. More details on the substrate holder are presented in Chapter 6. About 10 mm above the substrate holder is a gas injection unit, which is described in the following section. Infrared plates are installed around the substrate holder to enhance the increase in substrate temperature by infrared radiation from a tungsten heater.

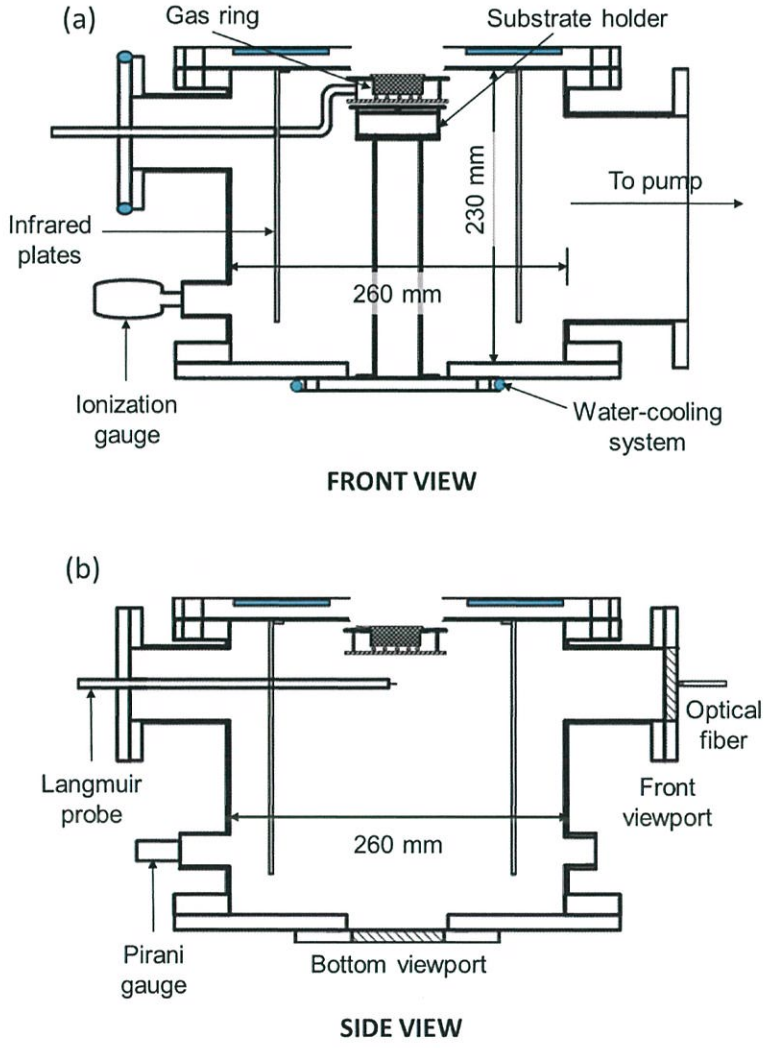

Fig. 3.5 Schematic diagram of the process chamber: (a) front view and (b) side view.

To be able to install the bottom viewport and the Langmuir probe, the substrate holder should be removed, as shown in Fig. 3.5b. The Langmuir probe was inserted radially into the process chamber (perpendicular to the magnetic field) at a distance of 153 mm from the top flange, where the antenna was attached. The front viewport is about 210-mm away from the chamber axis. It is where the fiber sensor head was mounted perpendicularly at the same level as the Langmuir probe.

3.1.6 Gas Injection Unit

Hydrogen gas was introduced into the process chamber using a ring-shaped gas inlet, shown in Fig. 3.6, with 56-mm outer and 38-mm inner diameters. The gas ring was connected to an s-shaped stainless steel tube that leads to a slow leak needle valve located outside the vacuum chamber. A disk-shaped, 80-mm-outer-diameter, 38-mm-inner-diameter, 1-mm-thick carbon sputtering target is placed on the gas ring nozzles, facing the substrate holder. In addition, a 2-mm-thick, 15-mm-high cylindrical carbon target was inserted into the inner diameter on the opposite side of the gas ring, facing the source chamber. Through ECR sputtering process, the unit supplies hydrocarbon molecules homogeneously to the deposition substrate.

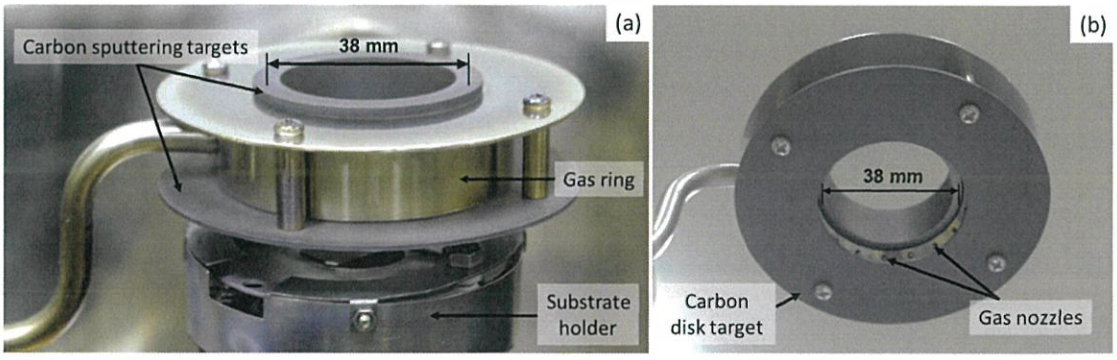

Fig. 3.6 (a) Photo of the gas injection unit with carbon sputtering targets. (b) Bottom view of the gas injection unit.

3.2 Langmuir Probe Measurement

3.2.1 Principle of Langmuir I-V Characteristic

When a biased Langmuir probe is immersed in plasma, the charged particles distribute themselves spatially around the probe, forming a *plasma sheath*, to shield out electric fields applied to them by the probe. Such phenomenon is called *Debye shielding* and it is one of the characteristic and collective behaviors of plasma which keeps the bulk of the plasma quasineutral at a roughly constant potential V_{pl} (plasma potential).[32] Plasma sheaths, which also form near the chamber walls or any surface in contact, are few Debye lengths thick. A *Debye length* is one of the characteristic lengths of plasma which is given by,[17]

$$\lambda_D = \sqrt{\left(\frac{\epsilon_0 T_e}{e n_e}\right)} \tag{3.1}$$

where T_e is the electron temperature in volts (V).

Langmuir probe theory applied in this study relies on the following assumptions on the Debye length of the plasma and other characteristic lengths:[33]

1. $\lambda_D \ll L$ (plasma dimension), so that the plasma is homogeneous, quasineutral and infinite.
2. $\lambda_D \ll r_p$ (probe radius), so that edge effects can be neglected.
3. Mean free path of all particles $\lambda \gg \lambda_D, r_p$, such that no collisions occur in the probe sheath.
4. The probe surface is completely absorbing and non-reactive.

Based on these assumptions, we can now give a qualitative interpretation on the Langmuir current-voltage (I-V) characteristic. An I-V curve can be obtained by sweeping the applied bias voltage on the probe (probe voltage), V_p, from a negative to a positive

potential, and measuring the drained current, called the probe current I_p, for each V_p. A typical I-V curve obtained from Langmuir probe measurement is shown in Fig. 3.7, where a positive I_p represents a net current flow into the plasma (electrons attracted to the probe), and a negative I_p denotes a current flow out of the plasma (ions attracted to the probe). I_p is composed of ion I_i and electron I_e currents:

$$I_p = I_i + I_e \tag{3.2}$$

When V_p is at the plasma potential V_{pl}, there is no plasma sheath, and the surface of the probe collects the ions and electrons that hit it.[34] V_{pl} is generally positive with respect to the chamber, because the electrons tend to escape to the walls faster than the more massive ions, leaving the plasma with an excess of positive space charge.

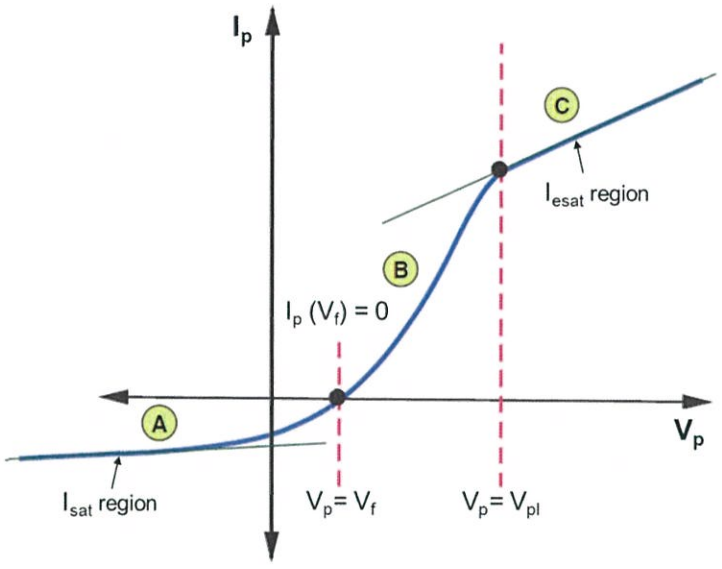

Fig. 3.7 A typical Langmuir probe current-voltage characteristic curve (after. Ref. 35).

When V_p is negative with respect to V_{pl} ($V_p < V_{pl}$), as in region B, the probe begins to repel electrons and attract ions. However, the ion current is still negligible in comparison to the electron current, again because the electrons reach the probe faster than the ions. As soon as V_p reaches the floating potential V_f, the electron current is suppressed enough that it equals the ion current, resulting in a zero net current (I_p = 0). A positive space

charge sheath forms near the probe when the ion density exceeds the electron density at the sheath edge, which occurs if the ions approach the sheath with a speed exceeding the Bohm velocity u_B given by,[36]

$$u_B = \sqrt{\frac{eT_e}{m_i}} \tag{3.3}$$

where m_i is the ion mass.

In region A, when $V_p \ll V_{pl}$, all electrons are repelled and the positive sheath surrounding the probe shields out and limits the collected ion current. As a result, I_p decreases slowly and becomes approximately constant. This I_p value is called the ion saturation current, I_{sat}. When $T_e \gg T_i$ (ion temperature), the ion saturation current is given by the Bohm ion current I_B,

$$I_{sat} = I_B = 0.6eA_p n_i u_B \tag{3.4}$$

where A_p is the probe collecting area.

For a Maxwellian ion distribution at the temperature T_i, the dependence of the ion current I_i on V_p is given by,[37]

$$I_i(V_p) = \begin{cases} I_{isat} exp\left[\frac{e}{k_B T_{iK}}(V_{pl} - V_p)\right] & V_p \geq V_{pl} \\ I_{isat} & V_p < V_{pl} \end{cases} \tag{3.5}$$

where k_B is the Boltzmann constant and T_{iK} is the ion temperature in Kelvin (K).

In region C, where $V_p > V_{pl}$, the ions are repelled and the electrons are attracted to the probe. A negative space charge sheath forms around the probe, effectively expanding the collecting area, thus, slightly increasing I_p.[34] For $V_p \gg V_{pl}$, the current I_p levels off to a value called the electron saturation current I_{es}, which is given by,[36]

$$I_{esat} = \frac{1}{4} eA_p n_e \bar{v} \tag{3.6}$$

where $\bar{v}$ is the electron average speed, given by,

$$\bar{v} = \sqrt{\frac{8eT_e}{\pi m_e}} \tag{3.7}$$

For a Maxwellian electron velocity distribution, the dependence of electron current I_e on V_p is given by,

$$I_e(V_p) = \begin{cases} I_{esat} exp\left[\frac{e}{k_B T_{eK}}(V_p - V_{pl})\right] & V_p \leq V_{pl} \\ I_{esat} & V_p > V_{pl} \end{cases} \tag{3.8}$$

where T_{eK} is the electron temperature in K.

The floating potential V_f can be derived from Eqs. (3.5) and (3.8), by setting it as the voltage V_p at which $I_i(V_f) + I_e(V_f) = 0$. Hence,

$$V_f = V_{pl} + \frac{k_B T_{eK}}{e} ln\left(0.6\sqrt{\frac{2\pi m_e}{m_i}}\right) \tag{3.9}$$

3.2.2 Langmuir Probe Setup

The cylindrical Langmuir probe used in this study to measure the local plasma parameters is shown in Fig. 3.8. It has an inner 0.5-mm-diameter tungsten wire, surrounded by a ceramic tube, surrounded by a Cu tube, and then covered by a 5-mm-outer-diameter tubular ceramic. 5-mm length of the tungsten wire tip was exposed to the plasma, while the rest of the probe components are covered by the outer ceramic.

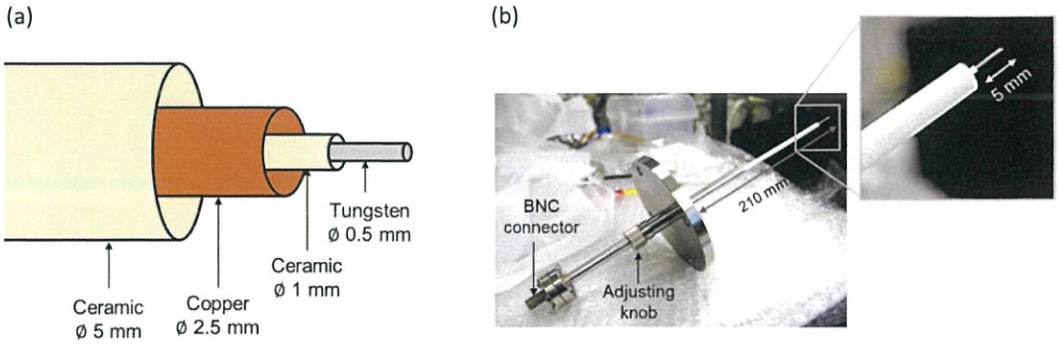

Fig. 3.8 (a) Schematic diagram, and (b) photo of the Langmuir probe used in the experiments.

The probe tip is positioned at the chamber axis. The radial position of the probe tip was varied by slightly loosening the adjusting knob, then pulling the probe back or pushing it forward. The Cu tube is kept in ground potential to serve as a shield that restricts outside electromagnetic fields to leak inside the shield, and vice versa. A signal carrying voltage was applied to the tungsten wire through a BNC connector attached to the other end of the probe. The circuit diagram of the Langmuir probe setup is shown in Fig. 3.9. The applied voltage to the probe was oscillating at a rate of 10 Hz. As the source voltage V_s was swept from -35 V to +35 V with respect to the chamber, I_p was measured through the voltage drop it creates across the shunt resistor. The voltage drop is taken as the difference between V_s and V_p, which are measured using a 2-Ch *Picoscope* 4224 USB scope with 12-bit resolution. The probe current is then given by,

$$I_p = \frac{V_s - V_p}{R} = \frac{V_{CH1} - V_{CH2}}{R} \tag{3.10}$$

where R is the electrical resistance of the shunt resistor, which in our case is 3200 Ω. The current I_p was plotted as a function of the voltage V_p and the plasma parameters were calculated from this I-V characteristic curve.

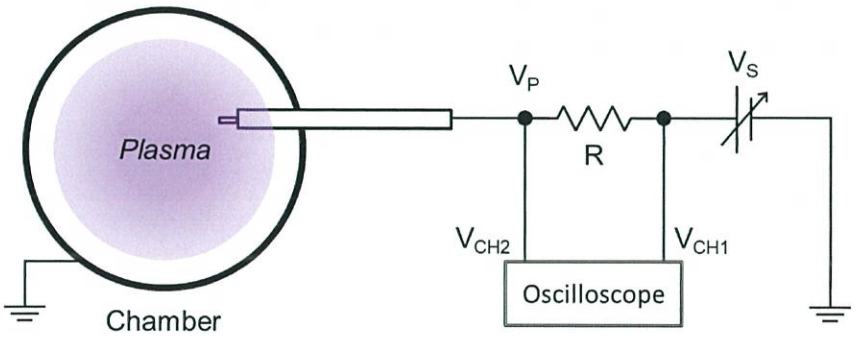

Fig. 3.9 Circuit diagram of the Langmuir probe setup

3.2.3 Determination of the Plasma Parameters

Shown in Fig. 3.10 is an example of an I-V curve obtained from a raw data, where the floating potential V_f and ion saturation current I_{sat} can be determined directly, since the Langmuir probe used in the ECR source is not subject to signal pickup which can greatly distort the I-V characteristic. The ECR source operate in microwave frequency which is so high that the signal is completely decoupled from the circuitry, and the measured currents are the same as in a DC discharge.[38]

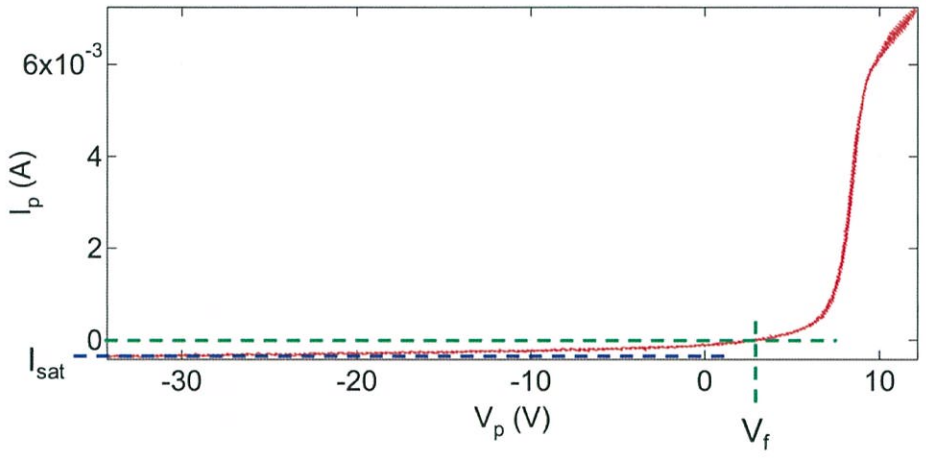

Fig. 3.10 Probe current plotted as a function probe voltage from raw data.

The electron temperature T_e can be determined from the transition region of the I-V characteristic (region B in Fig. 3.7), where $V_p < V_{pl}$.[36] By substituting V_{pl} from Eq. (3.9) into (3.8) for $V_p \leq V_{pl}$, and taking the natural logarithm of both sides of the equation, we get

$$ln|I_e| = \frac{e}{k_B T_{eK}}(V_p - V_f) + \mathrm{C} \tag{3.11}$$

where C is a constant. Notice that Eq. (3.11) is in the form of a line function $y = mx + b$, where m and b are the slope and y-intercept, respectively. In the case of Eq. (3.11), the slope is given by,

$$m = \frac{e}{k_B T_{eK}} \equiv \frac{1}{T_e} \tag{3.12}$$

where $k_B T_{eK}$ is expressed as eT_e. Then, substituting I_e from Eq. (3.2) into (3.11), and taking the current I_i for $V_p < V_{pl}$ in Eq. (3.5), we have,

$$\ln|I_p - I_{isat}| = \frac{1}{T_e}(V_p - V_f) + C \tag{3.13}$$

The I_{sat} value determined in Fig. 3.10 is subtracted from the current I_p, and the natural logarithm of the difference is plotted as a function of V_p, as shown in Fig. 3.11. Straight lines are fitted along the transition region and the section where $V_p > V_{pl}$. The voltage V_p across the intersection of these two fitted lines is the plasma potential V_{pl}, and the inverse of the slope of the line in the transition region is the electron temperature T_e.

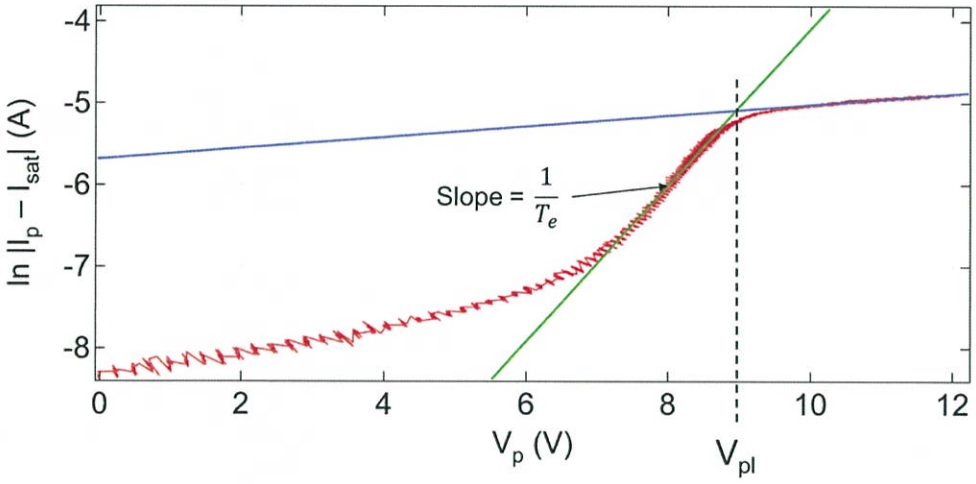

Fig. 3.11 Zoomed semi-logarithmic plot of electron current as a function of probe voltage, with lines fitted along the transition and positive-V_p regions.

As observed in Fig. 3.10, the positive V_p is not high enough to reach the electron saturation current I_{esat}. Since it is difficult to determine I_{esat} in the I-V curve, Eq. (3.6) cannot be used to solve for the electron density n_e. We know, however, that the bulk of the plasma is quasineutral, such that $n_e \simeq n_i$, hence, we can use Eq. (3.4) to obtain the ion

density n_i, then setting it equal to n_e. By substituting the Bohm velocity u_B from Eq. (3.3) into (3.4), and then solving for n_i, now equal to n_e, we get,

$$n_e = \frac{I_{sat}}{0.6e^{\frac{3}{2}}A_p}\sqrt{\frac{m_i}{T_e}} \tag{3.14}$$

The ion mass m_i, is given by,

$$m_i = (\text{atomic weight}) \times (u) \tag{3.15}$$

where u is the atomic mass unit. For hydrogen ion, we have, $m_i = 1.67 \times 10^{-27}$ kg. The cylindrical probe used in this study has a collecting area $A_p = 8.05 \times 10^{-6}\,\text{m}^2$, which was calculated using the following surface area formula,

$$A_p = \pi r_p^2 + 2\pi r_p l_p \tag{3.16}$$

where the probe radius $r_p = 5 \times 10^{-4}$ m and the exposed probe length $l_p = 5 \times 10^{-3}$ m.

3.3 Image Luminosity Capture

Excited hydrogen atoms typically emit light with frequencies that are in the visible spectrum (656, 486, and 434 nm). For this reason the image luminosity of plasmas was used to roughly estimate the plasma density or the density of the excited species present in the plasma discharge. Photographs of plasmas were taken with a *Pentax* K-7 14.6 megapixel digital single-lens reflex (DSLR) camera equipped with an 18–55 mm f/3.5–5.6 zoom lens. The camera was attached to a tripod mount positioned at a fixed distance from the viewport. The camera settings used in taking plasma photos through the front and bottom viewports are listed in Table 3.1.

The photos were converted from Pentax raw image files (PEF) to 24-bit color image files (PPM) using a DCRAW computer program, based on the white balance setting of the camera at the moment of shot (see Appendix). The colored PPM images were then converted to grayscale, based on the gray values calculated from the weighted average of

Table 3.1 Camera settings used in taking photos through the viewports for luminosity calculation

Setting	Front viewport	Bottom viewport
Aperture size	f/32	f/40
Shutter speed	0.6 seconds	1/8 seconds
ISO sensitivity	800	200
Focal length	45 mm	55 mm
Exposure bias	0	0

RGB levels at each pixel. This weighting assumes that red represents 30% of the perceived luminosity, while the green and blue channels account for 59 and 11%, respectively. Plasma density and uniformity were estimated using the luminosity of plasma photos taken through the front viewport. Plasma density was based on the mean luminosity of the photo taken over the sampling area about 25 mm below the source chamber, as shown in Fig. 3.12a. An example of a luminosity histogram obtained from a photo is shown in Fig. 3.12c. The grayscale conversion and mean luminosity calculation of the plasma photos were done using a batch code (refer to Appendix) executed in GNU *Octave* software, which provides a numerical computing environment. On the other hand,

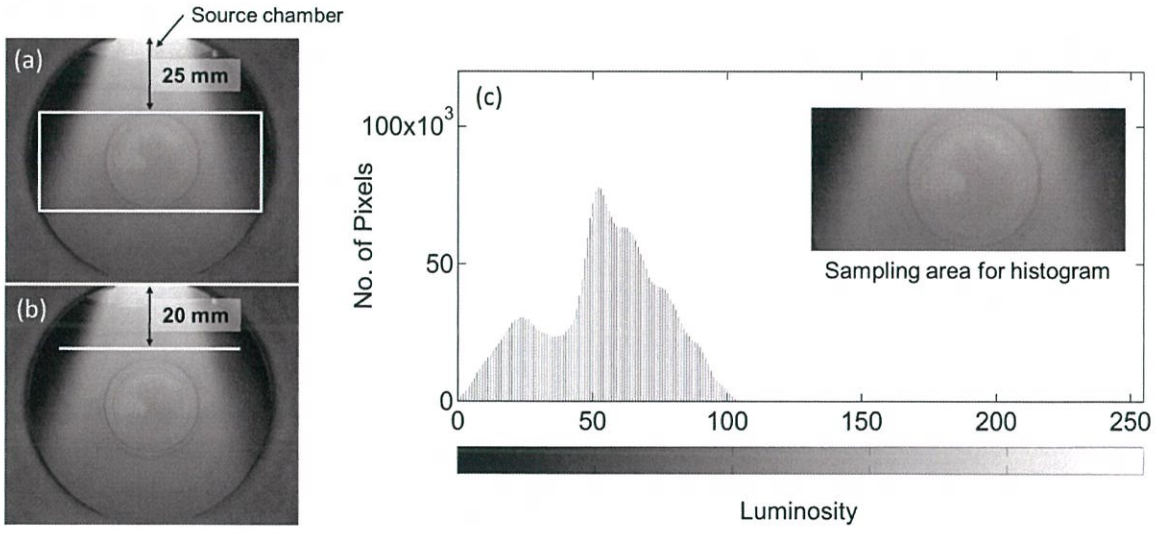

Fig. 3.12 (a) Sampling area for mean luminosity calculation, (b) sampling line for the acquisition of luminosity spatial distribution, and (c) luminosity histogram of a photo.

plasma uniformity was based on the spatial distribution of the luminosity taken along the sampling line about 20 mm below the source chamber, as shown in Fig. 3.12b. The luminosity distribution was obtained using an image processing program called *ImageJ*.

3.4 Frequency Spectrum Analysis

The microwave power absorption of the plasma was assessed through frequency spectrum analysis. Incident microwave radiated by the transmitting antenna that is poorly absorbed by the plasma propagates into the process chamber. Thus, a 60 × 8 mm^2 folded dipole receiving antenna inserted into the process chamber 153 mm below the antenna flange, as shown in Fig. 3.13, was used to detect the local intensity of transmitted microwave power. When transmitted microwave falls on the receiver, the interaction between the antenna and the microwave gives rise to a wave in the receiver line connected to an Anritsu MS2724B spectrum analyzer. The Langmuir probe was taken out of the chamber during microwave signal detection to eliminate any electromagnetic interference caused by the probe.

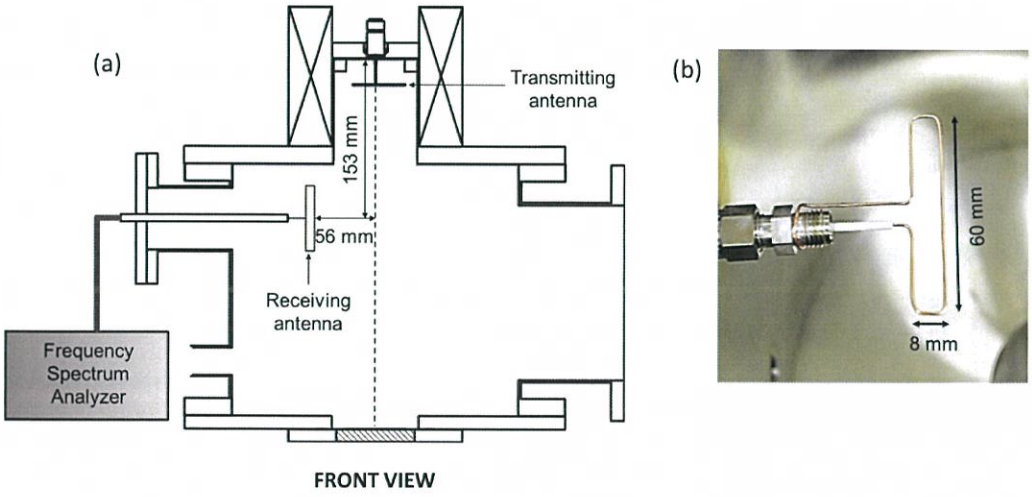

Fig. 3.13 (a) Schematic diagram of the frequency spectrum analysis setup and (b) actual image of the receiving antenna used to detect microwaves transmitted to the chamber.

Chapter 4

Microwave Coupling using Internal Antenna

4.1 Introduction

The method of microwave power coupling to the resonance zone, as illustrated in Fig. 2.3, greatly affects the ion energy, uniformity, and density of the plasma.[17] Properties of ECR plasma depend not only on the coupling method but also on the structure of the microwave coupler.[25] Microwave couplers or applicators are utilized for several functions in plasma processing applications, such as:

1. Impedance matching and optimization of microwave power transfer to the plasma
2. Improvement of plasma particle production efficiency
3. Enhancement of plasma density uniformity and controllability

Microwave applicators that are typically used in ECR reactors include antennas, waveguides, surfatrons and resonant cavities.[31] The common feature of these applicators is that microwave power is coupled to the plasma across a dielectric window or wall, to reduce the voltage across plasma sheaths at wall surfaces.[17] However, contamination from sputtered dielectric material and accumulation of ejected particles on the window requires frequent cleaning and maintenance cycles for the plasma source. Moreover, although strong electrostatic coupling occurs between the antenna and the plasma in the absence of a dielectric barrier, the ECR source operates in microwave regime, in which

the signal frequency of the antenna is comparable to the electron plasma frequency. The antenna never maintains its polarity long enough to sweep much of the electrons. It results in reduced electron loss and plasma potential in ECR plasmas compared in RF discharges.[39] Therefore, this chapter investigates and evaluates a "windowless" method of microwave coupling to ECR plasma using an internal antenna.

4.2 Theoretical Background

4.2.1 Propagation of Electromagnetic field by an Antenna

Microwave antennas are radiation applicators in which microwave energy propagates freely in the load like free space wave, without being significantly bounded to certain geometry.[40] To give a basic principle of electromagnetic field radiation by an antenna, let us consider a simple dipole antenna of which length is half of the wavelength, $\lambda/2$, of the input signal, as shown in Fig. 4.1a. When the signal is fed on the antenna, an electron flow sets up within in it. The electrons flow towards the positive potential and form a

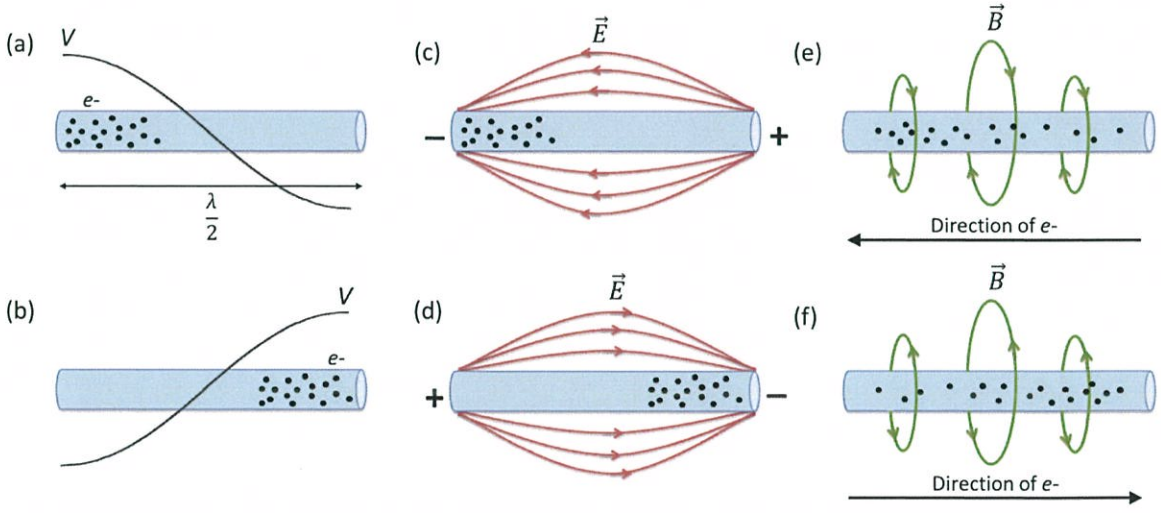

Fig. 4.1 Diagram of EM Field excitation by a dipole antenna. (a) The electrons flow towards the positive potential and (b) moves in the opposite direction as it reverses. (c) Electric fields are produced between the opposite polarities, and (d) reverses in direction with the polarity. (e) Magnetic fields are produced from the electron flow, (f) of which direction also reverses.

maximum concentration on one side (Fig. 4.1a). As the polarity of the potential reverses, the electrons move towards the opposite direction and form a maximum on the other side (Fig. 4.1b). A cycle of this process occurs and repeats itself at the signal frequency. Due to the electron concentration on one side, a negative potential builds up on that side and a positive potential on the other. The opposite polarities produce electric field between them which reverses in direction at each half cycle of the signal frequency, as shown in Fig. 4.1c and d. In addition, the electron flow in the antenna creates magnetic field which changes in direction relative to the direction of current, as illustrated in Fig. 4.1e and f. These electric and magnetic fields constitute the antenna's immediate field, which produces a radiating wave pattern that propagates away from the antenna, as illustrated in Fig. 4.2.[41]

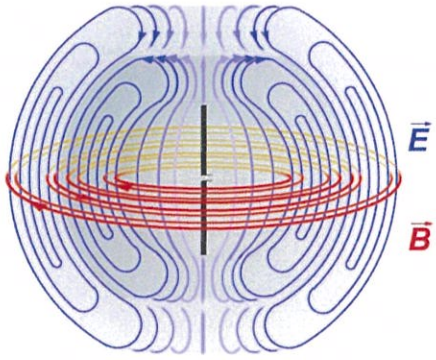

Fig. 4.2 Diagram of electromagnetic field radiation by a dipole antenna (after Ref. 42).

4.2.2 The Antenna as a Terminating Impedance

Let us consider an isolated antenna where all other antennas are removed from the system such that its interactions with them need not to be considered. The antenna functions like a dissipative load on the transmission line where it extracts power. Part of this absorbed power is radiated into space, and part is dissipated into heat in the antenna structure.[43] If the antenna impedance or if the tuner is adjusted to transform the antenna impedance equal to the line impedance, the incident forward power is the power

absorbed by the antenna. Because the line is terminated in its characteristic impedance, there is no reflected wave and no standing wave in the line.[44] On the other hand, if the impedance of the antenna and the line are mismatched, the antenna does not absorb the entire power incident on it but gives rise to a reflected wave in the line.

4.2.3 Antenna and Plasma Coupling

In the previous section, the transmitting antenna is treated as an isolated system and the significant feature of the interaction between the antenna and the plasma is neglected. Now, consider a transmitting antenna that when completely isolated is matched to its line. When a conducting medium, such as plasma, is introduced into the field of this transmitting antenna, it gives rise to a scattered wave. This, when detected by the transmitting antenna, in turn gives rise to a wave transmitted down the feed line of that antenna. The net effect is that the transmitting antenna no longer gives a matched impedance to its line.[43] For this reason, the reflected power fluctuates whenever the plasma condition changes.

4.2.4 Antenna Resistance

The total power dissipated by the antenna is the sum of the radiated power and the power dissipated in ohmic losses in the antenna structure. Correspondingly, the electrical resistance of the antenna can be taken as a sum of two elements: a radiation resistance and an ohmic resistance.[43] The power dissipated in the radiation resistance is converted into electromagnetic radiation, while that of in the ohmic resistance is converted into heat.

When an AC signal is fed to the antenna, the electrons radiate electromagnetic waves, as described in section 4.2.1. These waves carry energy absorbed from the electrons. And, the loss of energy appears as an effective resistance to the electron flow. This is

comparable to the ohmic resistance resulted from the scattering of electrons in the crystal lattice of the material, hence, hindering the electron current. Radiation resistance depends on the geometry of the antenna, while the ohmic resistance is mainly determined by its material.[45]

In addition to the intrinsic resistance of the antenna described above, a contact resistance due to weakly contacting interfaces may occur. Surfaces of metallic contacts may have an oxide layer and adsorbed water molecules which reduces charge transport efficiency between the interfaces.

4.3. Materials and Methods

4.3.1 Antenna Flange Configuration

Since the microwave antenna excites plasma locally, the distance between the antenna and the graphite sputtering target is an important parameter that decides the system's overall performance. Therefore, the device has been operated with three antenna configurations to change the distance between the graphite target and the antenna. Fig. 4.3 shows the source chamber of the ECR plasma system in three types of configurations: *far, mid*

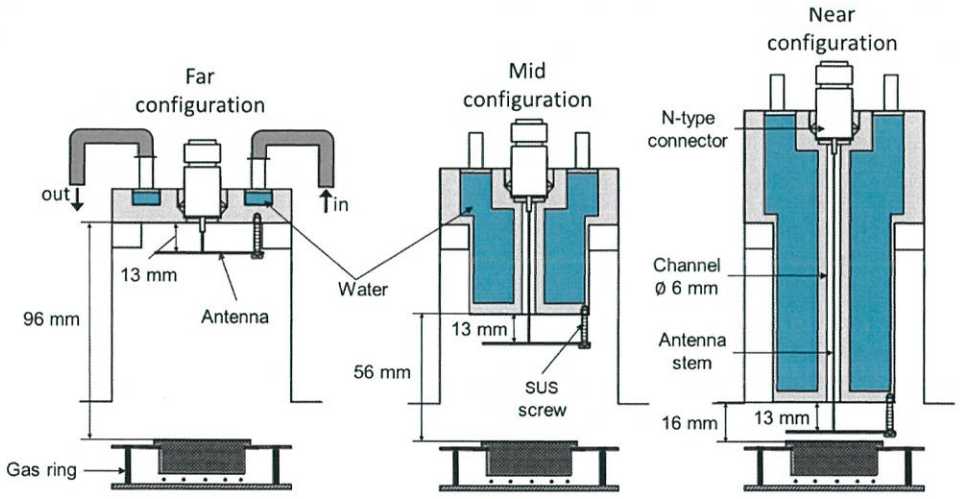

Fig. 4.3 Geometry and position of the antenna flange relative to the gas ring in each configuration.

and *near*, in which the antenna flange is 96, 56 and 16 mm away from the gas ring, respectively. In all the configurations, the distance between the antenna and the bottom of the flange is 13 mm. In mid and near configurations, the stem of the antenna is inserted into a 6-mm-diameter channel along the vertical axis and attached to the N-type connector at the end. The SUS 304 antenna flanges have built-in cavities for the circulating water of the cooling system.

4.3.2 Antenna Structure

The microwave was launched into the chamber through an antenna which was modified in terms of its structure and material. Nickel wires were formed to configure four types of antenna structure: *spiral*, *helical*, *circular* and *linear* as illustrated in Fig. 4.4. The spiral and helical antennas are each composed of n = 6 turns. The 1.5-mm-diameter wire was wound in a counter-clockwise direction when viewed from the vacuum side. The other end of the antenna was connected to a grounded stainless steel screw, as shown in Fig. 4.3.

There are two types of far-configuration flange used in mounting the antennas based on the orientation of the N-type connector. As shown in Fig. 4.5, the spiral and helical antennas are attached to the flange with a centered connector, while the loop and linear antennas are connected to the one with an off-centered connector.

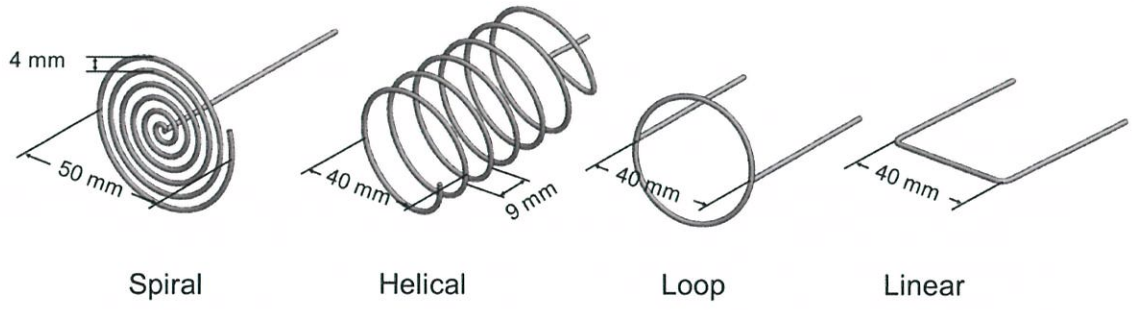

Fig. 4.4 Nickel antenna structures with their corresponding parameters.

4.3.3 Antenna Position

The position of the spiral antenna, *D*, is based on the distance of the spiral plane from the antenna flange, as indicated in Fig. 4.5. For comparison, the position of the spiral antenna was initially set to *D* = 80 mm and was then varied by changing the length of the antenna stem and the grounded screw.

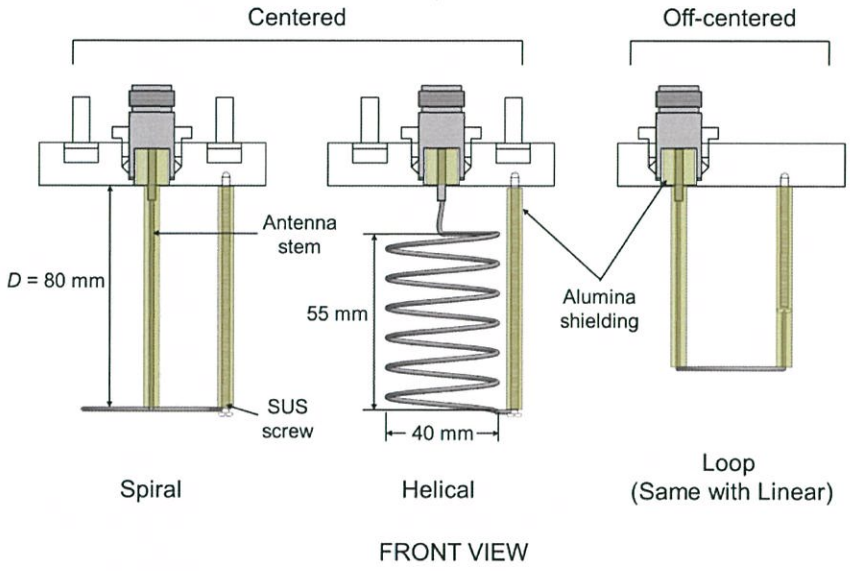

Fig. 4.5 Nickel antennas mounted to two types of far-configuration flange.

4.3.4 Magnetic Field Configuration

As illustrated in Fig. 4.6, the electromagnet (described in section 3.1.3) is installed

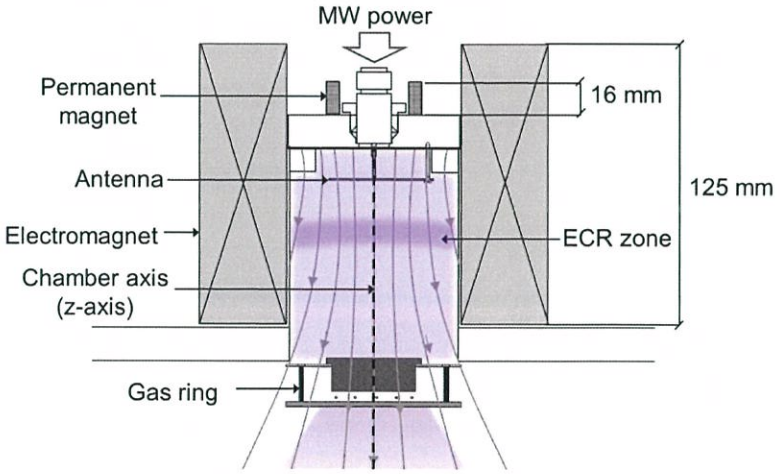

Fig. 4.6 Source chamber with electro- and permanent magnets.

around the source chamber to generate a divergent magnetic field and rely on the magnetic beach absorption of the microwave power. In addition, the permanent magnet is placed above the antenna flange to deflect charged particles away from the flange surface and reduce metal contamination.

The magnetic field intensity along the chamber axis varied with the current applied to the electromagnet I_B, as seen in Fig. 4.7a and b, in the cases without and with permanent magnet, respectively. To examine the dependence of plasma properties on I_B, the current was set from the highest down to the lowest value at each experimental set to avoid any hysteresis effect. Without the permanent magnet, the ECR condition for 2.45 GHz frequency was satisfied when the magnetic field intensity is 87.5 mT at $I_B \geq 80$ A. With the permanent magnet, the ECR condition was attained at $I_B \geq 55$ A.

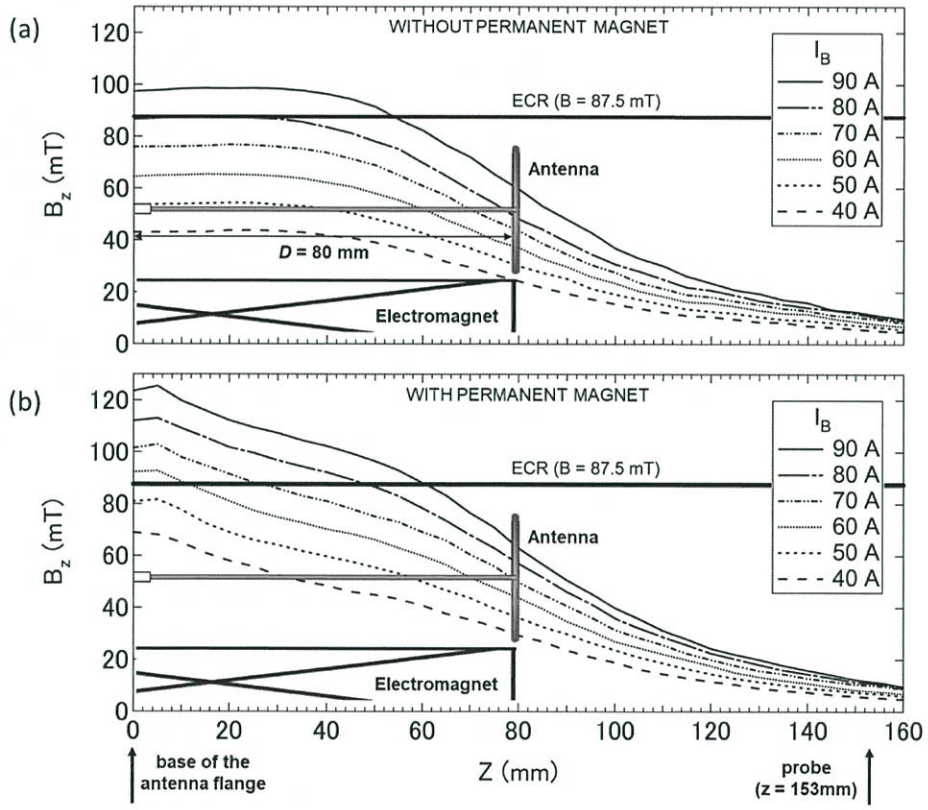

Fig. 4.7 Magnetic field intensity profile along the chamber axis at different magnet current I_B (a) without and (b) with the permanent magnet.

4.4 Results

4.4.1 Effects of the Antenna Flange Configuration

In this section, bare spiral antennas with n = 4 number of turns were utilized. Each antenna has a stem of different length according to the flange configuration described in Fig. 4.3. At this point, the permanent magnet was not yet present. The forward power and hydrogen pressure were fixed at 100 W and 1 Pa, respectively. Photos of plasmas produced in far, mid and near configurations at various magnet current I_B are displayed in Fig. 4.8. Photos were taken through the front viewport facing the region below the gas ring, and through the bottom viewport along the axial axis of the vacuum chamber. It can be observed in the images taken through the front viewport (Fig. 4.8a) that plasmas produced in far configuration are more diffuse than those of in mid and near configurations. Plasma discharges in the latter configurations tended to concentrate at

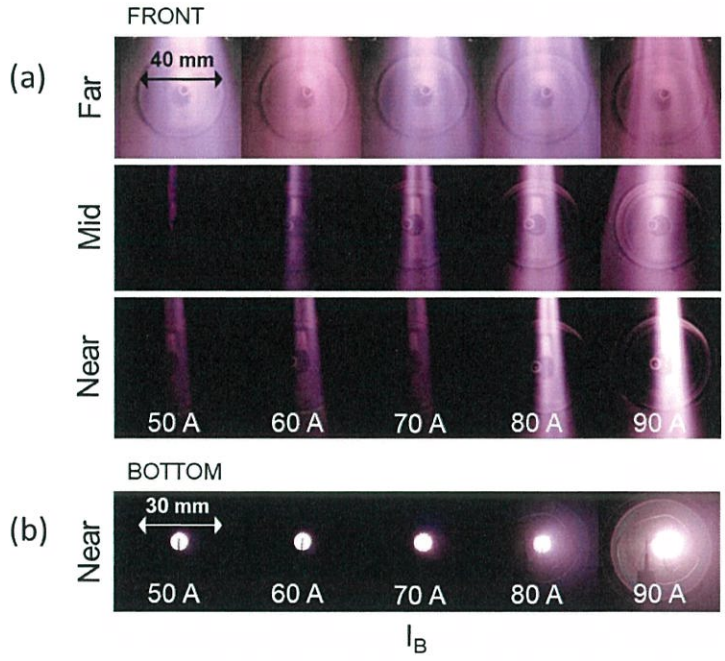

Fig. 4.8 Plasma photos taken (a) through the front viewport at various I_B in each flange configuration, and (b) through the bottom viewport in near configuration.

the central region of the antenna. When observed from the bottom viewport (Fig. 4.8b), plasmas are streaming out from the flange channel in near configuration. It indicates strong capacitive coupling between the plasma and the antenna, which may have been caused by the short distance between the antenna stem and the channel walls. Consequently, plasmas in mid and near configurations were extinguished at relatively higher I_B, since the confining effect of the magnetic field was not enough to sustain the capacitive discharge.

The plasma parameters were obtained based on the measurements done using the Langmuir probe inserted radially into the process chamber, below the gas ring (see Fig. 3.5b). The dependence of electron density n_e on current I_B for different flange configurations is displayed in Fig. 4.9. When I_B was decreased to 70 A, the plasma density in mid and near configurations suddenly decreased. This event can be due to ECR to sub-ECR mode transition,[46] since 80 A was the minimum I_B required to satisfy the ECR condition within the source chamber. Such transition, however, is not observed in far configuration. This behavior is further investigated in section 4.4.6. The obtained average of electron temperature T_e for the three configurations is about 1.4 V.

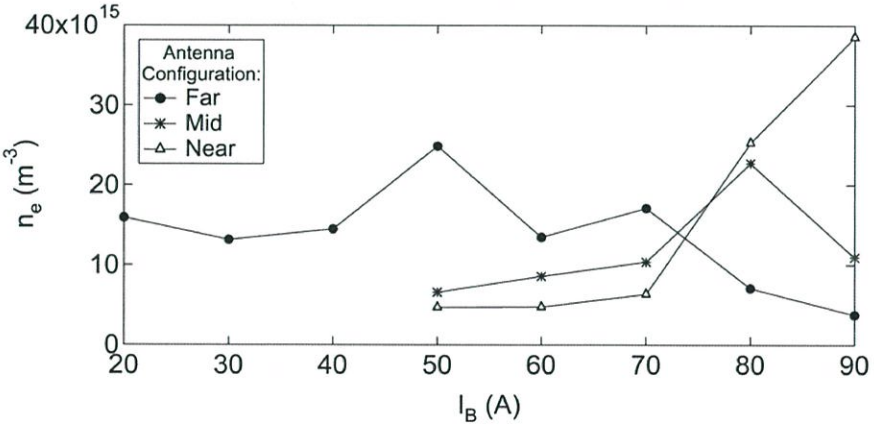

Fig. 4.9 Electron density n_e plotted as a function of I_B for different flange configurations.

Shown in Fig. 4.10 is the dependence of plasma potential V_{pl} on current I_B. In far configuration, the average V_{pl} is about 12 V which is much higher than in other configurations. Since far configuration produced more diffuse plasma, its high plasma potential can be due to the increased diffusion of the electrons to the walls, which left the plasma with more positive charge.

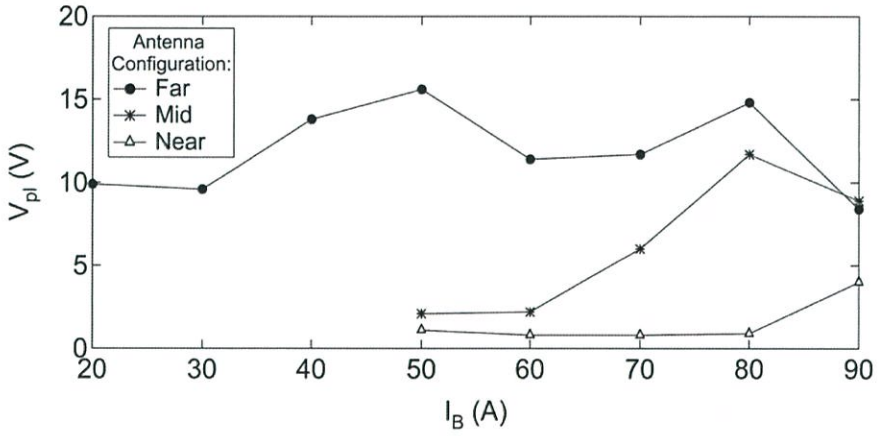

Fig. 4.10 Plasma potential V_{pl} plotted as functions of I_B for different flange configurations.

Reflected power P_r measured from the microwave generator was recorded simultaneously with probe measurements at various magnet current I_B. In Fig. 4.11, it is evident that at $I_B \geq 80$ A, P_r values are very low, which is attributed to the high absorption of microwave power in the resonance zone.

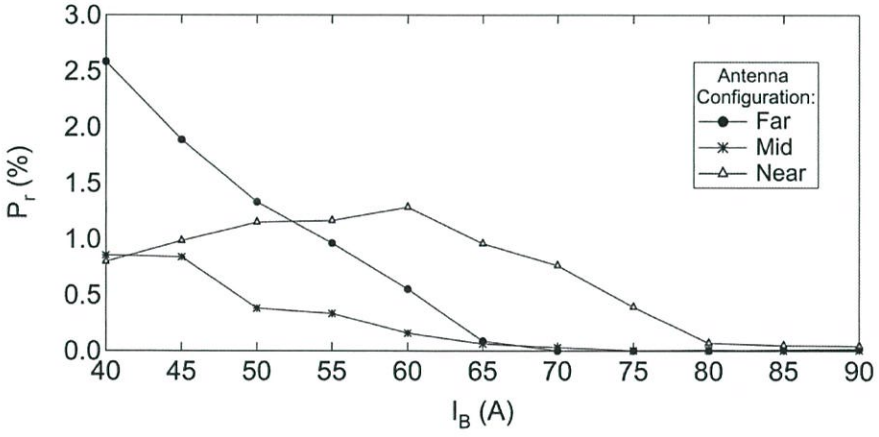

Fig. 4.11 Reflected power P_r plotted as a function of I_B for different flange configurations.

4.4.2 Effects of Antenna Insulation

In far-antenna flange configuration, plasmas can be sustained even at low magnet current I_B, hence, such configuration is used in the following sections. The plasma potential, however, tended to be high in far configuration due to the diffusive loss of electrons to the chamber walls. In addition, when a bare metal antenna, supplied with high-frequency power and grounded on the other end, is immersed in plasma, electrons from the plasma flow through the antenna to the ground.[14] This event further increases the plasma potential, hence, the impact energy of the ions to the substrate. To prevent substrate damage, it is then necessary to reduce the electrostatic coupling between the antenna and the plasma. In this section, the antenna stem and the inner wall of the N-type connector are shielded from the plasma discharge using alumina insulators, as shown in Fig. 4.12. The following results were obtained using bare and insulated spiral antennas, with n = 2 turn and D = 85 mm position relative to the antenna flange.

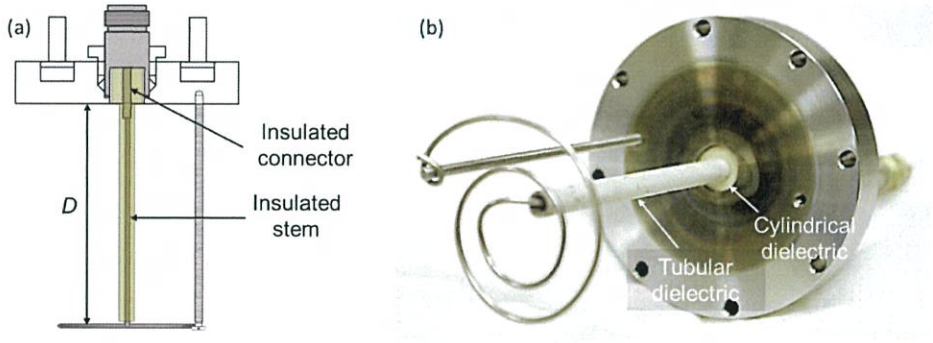

Fig. 4.12 (a) Spiral antenna with insulated connector and stem. (b) Image showing the insulators.

The effect of insulation on plasma potential V_{pl} and electron temperature T_e (deduced from Langmuir probe I-V characteristics) is shown in Fig. 4.13. The average T_e for bare- and insulated-antenna cases was about 1 V. It can be observed that V_{pl} was decreased by half when the antenna was insulated. This indicates that the antenna shielding had effectively reduced the electrostatic coupling between the antenna and the plasma. Such

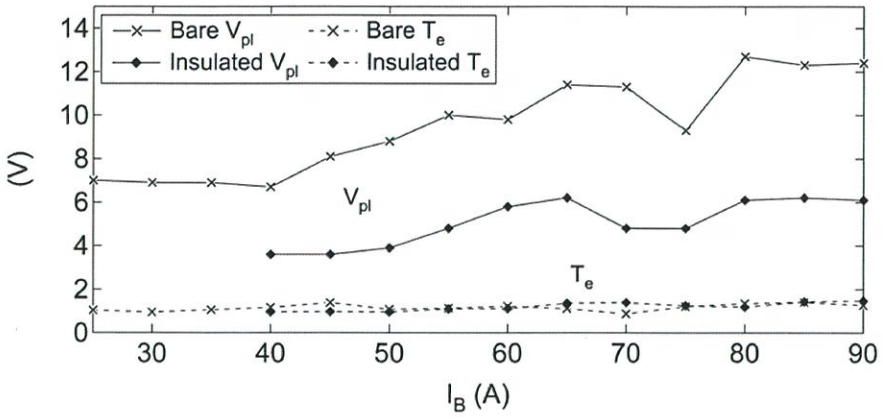

Fig. 4.13 Plasma potential V_{pl} and electron temperature T_e plotted as functions of I_B for bare and insulated spiral antennas.

effect is also evident in the reduced formation of plasma discharges near the antenna, as seen in Fig. 4.14. With the bare antenna, the plasma discharge was concentrated near the antenna stem and the connector, as observed in the bottom-view images. In contrast, plasmas produced by the insulated antenna tend to form in the front region of the spiral structure at currents above 70 A.

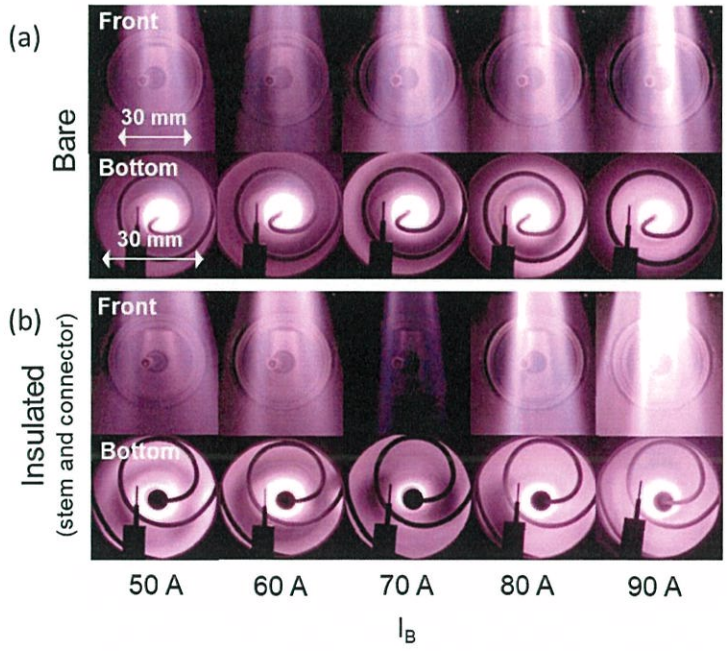

Fig. 4.14 Photos of plasmas produced using (a) bare and (b) insulated spiral antennas, taken through the front and bottom viewports at various I_B.

As discussed in section 3.3, the plasma density is roughly estimated using the image luminosity of the plasma discharge. And, to assess the radial uniformity of the plasma density, the luminosity spatial distribution of plasma photos taken through the front viewport was obtained. The luminosity distribution was evaluated along a sampling line about 20 mm below the source chamber. Fig. 4.15 shows that plasmas produced using the insulated antenna were broader and more homogeneous. This is attributed to the reduced capacitive discharges near the antenna stem and connector, and to the increased plasma discharges generated from the spiral structure of the antenna. With the insulated antenna, setting the current at or above 85 A, gave rise to a much broader luminosity distribution, which might be due to a change in size of the resonant zone.[17]

Based on the images in Fig. 4.14, another noticeable property of plasmas produced using the insulated antenna is the presence of a low-density mode at around 70 A. To

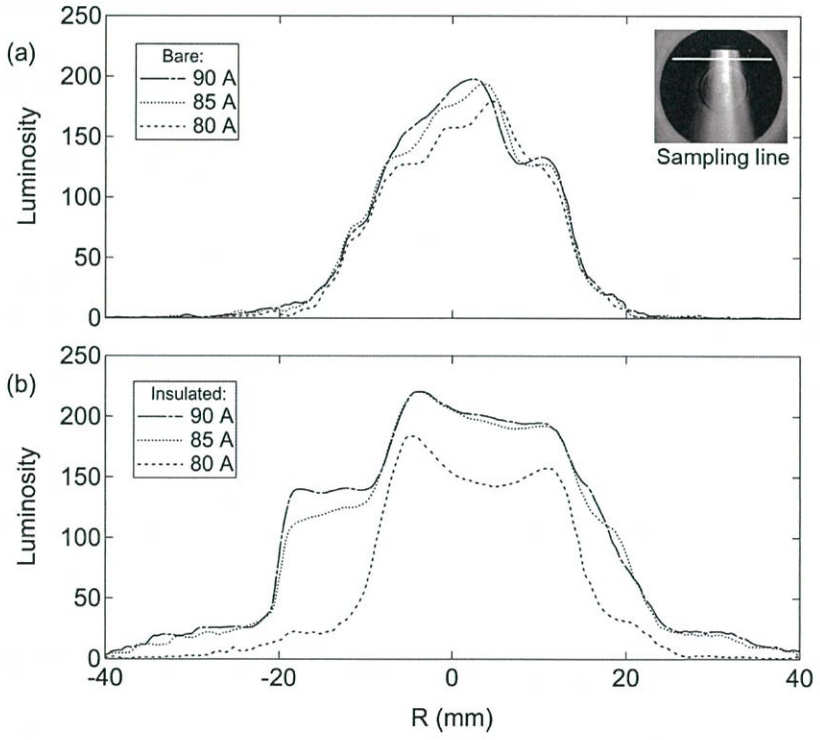

Fig. 4.15 Luminosity spatial distribution of plasmas produced using (a) bare and (b) insulated spiral antennas at various I_B.

examine this behavior, let us isolate the case when only the antenna stem is insulated, from the case when only the connector is shielded. This time, a spiral antenna with n = 2 and D = 50 mm was utilized. As seen in Fig. 4.16, though the image luminosity of the plasmas intensified after insulating the antenna stem, it is when the connector was shielded that the low-density mode began to manifest. This behavior is attributed to the assembly of the connector and the dielectric around it, which resembled a dielectric resonator antenna.[47] As microwave power was introduced through the connector, microwaves can bounce back and forth between the dielectric walls, forming standing waves. Microwaves could have been radiated into the source chamber in an altered radiation pattern, producing the low-density mode. Such mechanism and other factors affecting this low-density mode are further discussed in the following sections.

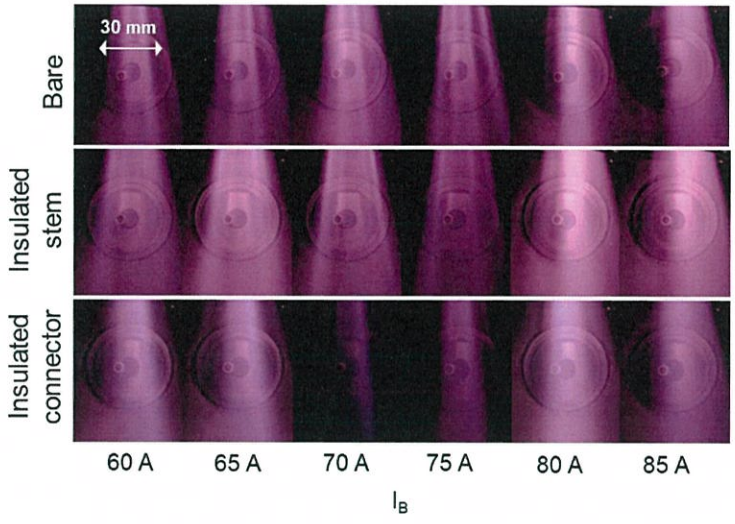

Fig. 4.16 Photos of plasmas produced using bare, stem- and connector-insulated spiral antennas, taken through the front viewport at various I_B.

4.4.3 Effects of Permanent Magnet

The cases with and without the permanent magnet above the antenna flange, as illustrated in Fig. 4.6, are investigated in this section. Stem-and-connector-insulated spiral antenna with n = 2 and D = 95 mm was utilized. Since ion saturation current I_{sat} is

approximately proportional to electron density n_e, based on Eq. (3.14), I_{sat} is then plotted as a function of current I_B. As seen in Fig. 4.17, the I_B value at which the transition to the low-density mode begins shifted from 80 to 75 A when the permanent magnet was present. Note that in the presence of the permanent magnet, 55 A is enough to satisfy the ECR condition, as shown in Fig. 4.7b. Thus, transitions at 75 and 80 A from high-density to low-density mode do not actually represent an ECR to sub-ECR transition. Instead, they could be transitions from inductive to capacitive coupling of the microwave power to the plasma, which was previously observed with external antennas, but not with internal antennas, in inductive RF discharges.[14,48] Such transition is explained in section 4.5.

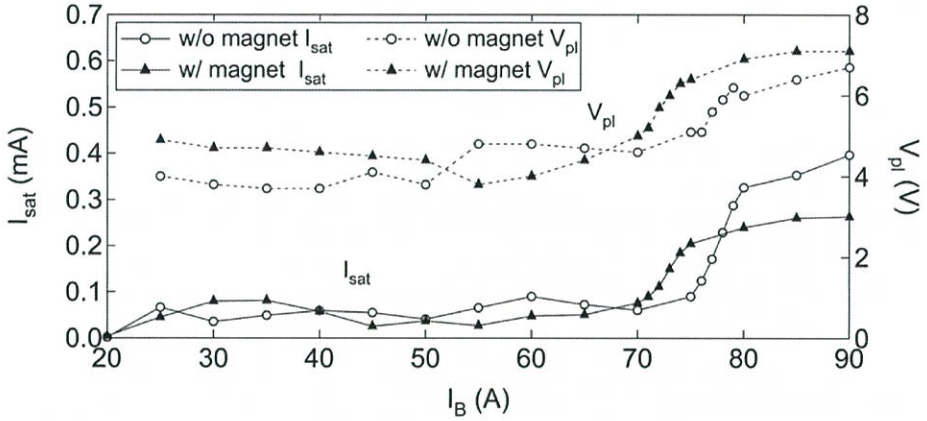

Fig. 4.17 Ion saturation current I_{sat} and plasma potential V_{pl} plotted as functions of I_B in the cases with and without permanent magnet.

As for the plasma potential V_{pl}, measured values in the cases with and without magnetic field are comparable. However, about 25% increase in the potential was observed at some I_B currents when the permanent magnet was present. This may be due to the enhanced diffusion of electrons to the side walls of the source chamber.

4.4.4 Effects of Antenna Structure

Insulated n = 6, D = 80 mm spiral and helical antennas, described in Fig. 4.5, are compared in this section. Photos of plasmas produced at various I_B were taken through

the front and bottom viewports, as shown in Fig. 4.18. To be able to get a full shot of the antenna through the bottom viewport, the gas ring was removed. The permanent magnet was installed in the following series of experiments.

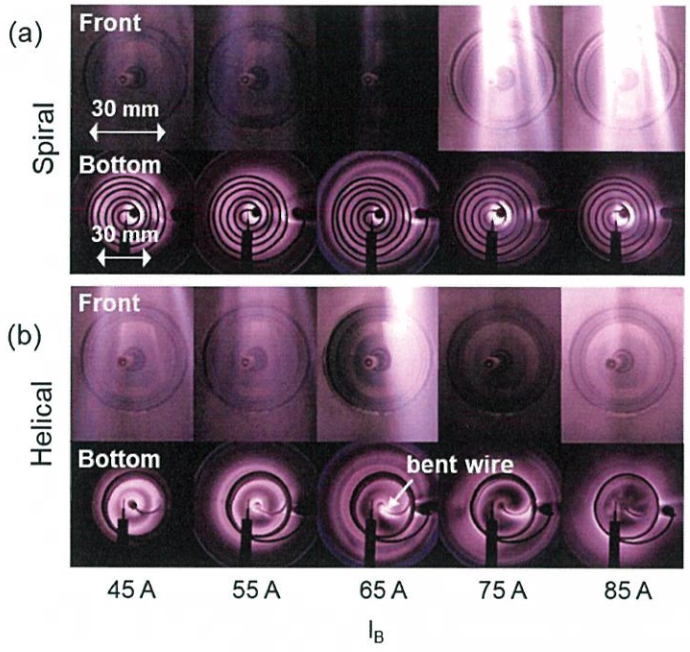

Fig. 4.18 Photos of plasmas produced using (a) spiral and (b) helical antennas, taken through the front and bottom viewports at various I_B.

The bottom-view photos reveal different plasma shapes over the range of I_B. When I_B was above 70 A, the plasma tended to concentrate at the front region of the antenna. When I_B was decreased below 70 A, the plasma formed rings close to the flange behind the antenna coil giving a dark silhouette appearance to it. Decreasing I_B below 60 A caused the rings to contract into a disc, which eventually decreased in radius until plasma suddenly disappeared. The occurrence of distinct plasma formations at changing I_B is associated to the confining effect of the induced magnetic field and coupling of the microwave power to the plasma.

Shown in Fig. 4.19a are luminosity spatial distributions of plasmas produced using spiral and helical antennas at I_B = 90 A. The helical antenna produced more radially

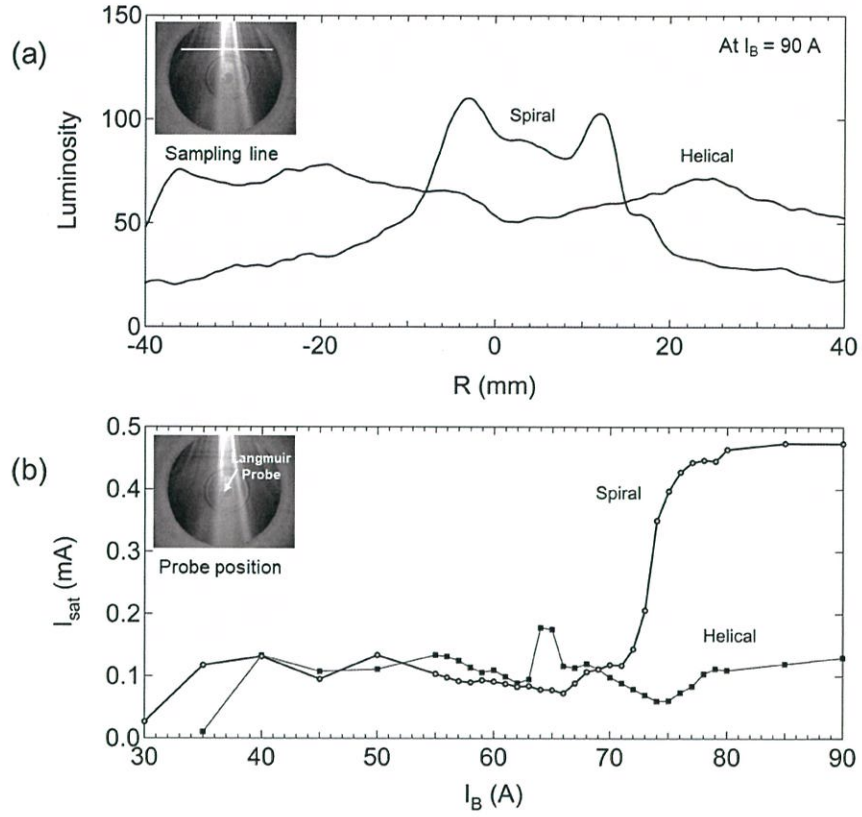

Fig. 4.19 (a) Luminosity spatial distribution of plasmas produced at 90 A, and (b) ion saturation current I_{sat} at various I_B for spiral and helical antennas.

uniform plasma than the spiral antenna. On the other hand, the spiral antenna produced plasma with higher intensity concentrated within 15 mm around the axis.

To see the effect of the antenna structure on plasma density, I_{sat} value from Langmuir probe measurement is plotted as a function of magnet current I_B, as shown in Fig. 4.19b. Above 70 A, higher I_{sat}, hence, plasma density, was measured with the spiral antenna. As observed in Fig. 4.19a, plasmas produced by the spiral antenna tended to concentrate near the chamber axis where the probe is located, causing high current measurements. The high-density region beyond 70 A was generated when plasmas diffused to the front region of the spiral antenna and into the process chamber.

A peaked range was observed between 60 and 70 A in the I_{sat} plot for the helical antenna. The peaks correspond to 64 and 65 A at which the resonance zone was about 20

mm below the antenna flange. In this area, the wire bending from the connector to the helical antenna is located. Consequently, discharges at such currents may have been capacitively driven by the high-voltage curved part of the helical antenna. As seen in Fig. 4.18b, the bent wire glowed brightly at 65 A when observed from the bottom viewport.

4.4.5 Effects of Number of Spiral Turns

In this series of experiments, insulated spiral antennas with D = 80 mm position were utilized to test the factors affecting their characteristic high-density mode beyond 70 A. To roughly estimate the plasma density, luminosity of plasma images taken through the front viewport were obtained as described in section 3.3. The mean luminosity of each image over a sampling area, about 25 mm below the source chamber, is plotted as a function of I_B. As seen in Fig. 4.20, the high-density mode is present in the luminosity plots of spiral antennas with number of turns n = 2, 4 and 6. The n = 2 antenna produced

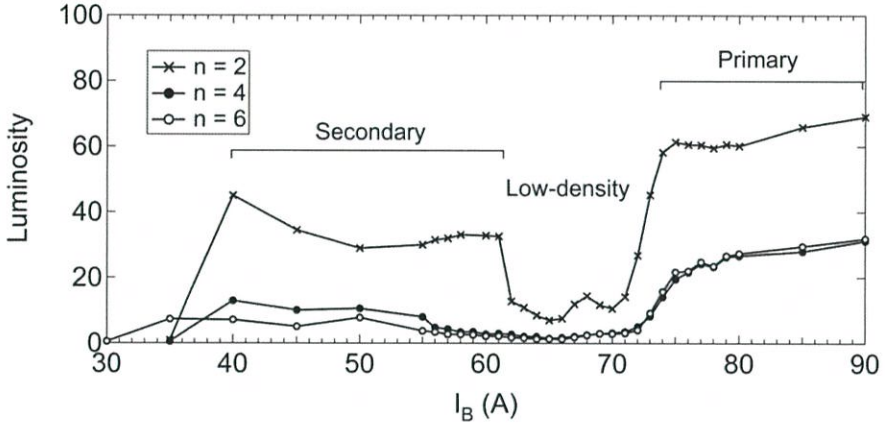

Fig. 4.20 Plasma image luminosity plotted as a function of I_B for plasmas produced using spiral antennas with different number of turns n.

much brighter plasma possibly due to its less number of turns, causing the formation of smaller plasma sheath near the antenna.[17] It resulted in a decreased loss of ion energy across the sheath, which in turn, leads to higher plasma density. It can be observed that the luminosity plot for n = 2 has two high-density modes: the primary and secondary

regions at about $I_B > 70$ A and $I_B < 60$ A, respectively, and a low-density mode between 60 and 70 A. The observed discontinuities in the plasma parameter plots and distinct change in the plasma shape in varying magnetic field are indications of plasma mode transitions.[46]

4.4.6 Effects of Antenna Position

The observed mode transitions are further examined by changing the position D of the insulated, n = 2 spiral antenna relative to the antenna flange. D was varied by changing the length of the antenna stem as show in Fig. 4.12a. As observed in Fig. 4.21, the dependence of luminosity and I_{sat} on magnet current I_B evolves as position D varies.

When D was increased, luminosity and I_{sat} values at $I_B \geq 73$ A also increased. At 60 mm and above, the values began to saturate at 73 A. In contrast, the values started to drop at

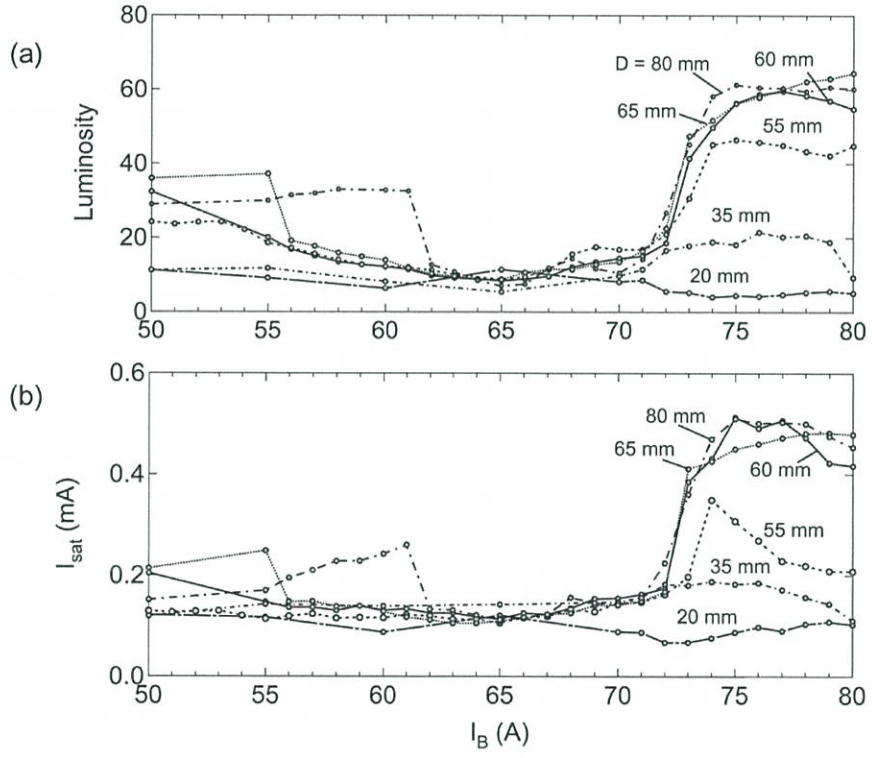

Fig. 4.21 (a) Plasma image luminosity and (b) ion saturation current I_{sat} plotted as functions of I_B for plasmas produced using n = 2 spiral antenna at various position D.

75 A when the antenna position is at 55 mm. In Fig. 4.22, bottom photos reveal that the main difference of the 55-mm from the 60-mm antenna is the development of a hole in the plasma discharge from 75 A. The hole formed near the region where the probe was located resulting in low I_{sat} measurements. The origin of the hole formation is yet being investigated. Such distinct change that occur when D = 60 mm, implies that the length of the antenna stem plays a significant role in sustaining the high-density mode at $I_B \geq 73$ A.

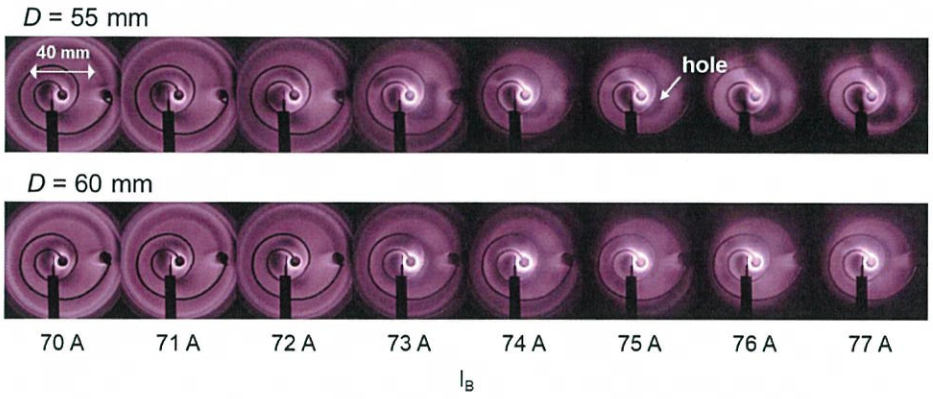

Fig. 4.22 Plasma photos taken through the bottom viewport at various I_B for spiral antenna position D = 55 and 60 mm.

Similar effect of the antenna stem on plasma density was previously observed in section 4.4.1, where plasmas were produced using different antenna flange configurations. Recall that in mid and near configurations, high plasma density was obtained when I_B was above 70 A. This can be attributed to the length of the antenna stem utilized in the experiment: 53 and 88 mm for mid and near configurations, respectively. For the mid configuration, its 53-mm-long antenna exhibited similar density profile with the antenna with D = 55 mm, in which density values dropped beyond 75 A. As expected, the 88-mm-long antenna demonstrated similar density profile with the antennas having $D \geq 60$ mm. On the other hand, the 13-mm-long antenna utilized in far configuration exhibited low-density profile above 70 A, since the stem was much shorter than 60 mm, as with the case of the antenna with position D = 20 mm.

4.5 Discussion

Let z_{res} be defined as the distance from the base of the antenna flange at which the magnetic field intensity satisfies the ECR condition (B = 87.5 mT) along the chamber axis. The position of the ECR zone z_{res} was obtained based on the axial profile of the magnetic field at different magnet current I_B shown in Fig. 4.7b. To better understand the geometrical arrangement of the spiral antenna, with D = 60 mm, with respect to the position of the ECR zone, the schematic diagram of the antenna is overlaid on z_{res} plotted as a function of I_B, as shown in Fig. 4.23.

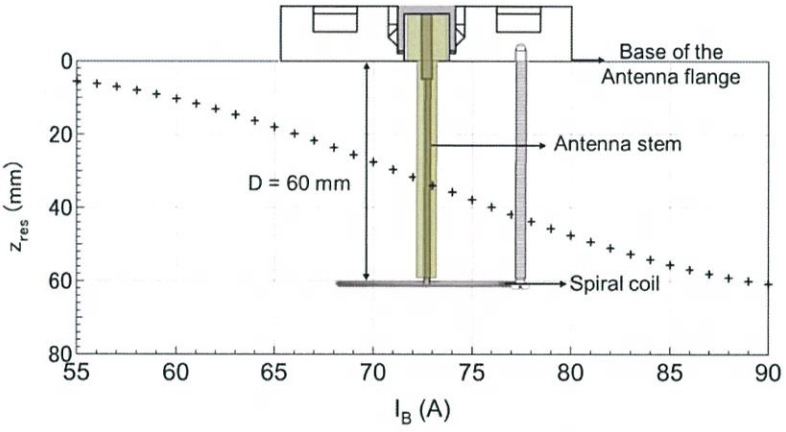

Fig. 4.23 Distance z_{res} at which the ECR field is created along the chamber axis measured from the base of the antenna flange plotted as a function of I_B.

At 73 A, z_{res} is around 34 mm from the antenna flange. Note that for microwave with 2.45 GHz frequency, the wavelength λ is about 120 mm. Hence, the length of the antenna stem at 30 mm is approximately quarter of a wavelength. The 60-mm stem of the spiral antenna could have served as a dipole antenna, which radiated maximum power near z_{res} at 73 A mm, as illustrated in Fig. 4.24. It resulted in highly efficient power absorption over the entire cross section of the resonance zone at 73 A, which caused a jump in the density measurements and launched the primary high-density mode. Above 73 A, the ECR zone is close to the spiral coil, which emits peak radiation perpendicular to the spiral

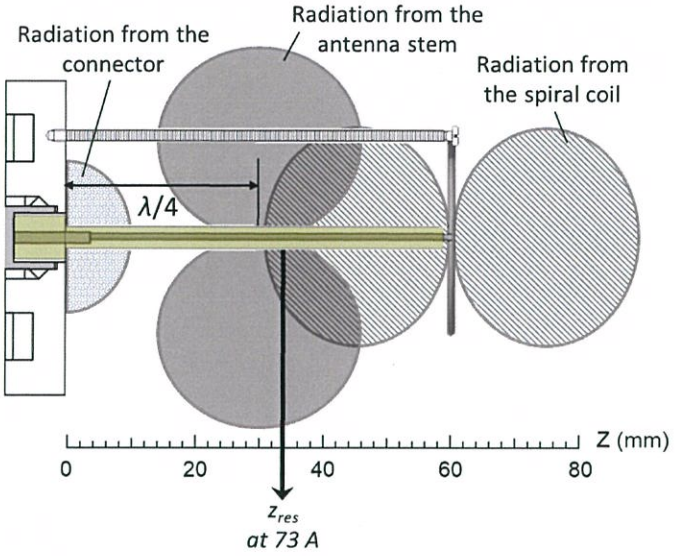

Fig. 4.24 Radiation pattern of the spiral antenna relative to the axial distance of the ECR zone from the antenna flange z_{res}.

plane. The superposition of radiation from the stem and the spiral coil in this region could have sustained high ionization beyond 73 A.

When the magnet current was decreased below 73 A, z_{res} began to move closer to the antenna flange, away from the location at which maximum power was radiated, causing poor microwave absorption in the resonance zone. The absorbed microwave power could have decreased below the minimum level to sustain an inductive coupling between the plasma and the antenna, as discussed in section 2.7. Consequently, the plasma exhibited transition to a low-density state, which is a manifestation of an inductive to capacitive coupling transition.

The secondary high-density mode was formed when I_B was decreased below 60 A. This mode extends to currents below 55 A, which was the minimum magnet current to satisfy ECR condition. Clearly, high-density measurements below 55 A was not due to electron cyclotron heating of electrons. Instead, plasma discharges at such low currents could have been capacitively driven by the microwave power radiated from the connector that resembles a dielectric resonator antenna, as illustrated in Fig. 4.24.

To evaluate the extent of the effect of position D on plasma density, insulated circular and linear antennas with D = 65 mm are compared to the spiral antenna with the same position. Luminosity plots of plasmas produced using spiral, circular and loop antennas are superimposed in Fig. 4.25a. Plasmas produced by the linear and loop antennas also demonstrate the primary high-density mode above 70 A. However, unlike the spiral antenna, they barely exhibit the secondary high-density mode below 60 A. In addition, their luminosities above 70 A escalate gradually at increasing I_B, as oppose to the abrupt increase in the spiral antenna plot. These can be manifestations of high power dissipation in ohmic losses, as discussed in section 4.2.4, in the circular and loop antennas.[49]

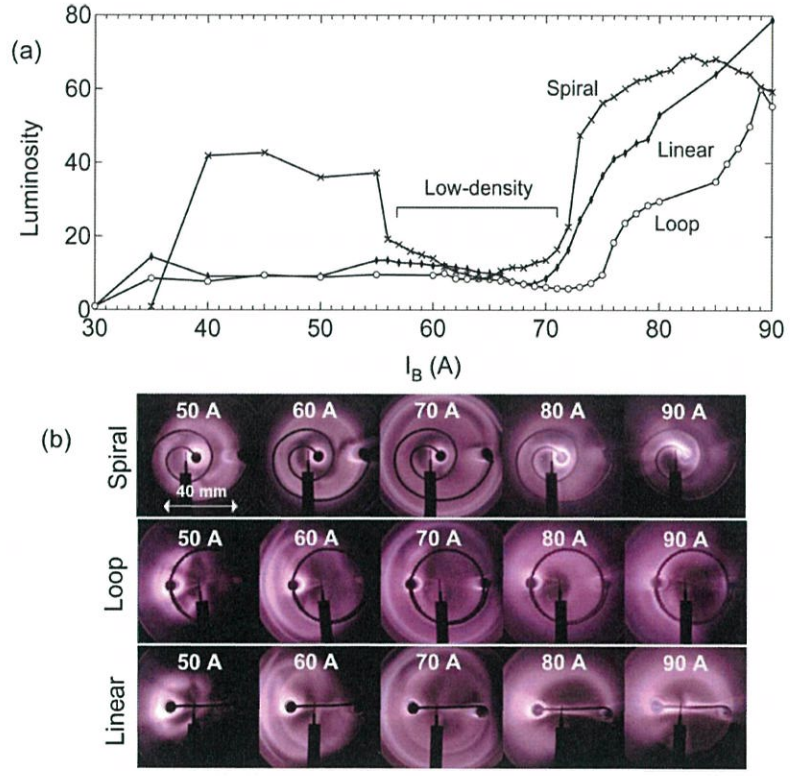

Fig. 4.25 (a) Plasma image luminosity and (b) bottom-view photos at various I_B for plasmas produced using different antenna structures with D = 65 mm.

The luminosity plots of the three antenna structures exhibit the low-density mode. It can be observed in the bottom-view photos in Fig. 4.25b that the low-density mode is initiated by the formation of plasma rings near the flange at around 70 A. As soon as the

rings were formed, plasma luminosity captured from the process chamber dropped. Decreasing I_B by several amperes caused the luminosity to increase once the plasma rings had contracted. In the case of the loop and linear antennas, plasma tended to move towards the connector at the left side, where the electric field was stronger.

In Fig. 4.26, the dependence of the low-density mode on forward microwave power P_f is displayed. The spiral antenna with n = 2 and D = 65 mm was utilized. The minimum I_B to sustain the plasma increased as P_f was reduced. Stronger magnetic confinement is required to compensate diffusion loss of plasma particles to the chamber walls.[50] As P_f was increased, the density of ionized particles also increased, resulting in heightened depth and shortened length of the low-density mode. Increasing the power to 140 W provided sufficiently high energy to overcome this low-density or capacitive mode.

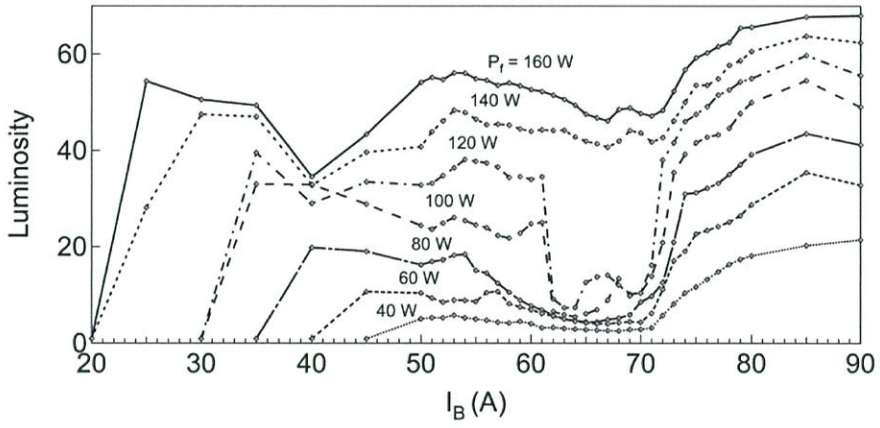

Fig. 4.26 Plasma image luminosity plotted as a function of I_B for plasmas produced using spiral antenna at various forward microwave power P_f.

The electric field from the antenna that crosses the static magnetic field and reaches the resonance zone is absorbed. When the incident microwave is poorly absorbed by the plasma near the resonance zone, it propagates into the chamber. Thus, such transmitted power was detected using a receiving antenna located in the process chamber, as described in Fig. 3.13. At P_f = 100 W, the image luminosity of plasmas was monitored

simultaneously with the reflected and transmitted power. Less than 1% reflected power was measured in high- and low-density modes, as seen in Fig. 4.27a. The relationship between luminosity and transmitted microwave power detected in the chamber is presented in Fig. 4.27b. Low MW transmission was observed when I_B was below 60 A and above 70 A which correspond to primary and secondary high-density modes, respectively.

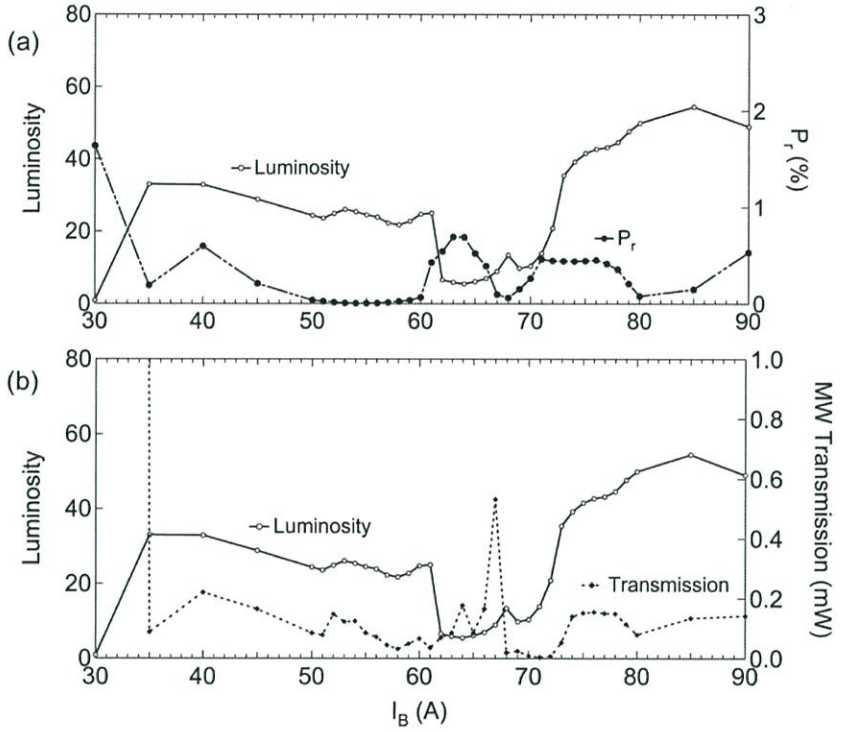

Fig. 4.27 Plasma image luminosity with (a) reflected power P_r and (b) MW transmission plotted as functions I_B for spiral antenna.

Note that low transmission implies high dissipated power. In this case, microwave power was radiated by the antenna and efficiently absorbed by the plasma which resulted in high degree of ionization. High transmission was detected between 60 and 70 A where low luminosity values were measured. It is an indication of poor power absorption of the plasmas. It supports the assumption that these plasmas were generated through capacitive coupling which resulted in the formation of the low-density mode. Decreasing I_B from 74 to 70 A caused a steep descent in the luminosity and MW transmission. This time, power was neither absorbed effectively by the plasma nor

transmitted into the vacuum chamber. Instead, power could have been dissipated within the antenna line. The steep descent near 70 A is also evident in the superimposed and vertically shifted transmission profiles of plasmas generated at different forward power shown in Fig. 4.28. As P_f was increased, the descent gradually vanished. At 140 W, this descent which characterized the transition from primary high- to low-density mode was no longer observed, since the power was enough to eliminate the low-density mode as shown in Fig. 4.26. Additionally, the peak transmission found between 60 and 70 A disappeared as P_f was increased to 140 W.

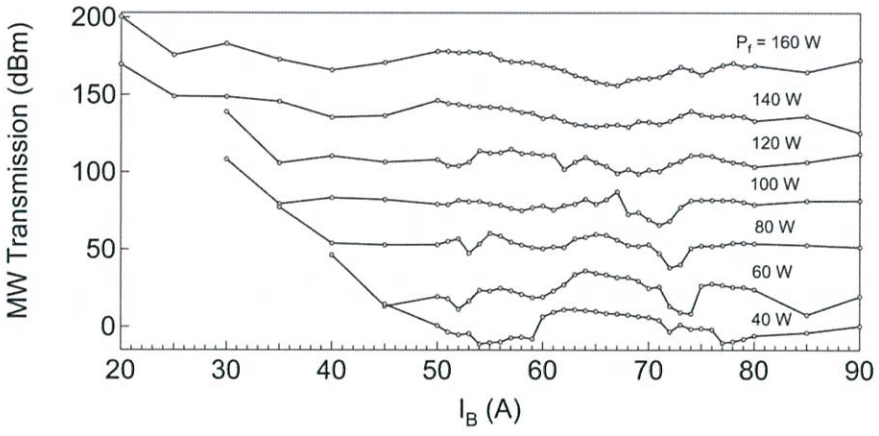

Fig. 4.28 Vertically shifted MW transmission plotted as functions of I_B at various forward microwave power P_f.

4.6 Conclusion

Good microwave coupling was achieved between plasmas and internal antennas in ECR and sub-ECR condition by optimizing the magnet current and the antenna structure. The position of the spiral antenna with respect to the antenna flange, which is associated to the length of the antenna stem, plays a significant role in producing a stable high-density mode at 73 A and above. Transition from inductive to capacitive coupling mode occurred below 73 A which produced a low-density mode with poor microwave absorption.

Chapter 5

Properties of ECR Plasma Generated using Carbon Internal Antenna

5.1 Introduction

Internal antennas of different structures were used to introduce microwave power into electron cyclotron resonance plasma sources without dielectric windows to avoid accumulation of conductive layers on the window that prevents further injection of power.[18-20] The antennas were able to efficiently transfer microwave power and sustain stable ECR discharges suitable for film deposition. However, parts of these antennas protruding directly into the plasma space were made of stainless steel. Sputtering of antenna wall surfaces by high-density plasmas in ECR sources can result in metal contamination. Therefore, it is strategic to cover the internal antenna with the same material being deposited, particularly, carbon in this study. To explore such possibility, this chapter gives an evaluation on the performance of internal antennas made of graphite material in microwave coupling and ECR plasma excitation. The effects of plasma conditions, antenna structure and magnetic configuration on plasma parameters and properties are investigated using image luminosity capture, Langmuir probe analysis, and reflected and transmitted power measurements.

5.2 Materials and Methods

5.2.1 Antenna Structure

In the preceding chapter, results show that the insulated 2-turn spiral antenna with position D = 60 mm produced high-density plasmas with good microwave absorption. Hence, one of the carbon internal antennas tested in this chapter was fabricated based on the same antenna parameter. Shown in Fig. 5.1, are the three carbon antennas that were tested, namely: spiral, loop and coaxial. The carbon spiral antenna was attached to the N-type connector using a 6-mm-diameter carbon stem. A low-thermal expansion borosilicate glass tube was used to shield the stem and the inner wall of the connector. The other end of the antenna was also attached to a 6-mm-diameter grounded carbon stem. As for the carbon coaxial antenna, a carbon rod with 12-mm height and 12-mm diameter served as its inner electrode. The inner electrode was screwed to a shielded stainless steel joint attached to the N-type connector. The 44-mm-diameter grounded outer electrode was separated from the inner electrode by 2 mm. The upper 1.7 cm of the

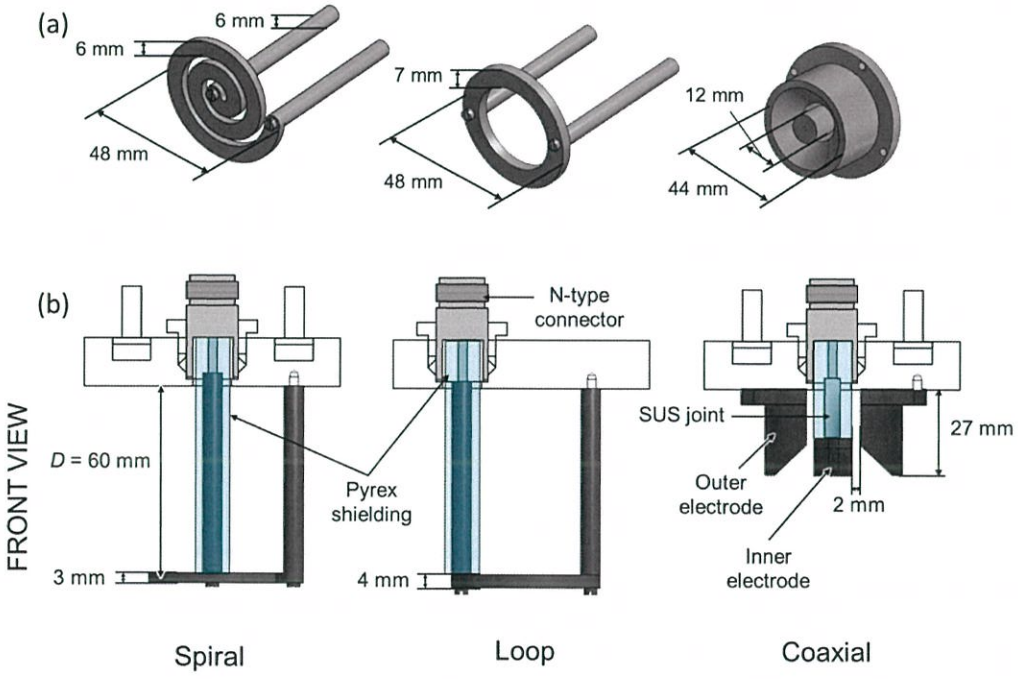

Fig. 5.1 (a) Carbon antenna structures with their corresponding parameters. (b) Front view diagram of the antennas.

inner wall of the outer electrode is cylindrical, while the bottom 1 cm of the inner wall is conical, as illustrated in Fig. 5.1b, so that the produced plasma exits the antenna along the linear magnetic field generated by the electromagnet. On the other hand, the carbon loop antenna was attached to the flange with an off-centered connector unlike the spiral and coaxial antennas. The loop antenna has 48-mm outer and 34-mm inner diameters, and was joined to two 6-mm-diameter stems, one was shielded and attached to the connector and the other was attached to the grounded flange.

5.2.2 Magnetic Field Configuration

Electromagnet coils were placed around the plasma production chamber, which generated a divergent magnetic field downward, as illustrated in Fig. 5.2a. In section 5.3.4, the magnetic field configuration was modified by attaching the temporary magnets, described in section 3.1.3, to the electromagnet. They served as a magnetic flux return which swallowed some of the divergent fields produced by the electromagnet, directing them away from the chamber axis, as shown in Fig. 5.2b. The magnetic field intensity along the chamber axis varied with the current supplied to the electromagnet I_B (magnet current), as seen in Fig. 5.3. The intensity profiles in the cases with and without the flux return include the magnetic field contribution of the permanent magnet placed 15 mm

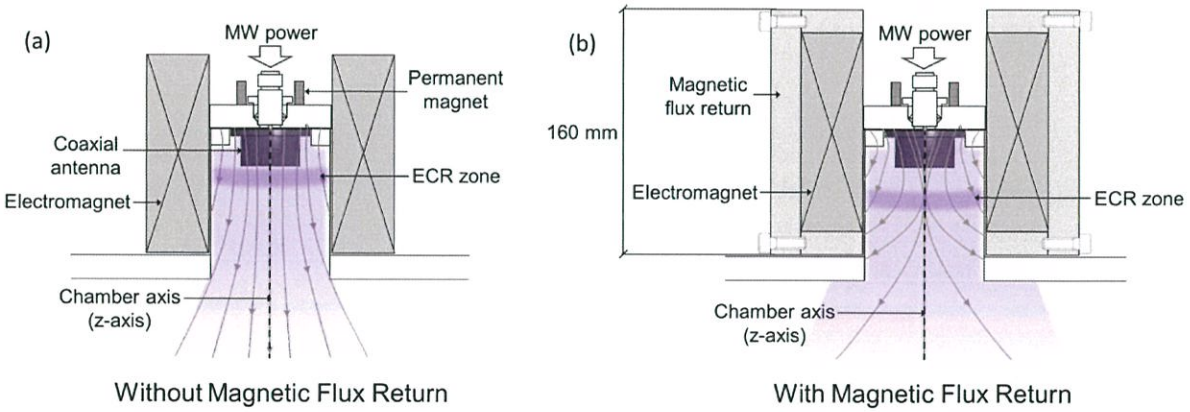

Fig. 5.2 Source chamber with (a) electro- and permanent magnets, and (b) with additional magnetic flux return.

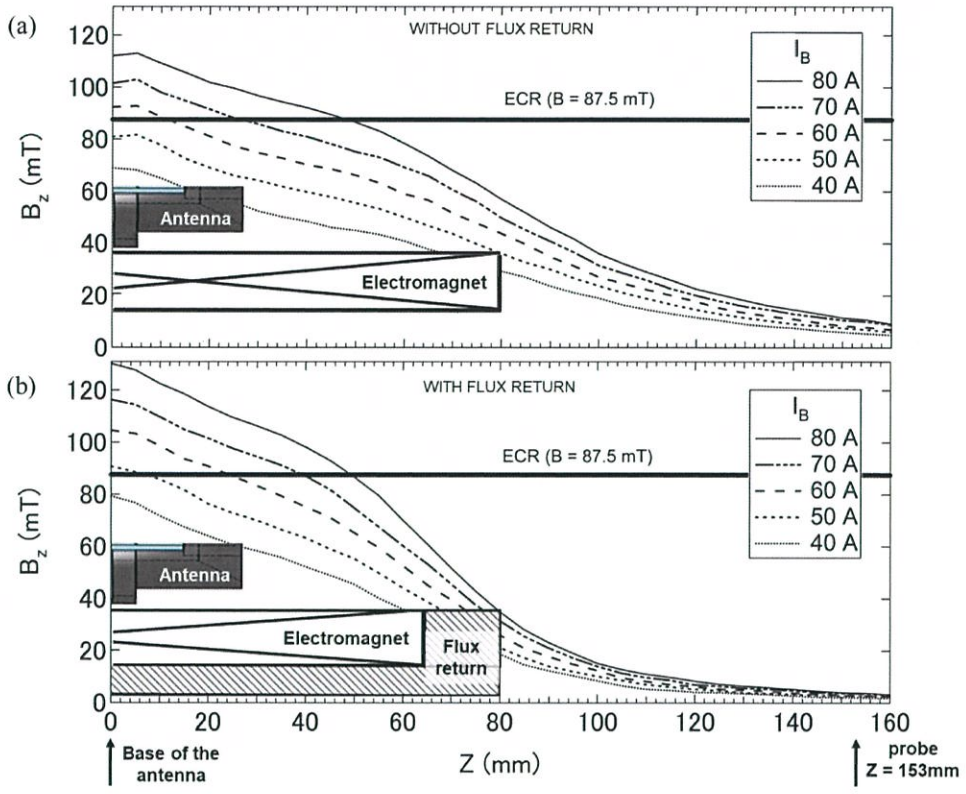

Fig. 5.3 Magnetic field intensity profile along the chamber axis at different magnet current I_B (a) without and (b) with the magnetic flux return. (Effect of the permanent magnet is included)

above the antenna. Without the flux return, the ECR condition for 2.45 GHz frequency was satisfied when the magnetic field intensity is 87.5 mT at current $I_B \geq 55$ A. In the presence of a flux return, the ECR condition was attained at $I_B \geq 49$ A.

5.3 Results

5.3.1 Effects of Magnet Current

Shown in Fig. 5.4, are images of plasmas produced using the carbon spiral, loop and coaxial antennas at various magnet current I_B. Photos were taken through the front viewport facing the region below the gas ring, and through the bottom viewport along the axial axis of the vacuum chamber. The forward power and hydrogen pressure were set at 100 W and 1 Pa, respectively. It can be observed that plasmas produced by the loop

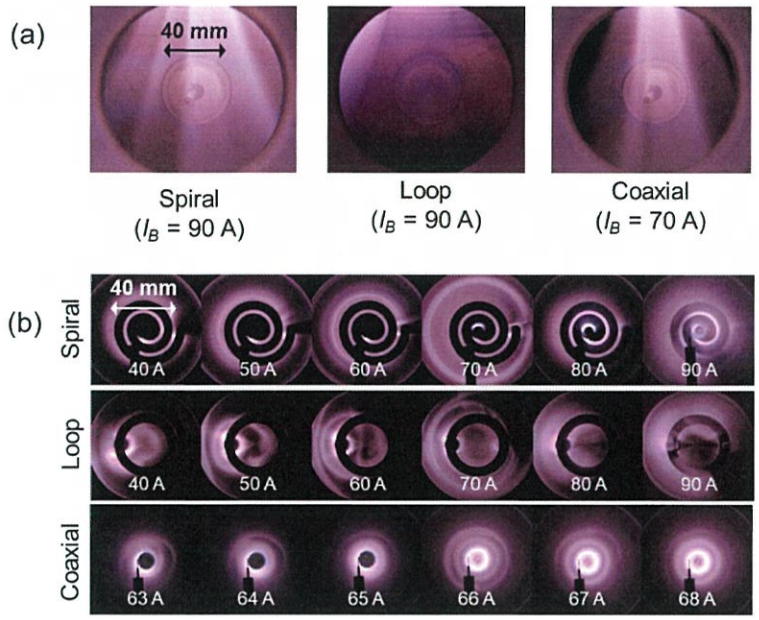

Fig. 5.4 Images taken through the (a) front and (b) bottom viewports at various I_B for plasmas produced using different carbon antenna structures.

antenna tended to converge at the side of the chamber near the connector, which made it difficult to compare plasma parameters measured through the probe located at the chamber axis. For this reason, luminosity of plasma images taken through the front viewport was used to roughly estimate the plasma density, as discussed in section 3.3. The mean luminosity over a sampling area, about 25 mm below the source chamber, is plotted as a function of I_B in Fig. 5.5. Plasmas produced using the spiral and loop antennas

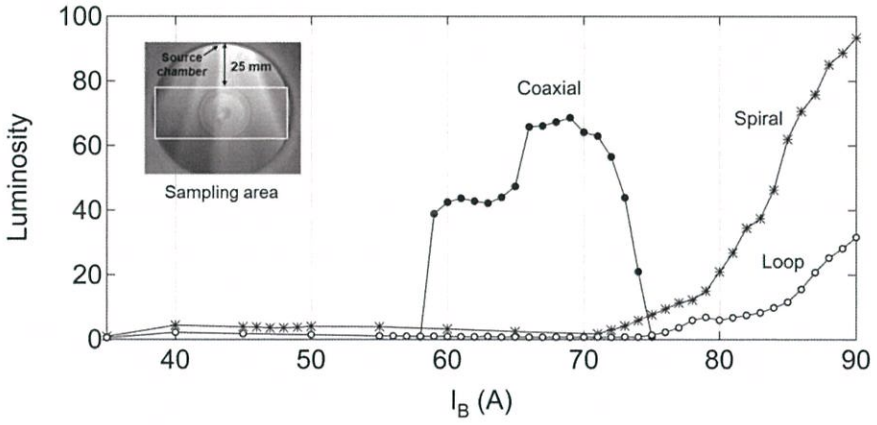

Fig. 5.5 Plasma image luminosity plotted as a function of I_B for plasmas produced using different carbon antenna structures.

exhibit high-density mode above 70 A, which was also observed in the plasmas produced using the nickel spiral antenna (see Fig. 4.21b). However, with the carbon antennas, the luminosity values manifested a gradual increase when I_B was set above 70 A, which is different with the jump observed with the nickel spiral antenna. In addition, the secondary high-density mode observed at currents below 60 A with the nickel spiral antenna was not observed with the carbon antennas. These may have been caused by a contact resistance between the steel N-type connector and the carbon stem attached to it.

Bottom-view photos in Fig. 5.4b show that at sufficiently high magnet current, plasmas formed at the front region of the carbon antennas, giving high plasma image luminosities in Fig. 5.5. At 70 A, plasma rings formed behind the spiral antenna, which resulted in considerably low luminosity values. As in the case of the nickel spiral antenna, this indicates capacitive coupling between the carbon spiral antenna and the plasma. Since plasmas produced by the loop antenna tend to concentrate near the connector, away from the substrate region, only the coaxial and spiral antennas were compared in the following characterizations. The plasma parameters were obtained based on the measurements done using the Langmuir probe inserted radially into the process chamber,

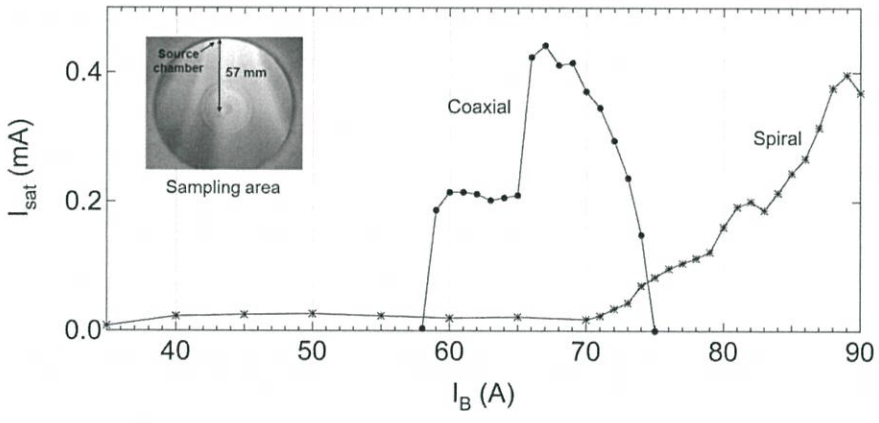

Fig. 5.6 Ion saturation current I_{sat} plotted as functions of I_B for plasmas produced using carbon coaxial and spiral antennas.

57 mm below the source chamber or 153 mm below the antenna flange. Displayed in Fig. 5.6 is the dependence of ion saturation current I_{sat} on magnet current I_B. Based on Eq. (3.14), the measured I_{sat} is approximately proportional to electron density n_e. The coaxial antenna exhibited a peaked I_{sat} profile with the highest value at around 67 A. The effect of the position of the resonance zone z_{res} on plasma density for carbon coaxial and spiral antennas is discussed in section 5.4.

Fig. 5.7 shows the variation of plasma potential V_{pl} and electron temperature T_e with current I_B. The average T_e obtained was 1 V. Recall that high I_{sat} value for coaxial and spiral antennas occurs around 67 and 89 A, respectively. Lower V_{pl} was measured in the plasma produced by the coaxial antenna at 67 A than that of the spiral antenna at 89 A. Such low V_{pl} measured in coaxial-antenna-produced plasma results in decreased impact energy of the ions to the deposition substrate, hence, reducing substrate damage.

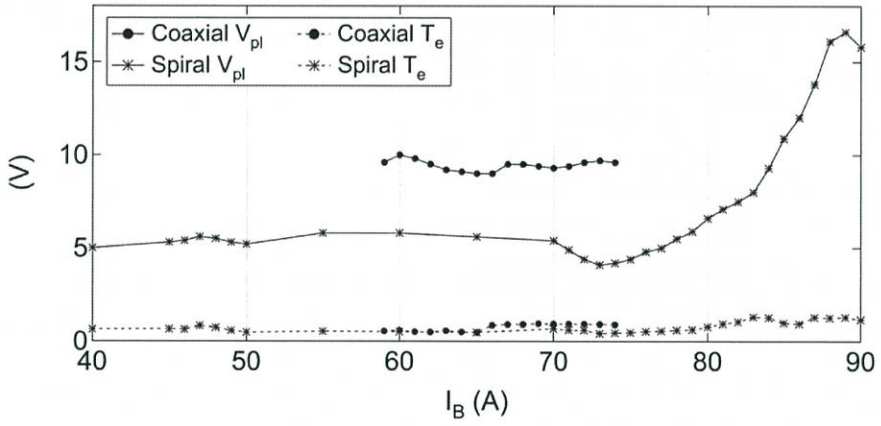

Fig. 5.7 Plasma potential V_{pl} and electron temperature T_e and plotted as functions of I_B for plasmas produced using carbon coaxial and spiral antennas.

To see the effect of the magnet current on plasma uniformity, spatial distribution of plasma luminosity taken through the front viewport was obtained at various I_B in Fig. 5.8. The luminosity distribution was evaluated along a horizontal line about 20 mm below the source chamber. The coaxial antenna generated more uniform plasma over an area with about 40 mm diameter. On the other hand, the spiral antenna produced more dispersed

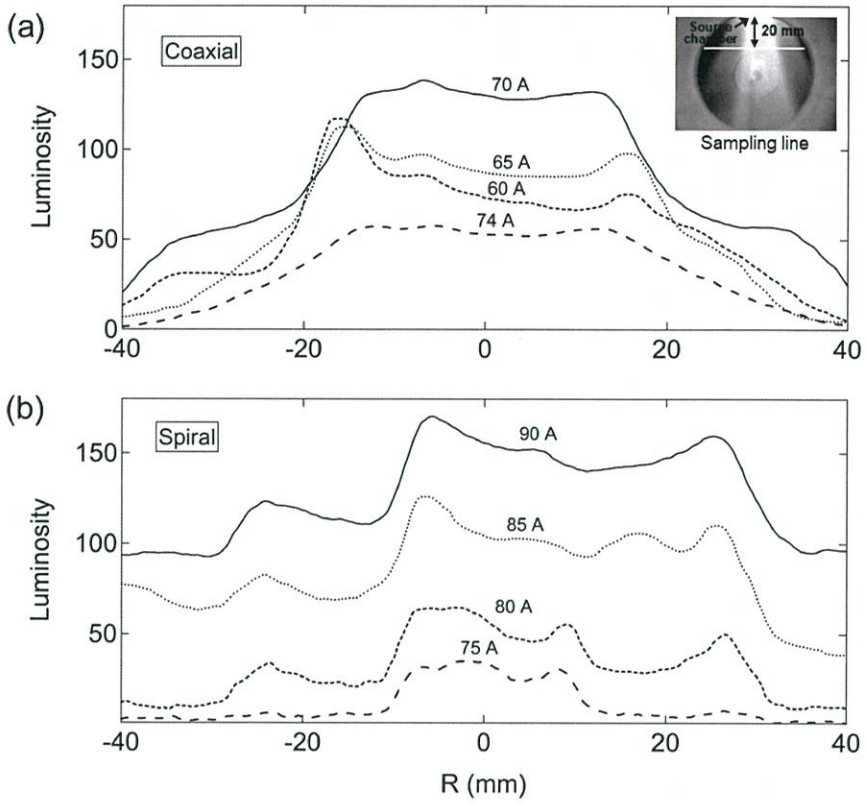

Fig. 5.8 Luminosity spatial distribution of plasmas produced using carbon (a) coaxial and (b) spiral antennas at various I_B.

plasmas due to the large surface area of its spiral arms. The spatial distribution for the coaxial antenna shows a bright central region and a faint peripheral region. The bright region is considered to be due to the direct plasma flow along the magnetic field lines. The clear edge of the plasma glow observed at the exit of the source chamber indicates that plasma was directly colliding with the side walls, and the reflected charged particles form the plasma in the peripheral region. Fig. 5.8 also indicates that there is some inhomogeneity in the plasma column streaming out of the source chamber. A change in the microwave absorption condition is known to cause this plasma inhomogeneity,[51] which can be seen in Fig. 5.9 for different I_B values.

Transmitted power was detected simultaneously with plasma image luminosity using the receiving antenna installed in the process chamber, as shown in Fig. 3.13. The

intensities of the detected 2.45 GHz wave and its second harmonic at 4.90 GHz are plotted for various I_B in Fig. 5.9a and b for coaxial- and spiral- antenna-produced plasmas, respectively. Superimposed in the figure is the plasma image luminosity, which was simultaneously captured while measuring the transmitted power. The absorption of 2.45 GHz wave is in good agreement with the I_{sat} and luminosity data in Fig. 5.6 and Fig. 5.9, respectively. Larger transmitted power detected when the spiral antenna was used indicates poor microwave power coupling to the plasma.

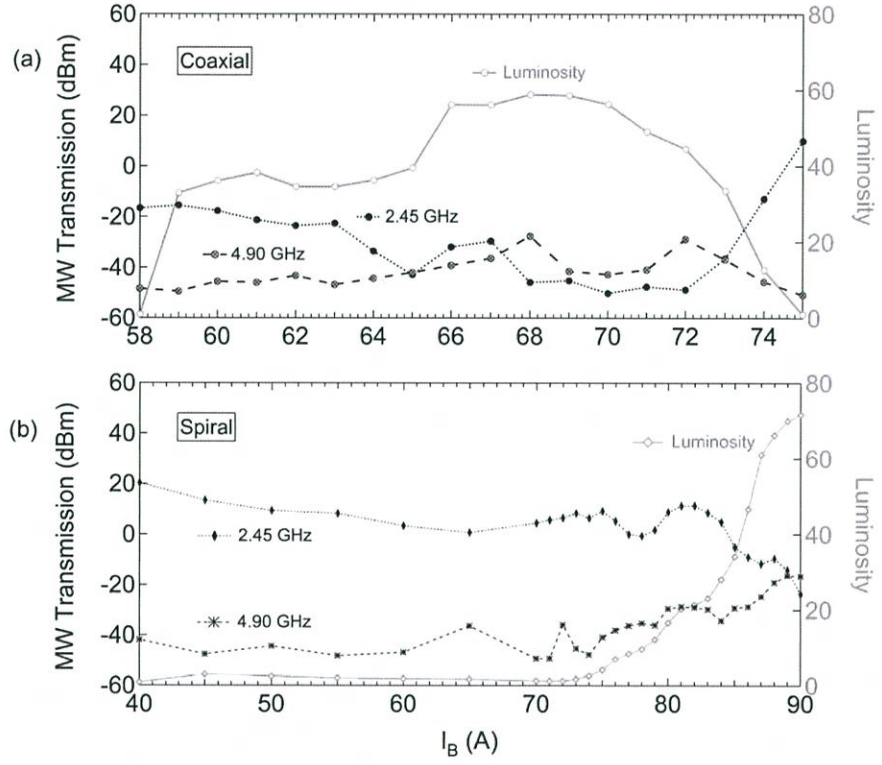

Fig. 5.9 MW transmission of 2.45 and 4.9 GHz waves with plasma image luminosity for plasmas produced using carbon (a) coaxial and (b) spiral antennas.

5.3.2 Effects of Hydrogen Pressure

The dependence of ion saturation I_{sat} and plasma potential V_{pl} on hydrogen gas working pressure is shown in Fig. 5.10. The magnet current I_B was set at 70 and 90 A for coaxial and spiral and antennas, respectively, since they correspond to nearly equal I_{sat} values as seen in Fig. 5.6. Highest I_{sat} value was obtained at 0.8 and 2 Pa for coaxial- and

spiral- produced plasmas, respectively. At higher pressures, measured V_{pl} increased due to frequent electron-neutral collisions causing diffusive loss of the electrons. On the other hand, I_{sat} decreased at higher pressures due to short mean free path which results in less ionizing collisions, hence, giving low current measurements in the downstream region.

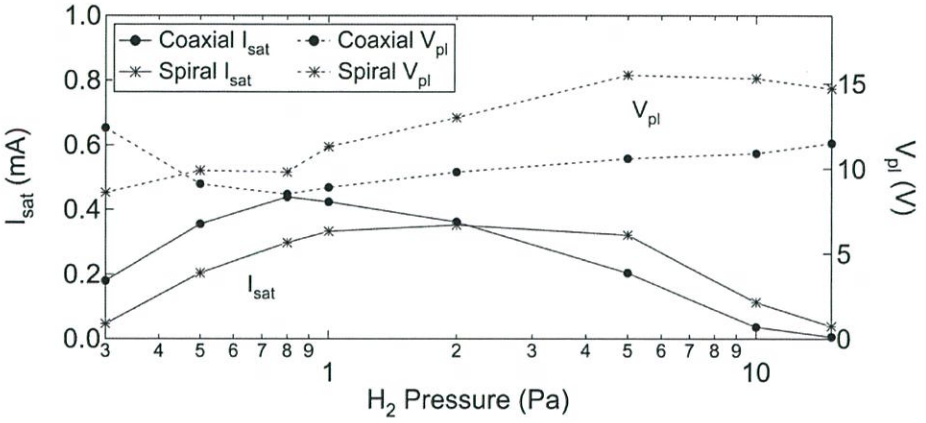

Fig. 5.10 Ion saturation current I_{sat} and plasma potential V_{pl} plotted as functions of H_2 pressure for plasmas produced using carbon coaxial and spiral antennas.

When plasmas are viewed from the bottom port, as displayed in Fig. 5.11, it is evident that plasmas produced at high pressures were brighter, and thus approximately denser. Plasmas at high pressures, however, were concentrated close to the microwave antenna and their plasma densities decay significantly along the chamber axis, as observed in the luminosity spatial distribution in Fig. 5.12. The higher the working pressure, the shorter the decay length becomes. The luminosity distribution was taken along a vertical line drawn on photos taken through the front viewport. Since the sampling line starts 100

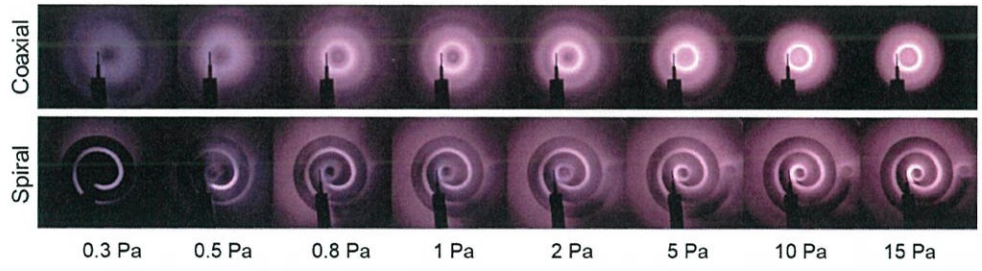

Fig. 5.11 Bottom-view photos of plasmas at various H_2 pressures produced using carbon coaxial and spiral antennas.

mm below the antenna flange, the bright plasmas observed near the antenna at high pressures are not evident in the luminosity distribution.

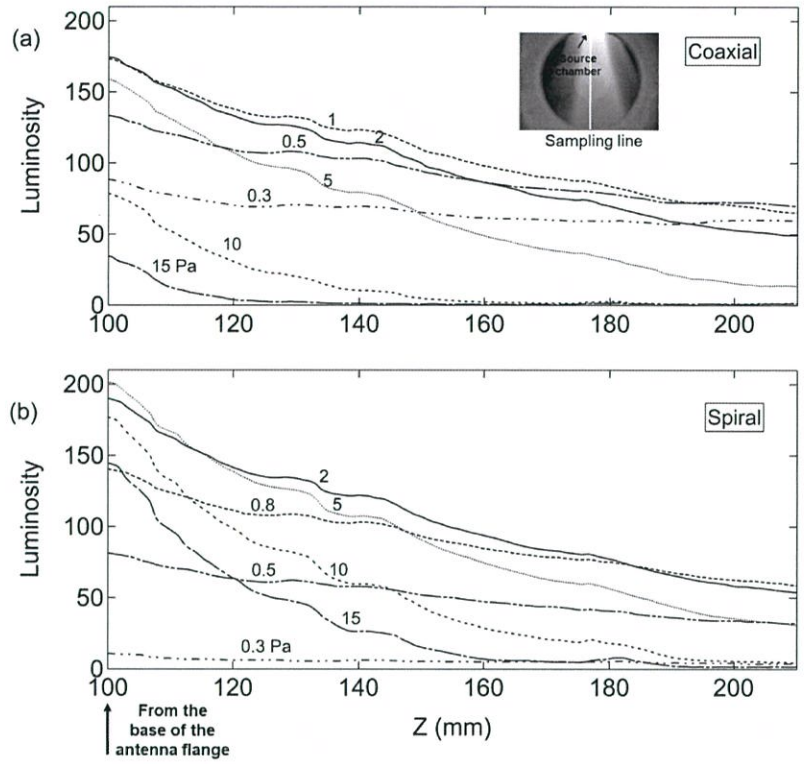

Fig. 5.12 Luminosity spatial distribution along a vertical line at various H_2 pressures for plasmas produced using carbon (a) coaxial and (b) spiral antennas.

5.3.3 Effects of Microwave Power

Here, the hydrogen pressure was fixed at 1 Pa. As the microwave forward power P_f was increased, the electron density n_e of plasmas produced using the carbon antennas also increased, as seen in Fig. 5.13a. The rate of increase in n_e with P_f for the coaxial antenna is higher than that for the spiral antenna. At 120 W, the coaxial antenna began to produce overdense plasmas with densities above the critical density n_c.

Using Eq. (2.1) and (2.4), the critical density for an incident wave with f = 2.45 GHz frequency, is given by,

$$\omega = 2\pi(2.45 \times 10^9) = 1.54 \times 10^{10}\ \text{Hz} \qquad (5.1)$$

$$n_c = \frac{m_e \epsilon_0 \omega^2}{e^2} = 7.5 \times 10^{16}\ m^{-3} \quad (5.2)$$

In both cases, the electron temperature T_e is nearly constant at 1 V with increasing P_f, as seen in Fig. 5.13b. The plasma potential V_{pl} is nearly steady at 9.5 V, for the coaxial antenna. Conversely, V_{pl} increased with P_f in the case of the spiral antenna, which is attributed to the more diffuse plasma this antenna generated.

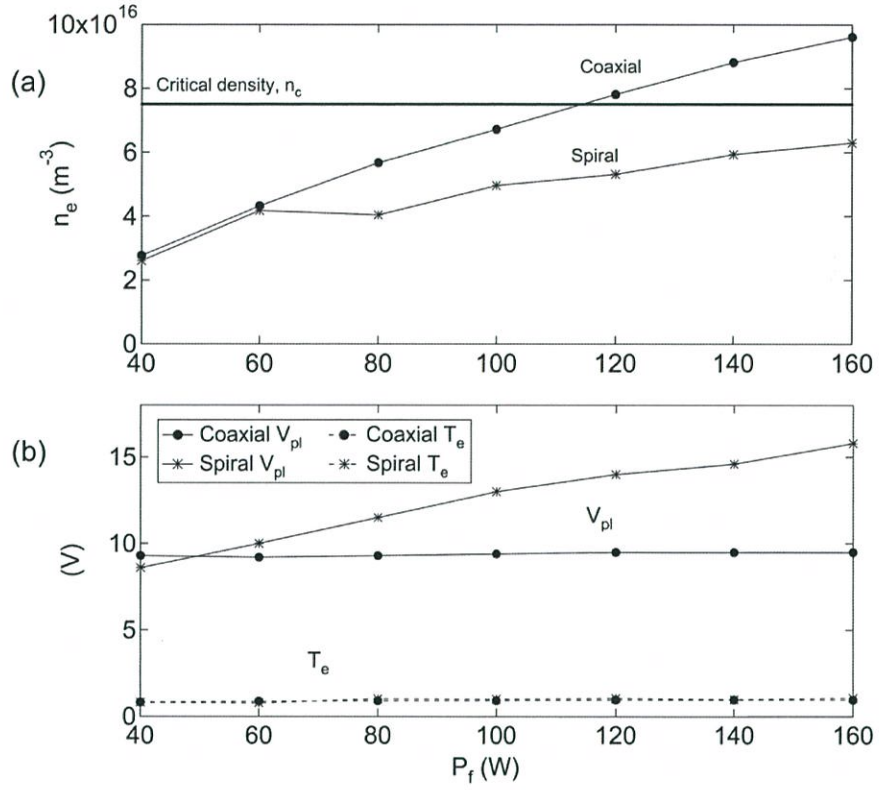

Fig. 5.13 (a) Electron density n_e, (b) and plasma potential V_{pl} with electron temperature T_e plotted as functions of forward power P_f for plasmas produced using carbon coaxial and spiral antennas.

5.3.4 Effects of Magnetic Flux Return

As seen in Fig. 5.8, the coaxial antenna produced more uniform plasmas than the spiral antenna. However, the plasmas were only about 40 mm in diameter which is relatively low for large-area deposition. Moreover, the plasma density at the substrate region was too high that it may cause film erosion. To tune the plasma properties for film deposition, the magnetic field configuration was modified by adding temporary magnets,

which are described in section 3.1.3. The temporary magnets were attached around the electromagnet, as illustrated in Fig. 5.2b, to serve as a magnetic flux return. As seen in Fig. 5.14a, the addition of flux return effectively decreased the current I_{sat} measured at the downstream region. High I_{sat} values were obtained when I_B was above 55 and 64 A, in with- than in without-flux-return (FR) case, respectively. As I_B was changed, I_{sat} also varied. Such behavior is attributed to the influence of I_B on the position of the resonance zone z_{res} with respect to the antenna geometry, which is discussed in section 5.4.

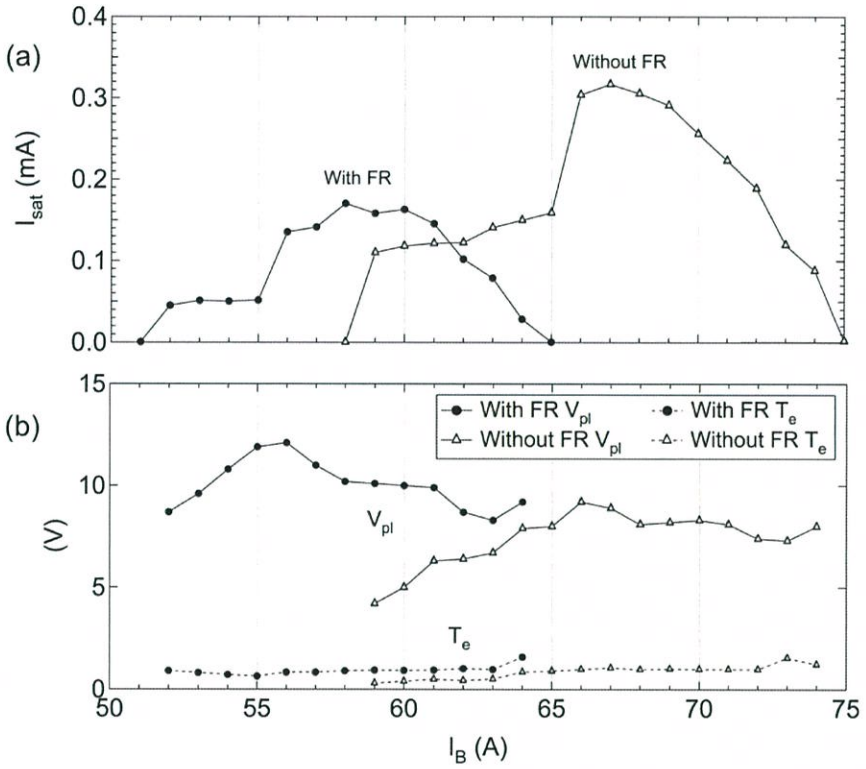

Fig. 5.14 (a) Ion saturation current I_{sat}, (b) plasma potential V_{pl} and electron temperature T_e plotted as functions of I_B in the cases with and without flux return (FR).

Since plasma potential V_{pl} and electron temperature T_e were found to be significant factors in thin film deposition using ECR plasma,[13,52] the dependence of V_{pl} and T_e on current I_B is plotted in Fig. 5.14b. The average T_e in both cases was about 1 V. When the flux return was present, V_{pl} increased by about 25%. Such relatively higher V_{pl} is attributed to the more diffuse plasma produced with flux return which is evident in the

luminosity spatial distribution in Fig. 5.15. It resulted in uniform plasma with diameter of about 60 mm, which is 50% larger than that of observed when there was no flux return.

As the flux return swallowed some of the divergent fields produced by the electromagnet, the magnetic field further decreased along the chamber axis causing the plasma to expand and the plasma density to decrease significantly.

The spatial distributions for 55 and 65 A, at which a sudden drop in I_{sat} was observed in Fig. 5.14, exhibit peaks at both edges of their plateau region. The peaks were from the plasma sheath formed around the inner electrode which suggests high capacitive coupling between the plasma and the antenna resulting in low I_{sat} measurements.

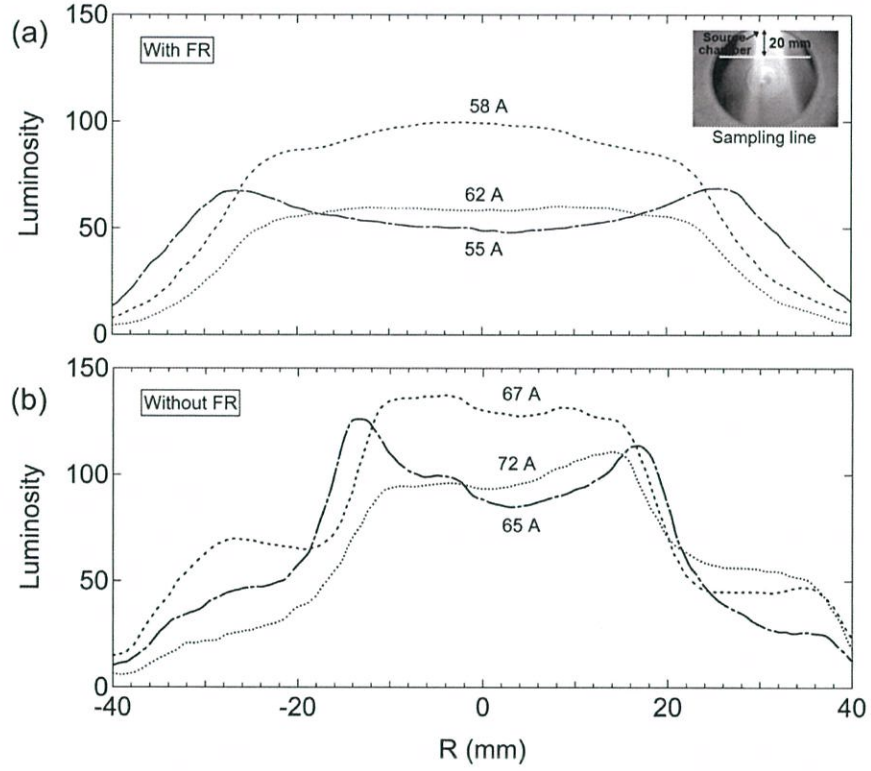

Fig. 5.15 Luminosity spatial distribution in the cases (a) with and (b) without a flux return (FR) at various I_B.

Finally, plasma coupling to the microwave power is examined through the detected 4.9 GHz wave in various I_B as shown in Fig. 5.16. Plasma image luminosity plotted as a function of I_B is overlaid in Fig. 5.16, which agrees with the I_{sat} data in Fig. 5.14a. It can be observed

that high microwave intensities correspond to high luminosities at around 57 and 66 A in with-FR and without-FR cases, respectively. High second harmonic wave intensity at 4.9 GHz indicates strong coupling between the fundamental 2.45 GHz wave and the plasma.

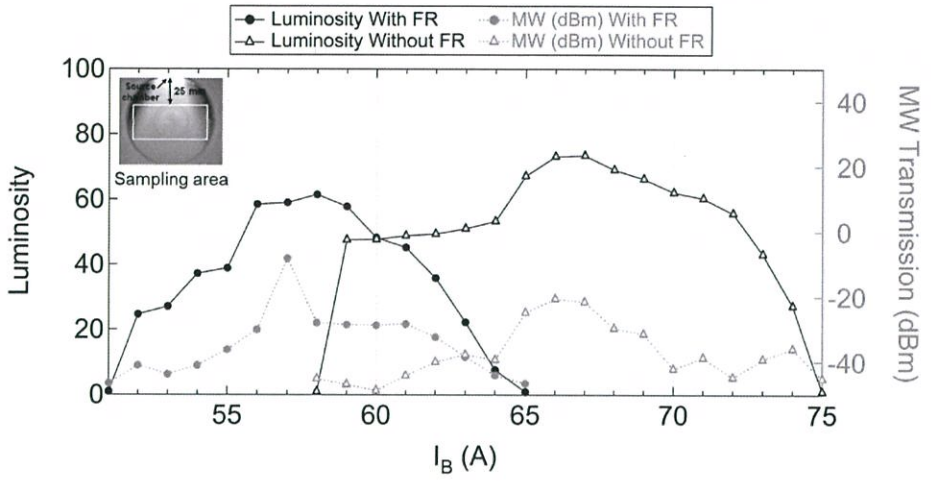

Fig. 5.16 Plasma luminosity and microwave power level at 4.9 GHz as functions of I_B for the cases with and without flux return (FR).

5.4 Discussion

The dependence of ion saturation current I_{sat} and position of the ECR zone z_{res} on magnet current I_B are shown in Fig. 5.17a and b, respectively. Recall that z_{res} is defined as the distance from the base of the antenna flange at which B is 87.5 mT (ECR field) along the chamber axis. As seen in Fig. 5.17a, the carbon coaxial and spiral antennas produced highest I_{sat} at 67 and 89 A, correspondingly. Based on Fig. 5.17b, for the coaxial antenna, at 67 A, z_{res} occurred at 22 mm where the middle of the inner electrode was located. For the spiral antenna, at 89 A, z_{res} occurred at about 60 mm where the spiral plane was located. Since the inner electrode and the spiral plane are where the excited electric fields of the antennas are concentrated, high power absorption in the resonance zone at such locations results in high degree of ionization. Therefore, high plasma density can be obtained when the position of the ECR zone is near the main radiating part.

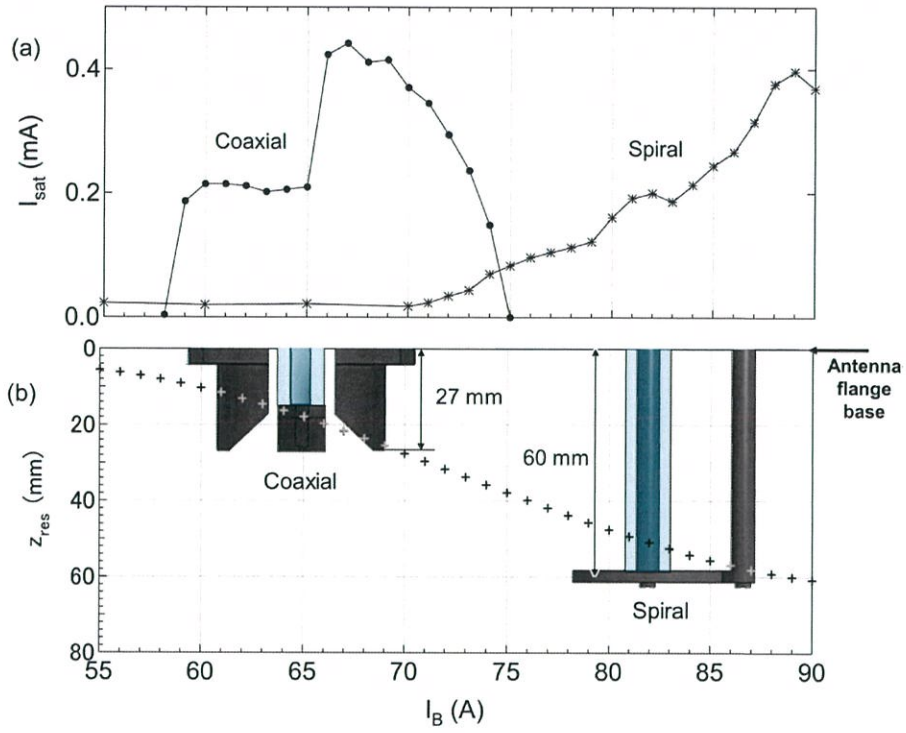

Fig. 5.17 (a) Ion saturation current I_{sat} and (b) distance z_{res} at which the ECR field is created along the chamber axis measured from the base of the antenna flange plotted as functions of I_B.

To closely examine the behavior of plasmas generated using the coaxial antenna, the corresponding plasma formations at different I_B ranges are illustrated in Fig. 5.18. When I_B was increased above 65 A, the position of the ECR zone z_{res} was in the conical part of the outer electrode where the inner electrode was located. This produced high-density plasma discharge, as illustrated in Fig. 5.18a. As I_B was increased above 67 A, I_{sat} values in

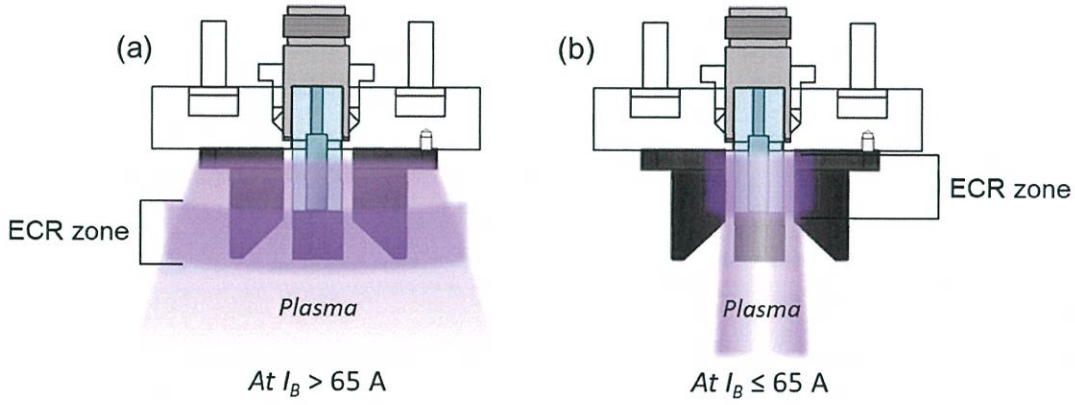

Fig. 5.18 Plasma formations near the coaxial antenna at (a) I_B > 65 A and (b) I_B ≤ 65 A.

Fig. 5.17a gradually decreased. It is because the plasma became more diffuse as z_{res} moved closer to the larger inner edge of the outer electrode.

On the other hand, decreasing I_B to 65 A resulted in a sudden drop in I_{sat}. It occurred when the ECR zone was formed within the cylindrical part of the outer electrode, as shown in Fig. 5.18b. This cylindrical area was insulated that it hindered the plasma discharge to expand out of the antenna, hence, giving low I_{sat} measurements in the probe region. As observed in the bottom-view photos in Fig. 5.4b, plasmas produced by the coaxial antenna at 65 A and below tended to concentrate behind the inner electrode, whereas, above 65 A, plasmas tended to form in front of the inner electrode.

In Fig. 5.19, the dependence of z_{res} on current I_B in the case without flux return is superimposed on that of with flux return. Both cases exhibited some similarities and differences in plasma formation and density relative to the position of the resonance zone. Firstly, in both cases, z_{res} was in the conical region of the outer electrode at I_B values corresponding to high density measurements in Fig. 5.14a. Secondly, both cases had their peak plasma density when I_B was sufficient to form resonance zone in the middle of the inner electrode. Thirdly, increasing I_B further caused z_{res} to move closer to the wide edge

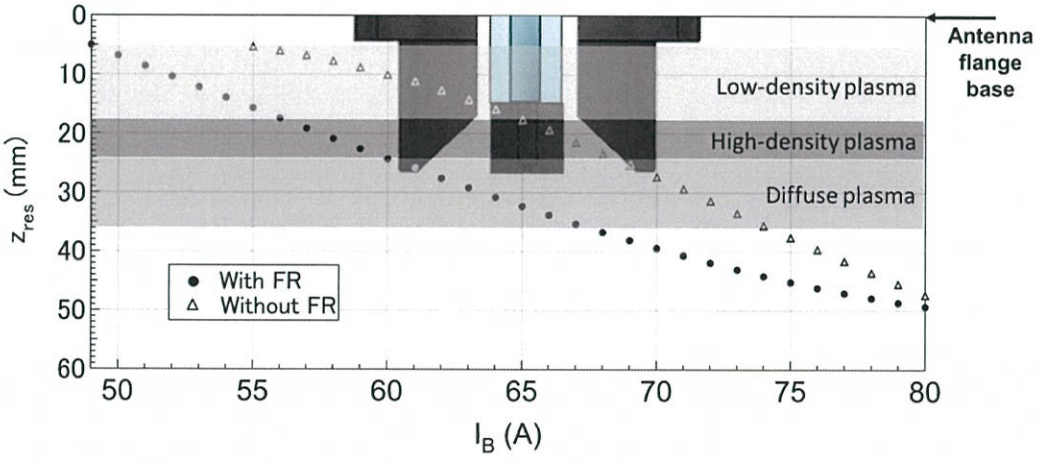

Fig. 5.19 ECR zone position z_{res} as a function of I_B in the cases with and without flux return (FR). Corresponding property of plasmas produced at different z_{res} is also indicated.

of the conical region which produced diffuse plasma, thus, lower I_{sat} values. Fourthly, as in the case without flux return (FR), in the presence of FR, low-density mode began when z_{res} moved to the cylindrical region of the outer electrode. Lastly, in the case with flux return, the plasma discharge was extinguished when z_{res} moved 5 mm away from the edge of the antenna. It is different from the case without flux return in which plasma extinction occurred when z_{res} was about 11 mm from the antenna. This discrepancy may have been due to the difference in shape and size of their resonance zones.

5.5 Conclusion

Compact pure carbon antennas demonstrated good microwave power coupling to ECR plasmas. Better power absorption and plasma homogeneity were observed with the coaxial antenna. Plasma density and homogeneity significantly depends on the position of the resonance zone relative to the antenna geometry. The magnetic flux return can be used to make the plasma properties more suitable for film deposition.

Chapter 6

Carbon Film Deposition by ECR Sputtering Method

6.1 Introduction

Carbon thin films are of great interest in wide range of industrial and technical applications due to their high electrical resistivity, high wear resistance, chemical inertness and wide spectral transparency.[53,54] In the production process of carbon thin film materials, systems are often operated with introduction of small amount of hydrocarbon gases.[55-57] The addition of hydrogen to CH_4 plasma helps in the stabilization of film growth through preferential etching of non-diamond carbon structures formed in the film.[58] This allows successful incorporation of methyl radical CH_3 into crystalline lattice.[59] Flux of hydrocarbon molecule suitable for diamond and diamond-like film formation can be produced by physical or chemical sputtering of graphite by hydrogen ion/neutral bombardment.[60] The sputtering process can be the source of hydrocarbon radicals by controlling the chemical reaction at the carbon surface, from which the produced radical species are directed toward the deposition target. Compared to DC and RF sputtering, higher sputtering yield of graphite can be achieved with high-density magnetized plasmas, such as electron cyclotron resonance (ECR) plasmas.[61] The ECR

plasma system can provide controllability of the molecular species depending upon the plasma parameters and the radical source surface potential. Furthermore, in ECR condition, low-potential and high-density plasmas can be produced at low working pressure. Low pressure reduces the amount of ion collisions in the sheaths at the substrate region which is needed for anistropic etching. In addition, low plasma potential of ECR discharges decreases ion impact energy on the substrate and on wall surfaces, which reduces substrate damage and contamination.[12,25] For these reasons, a system that produces ECR plasma with an internal antenna coupled to a graphite sputtering target in DC magnetic field was designed and tested in this study. This chapter reports the performance of the device in hydrocarbon emission and carbon film deposition.

6.2 Principle of Carbon Sputtering by Hydrogen Plasma

In the case of physical sputtering, an incident ion has to transfer enough kinetic energy to a surface atom or molecule to overcome its surface binding energy. In contrast, chemical sputtering requires much lower threshold energy for surface erosion. Chemical sputtering is different from chemical erosion in a way that the latter is a thermally activated process which requires a minimum substrate temperature.[62]

The basic mechanism of sputtering of carbon surfaces by hydrogen plasma was studied by Salonen et. al., and is illustrated in Fig. 6.1.[63] The small dark spheres represent hydrogen ions, while the large light spheres represent carbon atoms. Diagram (a) shows the typical hydrogenated amorphous carbon (a-C:H) arrangement at the surface. In (b), the H ion slightly interacts with the outer carbon atom, and (c) enters the space between two carbon atoms. As illustrated in (d), after the H ion collides with the inner carbon atom, the ion is reflected. Eventually, (e) the carbon atoms are forced apart by the H ion between them. The carbon atom then (f) leaves the target with H atoms bonded to it.

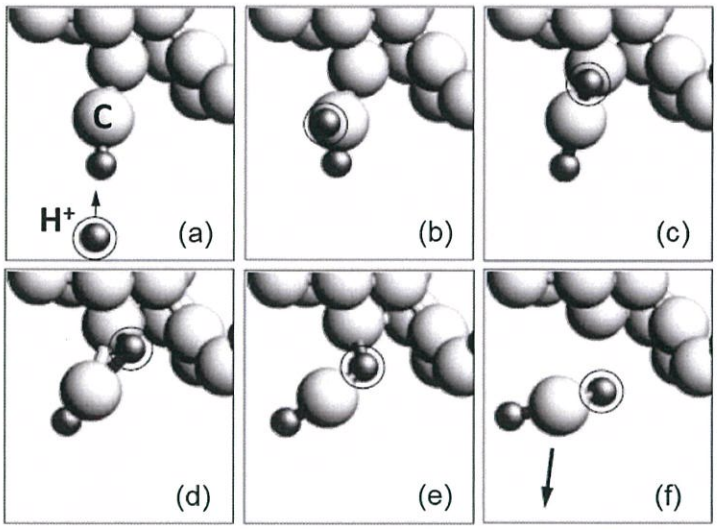

Fig. 6.1 Mechanism of carbon sputtering by hydrogen plasma (after Ref. 63).

6.3 Methods and Materials

6.3.1 Deposition Setup

The plasma system used in ECR chemical vapor deposition (ECR CVD) is shown in full in Fig. 3.2 and described in detail in chapter 3. The main part of the system used for deposition is shown in Fig. 6.2a. The hydrogen gas was supplied through the ring-shaped gas injection unit which was located above the substrate holder, as shown in Fig. 6.2a.

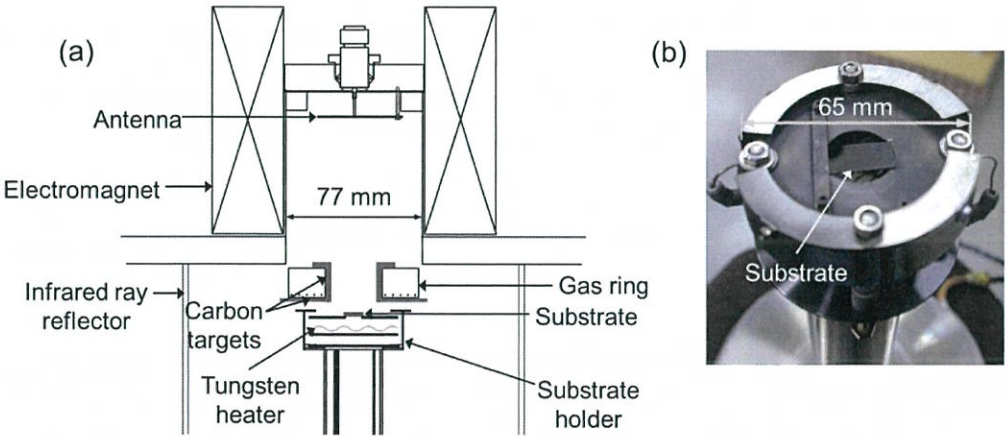

Fig. 6.2 (a) Experimental setup of ECR chemical vapor deposition (ECR CVD) of carbon thin film. (b) Actual image of the substrate holder.

The substrate holder, shown Fig. 6.2b, has an electrically floating stage which was connected to a DC source to apply bias voltage on the substrate. A thermocouple wire directed close to the substrate was used in measuring the substrate temperature.

Generated hydrogen plasma from the source chamber diffused into the process chamber along the magnetic field generated by the electromagnet. As the hydrogen plasma interacted with the solid carbon targets on the gas ring, hydrocarbon molecules were produced by ECR sputtering. The mechanism of film formation starts from touch down of hydrocarbon molecules to the deposition substrate, followed by successive hydrogen extraction through substrate heating, leaving the carbon atoms on the substrate surface, as illustrated in Fig. 6.3.

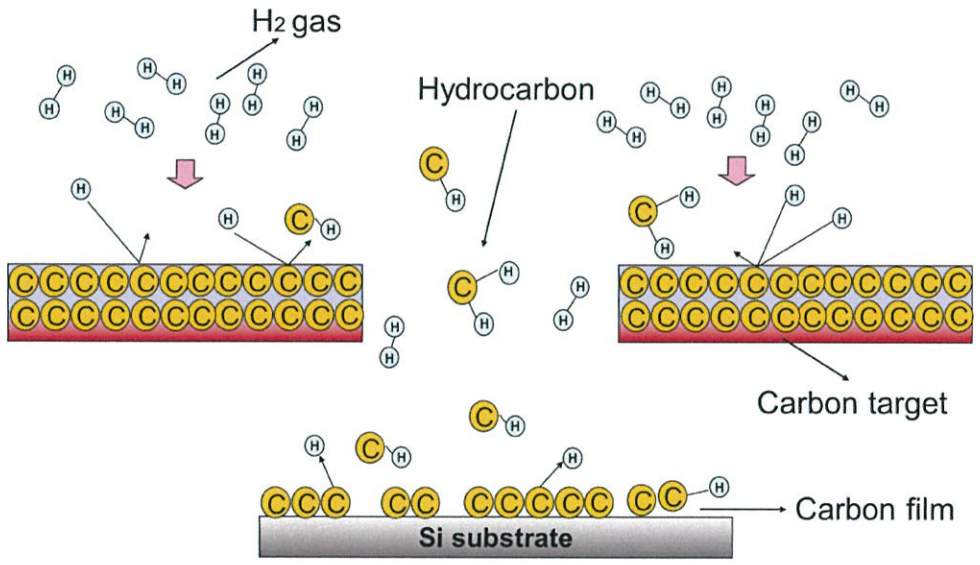

Fig. 6.3 Carbon film formation of hydrocarbon molecules produced by ECR sputtering.

6.3.2 Carbon Sheet and Cylinder Target

To reduce contamination from the tungsten heater at the back of the sample stage, a 30 x 30 x 1 mm carbon sheet was placed underneath the Si substrate as shown in Fig. 6.4a. In addition, a 67-mm-diameter, 90-mm-high, 6-mm-thick carbon cylinder was inserted into the source chamber, as illustrated in Fig. 6.4b, to cover its walls and eliminate metal

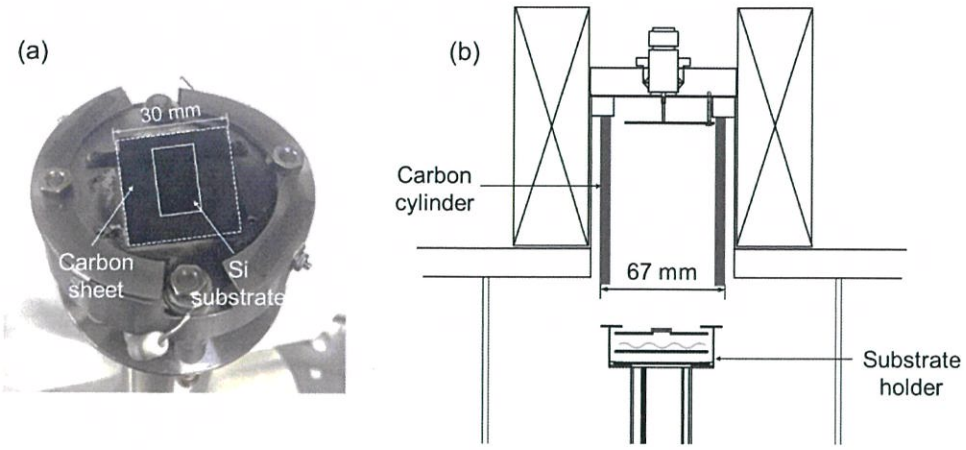

Fig. 6.4 (a) A carbon sheet placed underneath the Si substrate. (b) A carbon cylinder inserted into the source chamber.

impurities due to surface sputtering. The gas ring was removed from the chamber when the cylinder was installed. It served as the sputtering target in replace of those attached to the gas ring in the latter part of this chapter.

6.3.3 Film Preparation

Carbon thin films were deposited on Si (111) of dimension 20 x 10 x 1 mm at 100 W microwave power, deposition time ranging from 1 to 5 hours, and working pressure ranging from 1 to 10 Pa. The Si substrate was cleaned in an ultrasonic bath for 30 minutes and air dried before placing it on the substrate holder. The temperature of the tungsten wire wound at the back of the sample stage was raised by slowly applying current up to 19 A. The substrate is then heated to about 650 °C by the infrared radiation from the high-temperature tungsten wire. The carbon disk target and the substrate stage were biased at -400 V and 70 V with respect to the chamber wall, correspondingly.

6.3.4 Optical Emission Spectroscopy (OES)

Optical emission spectroscopy (OES) was carried out for the characterization of the excited hydrocarbon radicals and atomic hydrogen species present in the plasma. When

atoms and ions gain energy by absorption of radiation or by collision, electrons bounded to their nucleus are excited from a lower to a higher energy state. Electrons are less stable in the excited state, and tend to spontaneously de-excite back to the lower energy state. During this transition, the electrons release the difference in energy between the two states as photons. The energy of an emitted photon is given by,

$$E_{photon} = h\nu \tag{6.1}$$

where h is the Planck's constant and ν is its frequency. Each element or compound emits a characteristic set of discrete frequencies or wavelengths according to its electronic structure. By detecting and measuring these wavelengths, using an optical emission spectrometer, the elemental or chemical composition of a given sample can be identified.

An optical fiber attached to an *Ocean Optics* USB4000 spectrometer with 0.2 nm spectral resolution was utilized in this study. The fiber sensor head was mounted perpendicularly to the front or bottom viewport, as shown in Fig. 3.5b, to collect light emission from the plasma between 342–1038 nm.

6.3.5 Mass Spectroscopy

To obtain information on the present radicals both in excited and ground states, mass spectroscopy was employed. A basic mass spectrometer is consisted of an ionizer, an analyzer and a detector. The analyzer separates the ions according to their mass-to-charge ratio (m_i/q). Based on Newton's second law of motion and Lorentz force law:

$$\left(\frac{m_i}{q}\right)\boldsymbol{a} = \boldsymbol{E} + \boldsymbol{v} \times \boldsymbol{B} \tag{6.2}$$

where q is the ion charge and $\boldsymbol{a}$ is the acceleration, particles with the same m_i/q ratio behave in the same way in the presence of electromagnetic fields. Typically, the m_i/q ratio is expressed as the dimensionless m/z ratio, with m as the mass number and z as the charge number ($z = q/e$).

There are several types of mass analyzers, and one of them is the quadrupole mass analyzer (QMA). The basic principle of QMA operation is shown schematically in Fig. 6.5. It has four parallel metal rods that "filter" the ions based on the mass-to-charge dependency of the ion trajectories on RF and DC fields. Each opposing rods are connected, and an RF voltage with a DC offset voltage is applied between each pair of rods. The magnitude and frequency of the RF determine the m/z ratio of the ions that can pass through the quadrupole mass-filter without striking the rods. The RF/DC ratio determines the filter selectivity. Ions that successfully pass through the filter are focused towards the detector and the resulting analog current is measured by a sensitive electrometer.[64] The derivation of the working equations for quadrupole mass analyzer is beyond the scope of this discussion. However, it is based upon a second-order differential equation known as the *Mathieu equation*.[65]

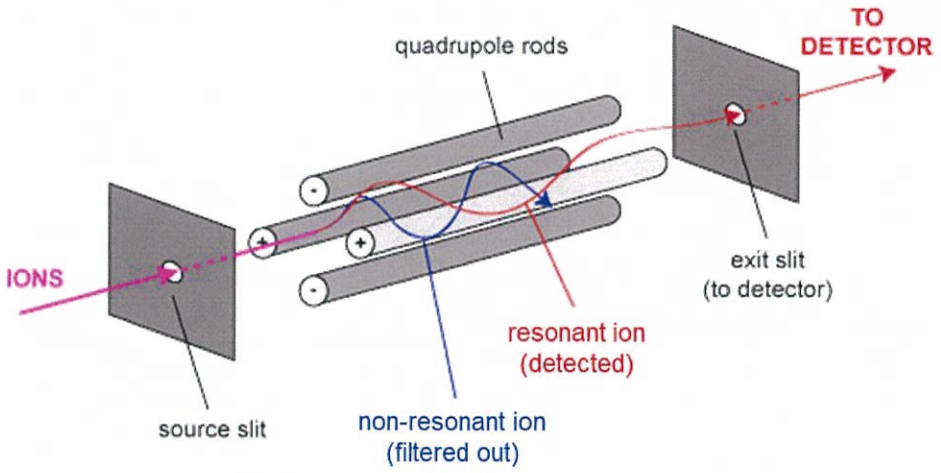

Fig. 6.5 Schematic diagram of a quadrupole mass analyzer (after Ref. 66)

In this study, an SRS 200 *Residual Gas Analyzer* was connected to a 70 L/s TMP coupled to a rotary pump. The gas analyzer utilizes a QMA, with mass range of 1 to 200 amu, which identifies different molecules present in a residual environment. To monitor the gas species near the surface of the carbon sputtering target, the gas analyzer system was attached to a probe inserted into the process chamber, as shown in Fig. 6.6a. The

stainless steel 18-mm-diameter probe with 0.5-mm-diameter aperture faces the carbon disk target along its vertical axis, as illustrated in Fig. 6.6b. The spectrometer ionizer located at the end of the tube system is about 22 mm from the aperture line-of-sight.

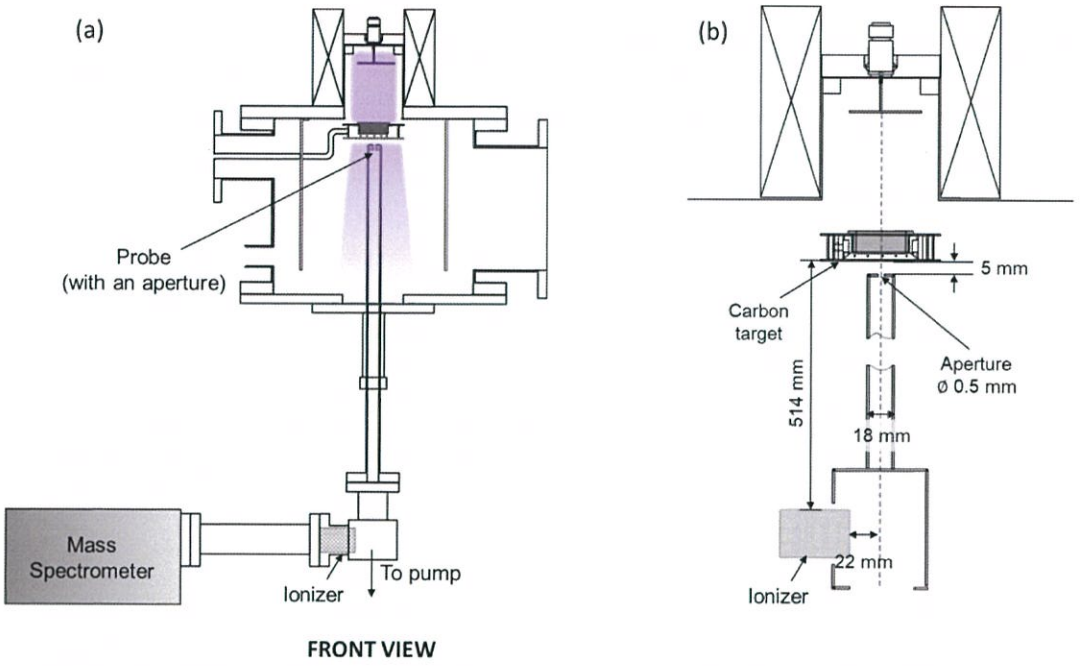

Fig. 6.6 (a) Schematic diagram of the mass spectroscopy setup and (b) diagram showing the probe coupled to the mass spectrometer and facing the carbon target.

6.3.6 X-Ray Diffraction (XRD) Analysis

The samples were analyzed through X-ray diffraction (XRD) to determine the crystal structure and chemical composition of the deposited films. XRD analysis is based on the interaction of incident X-rays with the atoms in the crystal lattice of a sample.

As illustrated in Fig. 6.7, *Bragg diffraction* occurs when incident monochromatic rays are scattered by the atoms of a crystalline structure and produces constructive interference. *Bragg's law* gives the condition on the diffraction angle θ for constructive interference to be at its strongest:[67]

$$2dsin\theta = n\lambda \tag{6.3}$$

where d is the lattice spacing and λ is the wavelength of the incident rays. When scattered

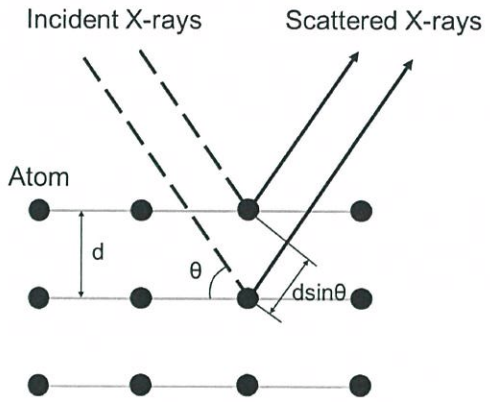

Fig. 6.7 Schematic diagram of Bragg diffraction where incident X-rays are scattered in mirror-like reflection by the atoms of a crystalline structure and undergo constructive interference.

waves undergo constructive interference, they remain in phase since their path difference ($2d\sin\theta$) is equal to a positive integer (n) multiple of the wavelength. As the effect of scattering in successive lattice planes accumulates, the effect of constructive interference intensifies. These diffracted X-rays are then detected, processed and counted. A diffraction pattern is obtained by measuring the intensity of diffracted rays while scanning through 2θ range. Conversion of the diffraction peaks to d allows identification of the chemical structure and composition since each material has a unique set of d.

In this study, a point focus PANalytical X'Pert PRO Materials Research Diffractometer was used to analyze the samples. Since the bulk of the sample is mostly consisted of Si substrate, the Si diffraction peaks significantly outsize the peaks from the thin film. Hence, samples were examined at an in-plane orientation to make the incident X-rays come in grazing angle (0.1^{o}) and primarily pass through the film region.

6.3.7 Scanning Electron Microscopy (SEM) and Energy Dispersive X-Ray Spectroscopy (EDS)

Samples were examined through a JEOL JSM-7001FD field emission scanning electron microscope to get information on the morphology and elemental composition of the deposited films. As the incident beam of accelerated electrons in an electron microscope

hit the sample, the electrons lose energy by repeated random scattering and absorption within it. The interaction between the electrons and the sample produces secondary electrons, backscattered electrons, diffracted backscattered electrons, photons, visible light, and heat. Secondary electrons are commonly used for showing the morphology and topography of samples in scanning electron microscopy (SEM), while emitted photons or characteristic X-rays are used for elemental analysis in energy dispersive X-ray spectroscopy (EDS).

6.4 Results and Discussion

6.4.1 Using Different Antenna Flange Configuration

Emission intensities of the downstream plasma in the process chamber were detected through the front viewport to observe the excited species in the plasma. The magnet current and microwave power were set at 80 A and 100 W, respectively. The typical optical emission spectrum obtained from the plasmas produced by the ECR source is shown in Fig. 6.8. The first three lines of the Balmer series for hydrogen at H_α 656, H_β 486, and H_γ 434 nm were observed. Strong Balmer line intensity occurs when many of the

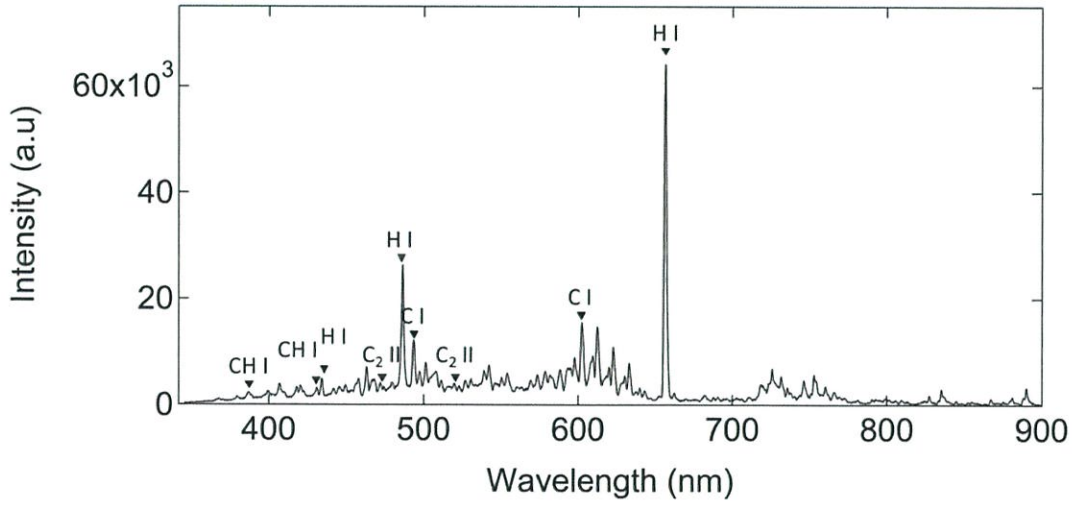

Fig. 6.8 Typical optical emission spectrum of plasmas produced by the ECR device.

hydrogen atoms have electrons that are in the first excited state. Excited neutral carbon atoms (C I) at 493 at 602 nm were detected as well. Singly ionized diatomic carbon (C_2 II) lines in the Swan band system were identified at 516 and 473 nm, while, CH radicals were found at 387 and 431 nm bands.

Shown in Fig. 6.9 is the superposition of mass spectra before and during ECR microwave plasma operation at 1 Pa H_2 pressure in far-antenna configuration (see Fig. 4.3). The mass spectra revealed the increase in the hydrocarbon (CH_x, C_2H_x and C_3H_x) radicals during the plasma discharge which confirms the sputtering of the carbon target by the ECR hydrogen plasma. The other peaks are caused by fragments of these species. Residual traces of N_2^+, O_2^+ and H_2O^+ were also detected in the background. The presence of air components in the spectra does not necessarily mean that the system was leaking. Instead, the turbomolecular pump (TMP) may have simply reached its compression limit. Ideally, the compression ratio of the TMP is in the 10^{-8} range.

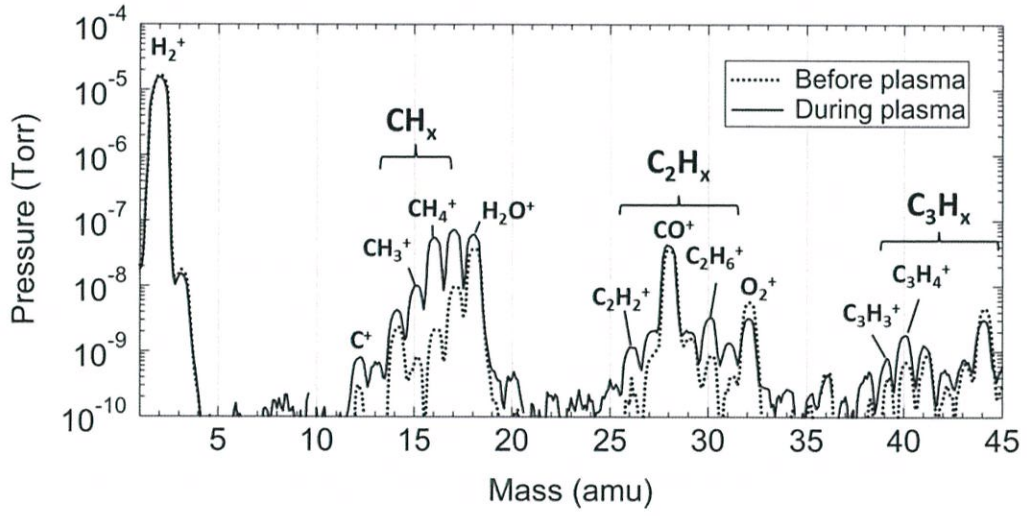

Fig. 6.9 . Mass spectra before and during ECR plasma excitation in far configuration.

The effect of antenna configuration on hydrocarbon production can be observed in the mass spectra shown in Fig. 6.10. Recall that each configuration varies in the distance between the antenna and the graphite sputtering target, as illustrated in Fig. 4.3. More

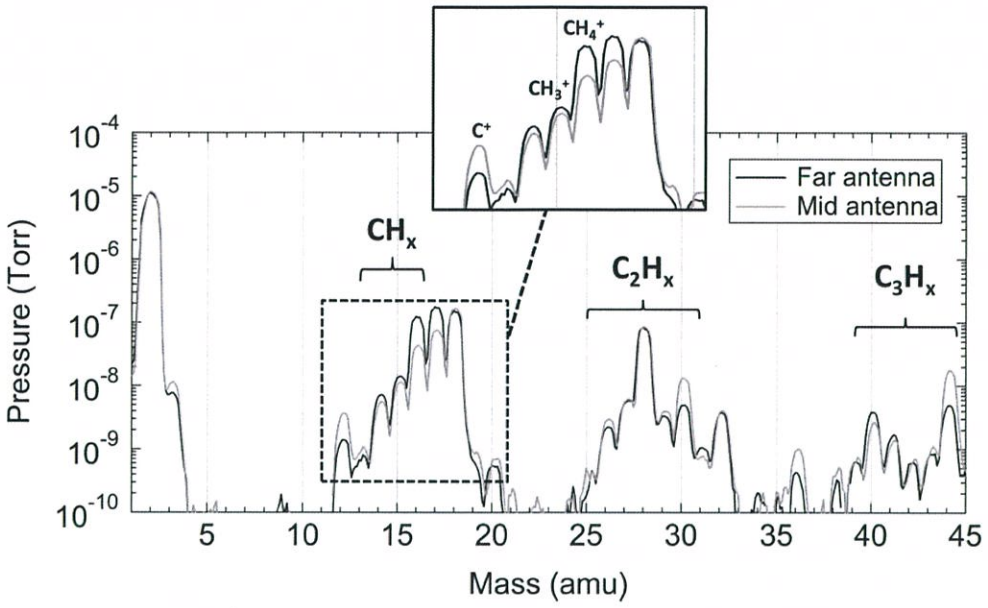

Fig. 6.10 Mass spectra of plasma excited in far and mid configurations.

carbon atoms were produced when the antenna was positioned closer to the graphite target in mid configuration. On the other hand, more CH_x radicals were generated when the antenna was farther from the sputtering target in far configuration. To examine these results, sputtering of the carbon target by hydrogen plasma in mid and far configurations are illustrated in Fig. 6.11a and b, respectively. More carbon species were observed in plasmas excited in mid configuration due to the proximity of the antenna to the carbon

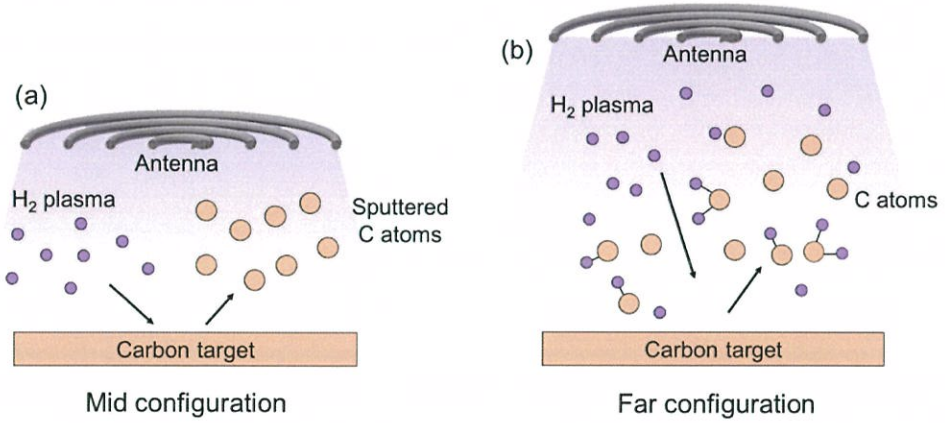

Fig. 6.11 Schematic diagram of sputtering of the carbon target by hydrogen plasma in (a) mid- and (b) far-antenna configurations.

target. It increased the incident ion energy, thus, increasing the bond breaking probability by physical sputtering. As for the far configuration, the plasma was excited farther from the graphite target giving more room for carbon radicals to react with hydrogen ions, thus, enhancing the formation of CH_x radicals by chemical sputtering.

Shown in Fig. 6.12 are SEM images of films deposited using the 4-turn Ni spiral antenna in different flange configurations. The exposure time and working pressure were set at 3 h and 10 Pa, respectively. The carbon sheet and cylinder were not yet placed during this time. Larger and denser grains were found in the film formed in far configuration, possibly due to the high production of CH_x radicals which are necessary for film growth. On the other hand, fewer grains were found in the near-configuration-formed-film. In near configuration, the deposition substrate is close to the plasma locally excited by the antenna. High ion flux to the substrate could have hindered the stable formation of film due to excessive sputtering.

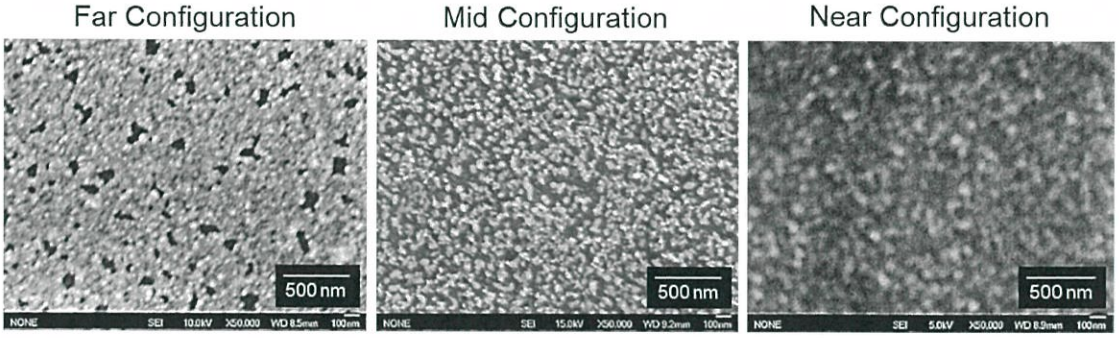

Fig. 6.12 SEM images of films produced in different flange configurations.

In far-antenna configuration, plasmas produced at various H_2 working pressures exhibit different grain sizes and densities, as seen in the SEM images in Fig. 6.13. Highest film density was obtained at 5 Pa.

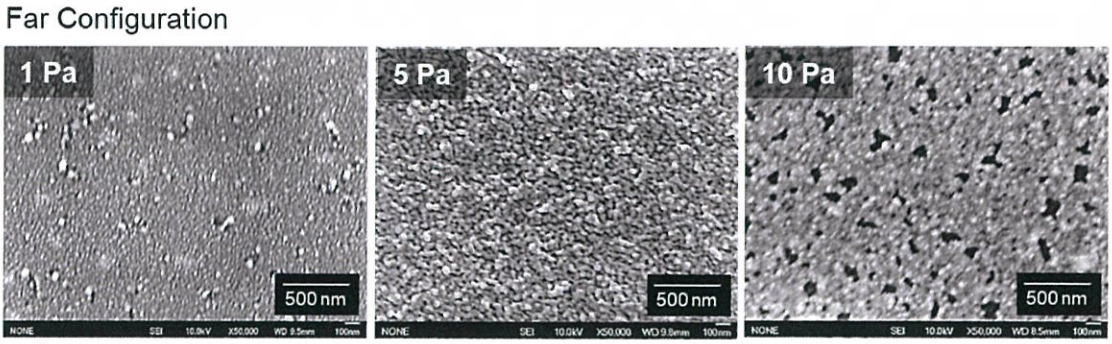

Fig. 6.13 SEM images of films produced in far configuration at different working pressures.

Crystalline structure of the films prepared in far, mid and near configurations have been confirmed in the XRD spectra shown in Fig. 6.14. Tungsten Silicide (WSi_2) crystals were found in the films. It is known that WSi_2 forms when the substrate is heated to temperatures of 600 °C and higher.[68] Such contamination from the tungsten heater made it difficult to detect carbon structures.

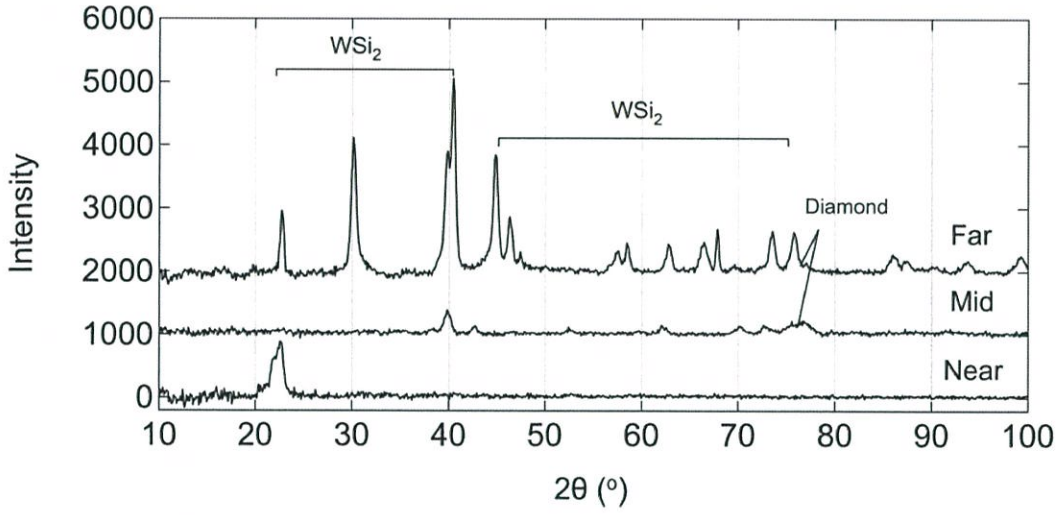

Fig. 6.14 Vertically shifted XRD spectra of films produced in different flange configurations.

To further investigate the factors affecting the CH production, as shown in Fig. 6.15, partial pressures of carbon and hydrocarbon radicals from the mass spectra were plotted as functions of the bias voltage applied to the carbon sputtering target. The plasma was excited in far-antenna configuration. The increasing trend of C^+ until saturation can be

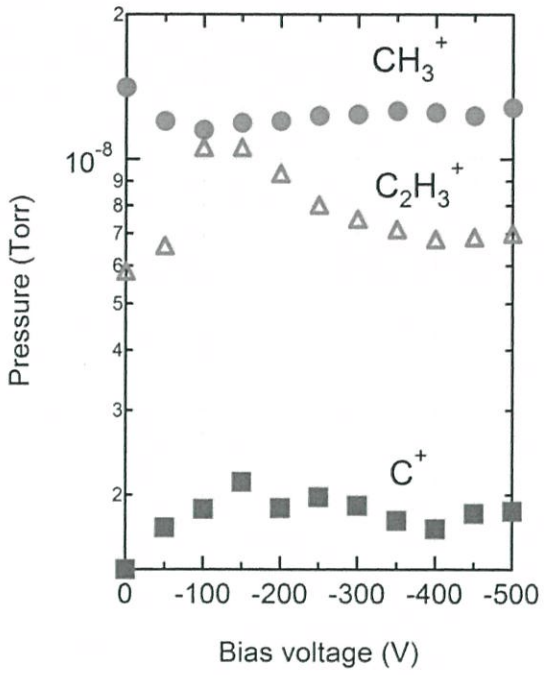

Fig. 6.15 Partial pressures of C and CH radicals as functions of the bias voltage applied to the carbon target.

observed as the negative bias voltage was raised. At around -100 V, CH_3^+ and $C_2H_3^+$ were formed together with almost equal amounts. As the sputtering target bias was increased, formation of $C_2H_3^+$ decreases.

Increased concentration of $C_2H_3^+$ below -100 V can be attributed to the high hydrogen adsorption on the surface of the target enhancing chemical sputtering. During that phase, the carbon target is exposed to more excited atomic hydrogen producing the radicals C_nH_m represented by $C_2H_3^+$. These molecules are known to be weakly bound surface groups that are typically eroded by chemical sputtering.[69] Higher bias voltage corresponds to increased energy of bombarding hydrogen, and the sputtering yield should be higher at higher bias, provided the same amount of hydrogen atoms are adsorbed. The decrease in $C_2H_3^+$ partial pressure as the bias voltage was raised can be caused by the depletion of hydrogen atoms near the surface of the carbon target leading to the reduction of chemical sputtering.

6.4.2 Using a Carbon Sheet Target

Due to the observed tungsten contamination in the XRD spectra of the deposited films, a carbon sheet, described in section 6.3.2, was placed underneath the Si substrate to cover it from the tungsten heater. Surface morphology of films deposited at different working pressures, without and with the carbon sheet can be observed in the SEM images shown in Fig. 6.16a and b, respectively. Without the carbon sheet, tungsten silicide particles with about 50 nm size formed in the deposited films. When the carbon sheet was present, plasmas were generated using the carbon spiral antenna in far configuration. The absence of particles on the SEM images in Fig. 6.16b suggests the prevention of tungsten silicide formation on the film when the carbon sheet was present.

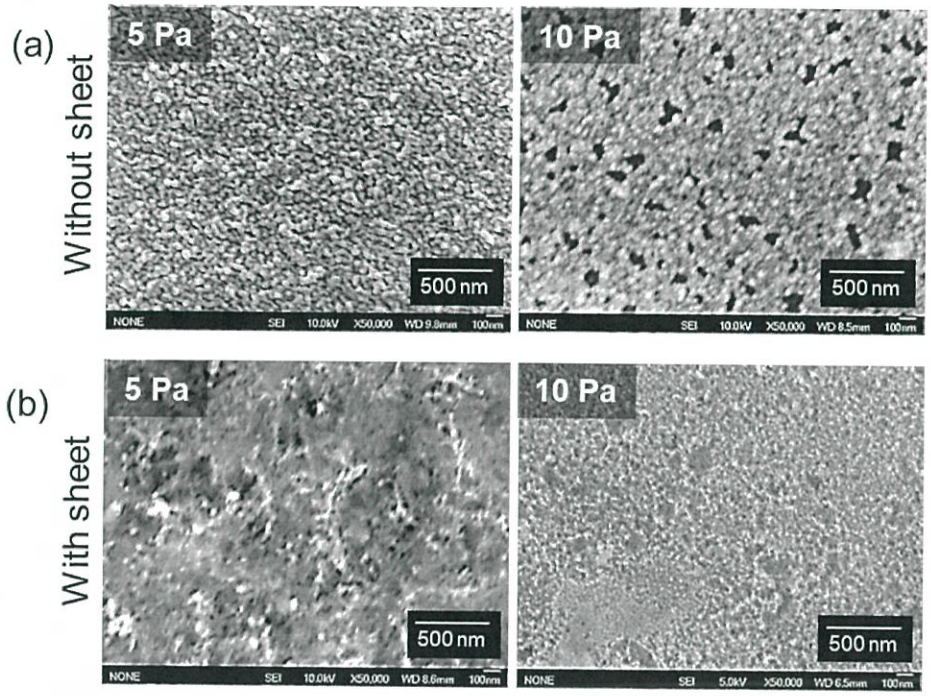

Fig. 6.16 SEM images of films deposited (a) without and (b) with a carbon sheet underneath the Si substrate at various working pressures.

6.4.3 Using Different Carbon Antenna Structures

Carbon and hydrocarbon emissions in plasmas produced with carbon coaxial and spiral antennas (see Fig. 5.1) are discussed in this section. Relative intensities of C_2 (474

nm) and CH (431 nm) bands from the OES data are plotted as functions of H_2 gas pressure in Fig. 6.17a. I_B is set at 70 and 90 A when using coaxial and spiral antennas, respectively, since they correspond to approximately equal I_{sat} values. In both cases, C_2 and CH emission intensities rise in increasing pressure to a peak value at 0.8 Pa due to increasing number ionizing collisions. Coaxial antenna-generated plasma has higher C_2 and CH intensities when the pressure was below 2 Pa. Emission intensities are not necessarily a quantitative measurement of ground state species concentration. Nevertheless, high population of excited C_2 and CH species can be attributed to the enhanced sputtering of carbon by hydrogen plasma. At higher pressures, C_2 and CH

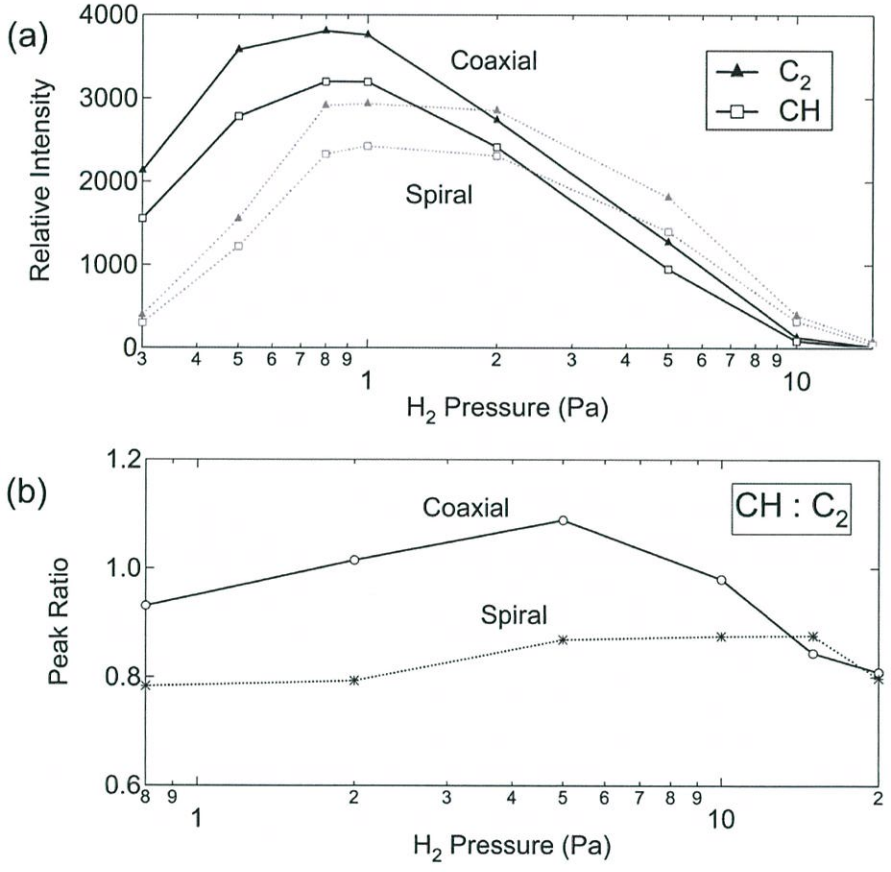

Fig. 6.17 (a) Relative emission intensities of C_2 and CH species, and (b) peak intensity ratio of CH to C_2 plotted as functions of H_2 pressure for plasmas produced using carbon coaxial and spiral antennas.

emission intensities detected from the process chamber decreased due to the shorter mean free path.

An important factor in carbon film deposition is the ratio of CH band to excited C_2 dimer peak. CH:C_2 ratio was found to be correlated to diamond growth rate and quality.[70] Relatively higher CH:C_2 peak ratios were obtained when using the carbon coaxial antenna. The highest ratio was achieved at 5 Pa, until it began to decrease at higher H_2 pressures. A higher H_2 pressure can cause additional reactions such as $C_2+H_2 \rightarrow C_2H + H$,[71] which reduces the C_2 intensities.

Weight densities of films deposited using the coaxial antenna at different working pressures and deposition time are shown in Fig. 6.18a and b, respectively. The carbon

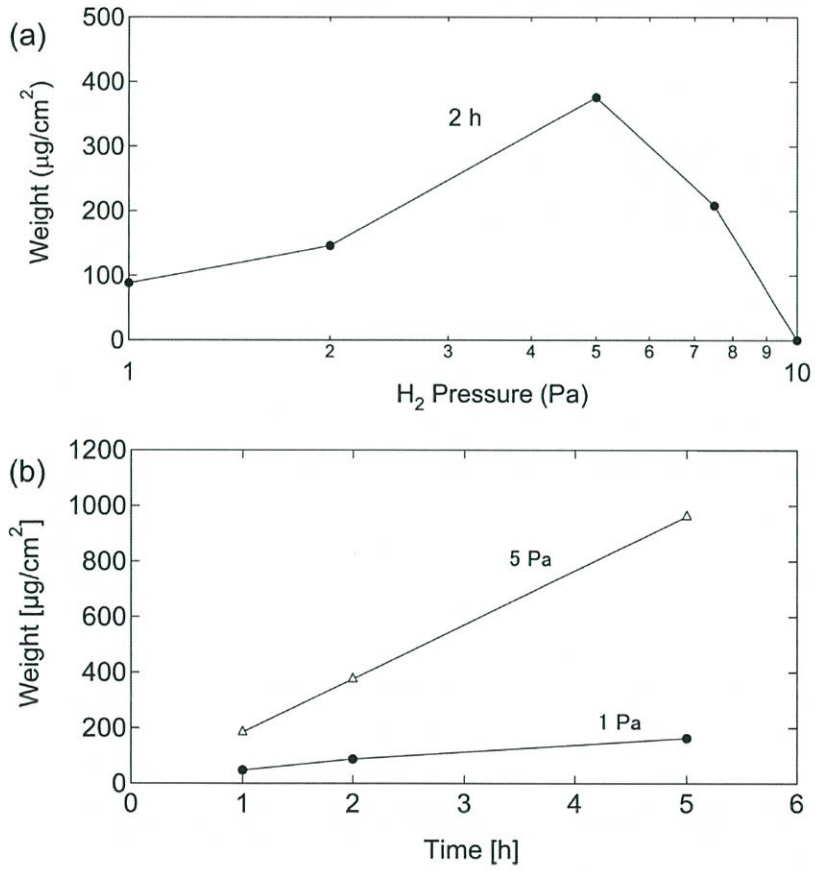

Fig. 6.18 Weight density of films deposited using the carbon coaxial antenna at various (a) H_2 pressures and (b) deposition time.

sheet underneath the substrate was present during the deposition. The magnet current was set at 74 A to reduce the ion flux at the substrate region and lessen the film etching effect of the ions. Based on Fig. 5.8a, the plasma uniformity was not compromised when I_B was set to 74 A. At 2 h deposition time, the highest film density was obtained at 5 Pa working pressure. In addition, the deposition rate at 5 Pa is about three times as much as the rate at 1 Pa working pressure. Sufficiently low I_{sat} value and relatively high CH:C_2 ratio observed at 5 Pa in Fig. 5.10 and Fig. 6.17b, respectively, resulted in the enhanced deposition rate of the film.

Fig. 6.19 shows the SEM images of films produced at different working pressures and deposition time. Clustered-structures observed in the film deposited for 5 h at 1 Pa (left) became larger and denser when the pressure was increased to 5 Pa (center). When the deposition time was reduced to 2 h (right), nanoparticles of about 40 nm in diameter were found on the film surface. These particles were not present at 5 h of deposition possibly due to erosion of the film surface by excited hydrogen atoms during the prolonged exposure.

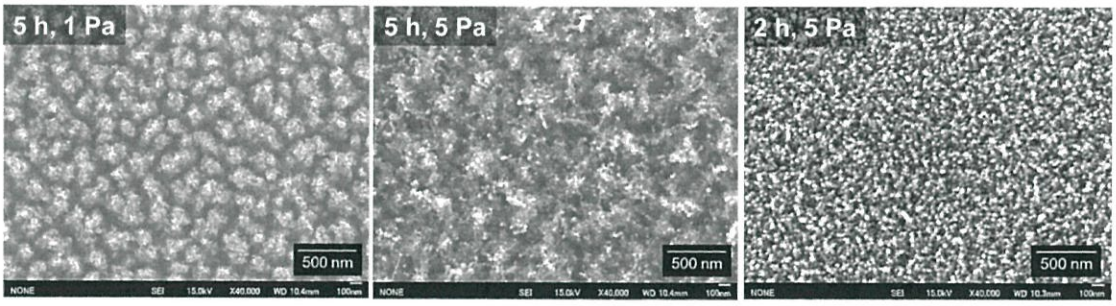

Fig. 6.19 SEM images of films deposited using the carbon coaxial antenna at different gas pressures and exposure time.

The elemental composition of the deposited films based on EDS is shown Table 6.1. Relatively high atomic percentage of carbon atoms were detected on the surface of the films deposited at 1 and 5 Pa. Recall that the films deposited without the carbon sheet in section 6.4.1 abundantly contain tungsten (W) based on their XRD data. This time, the

Table 6.1 Elemental composition of films deposited at different working pressures.

Element	Atomic % for 1 Pa	Atomic % for 5 Pa
C	67.53	61.97
O	2.08	3.84
Si	28.66	30.92
Cr	0.32	0.38
Fe	0.98	1.10
W	0.43	1.69

carbon sheet has effectively reduced tungsten contamination from the heater, resulting in less than 2% of tungsten atomic percentage.

During the operation, the ECR reactor maintained a stable plasma for more than 5 h. During this time, the reflected power increased from about 0 to 1%, which is presumably due to an increase in the antenna temperature. A 2% decrease in the weight of the inner graphite electrode was measured after the 5 h operation. A thin film deposited on the inner surface of the conical part of the outer electrode was also observed. The MW power feedthrough showed no degradation throughout the experiment. The screw connecting the inner electrode to the MW power feedthrough required replacement after four or five 5 h operations.

6.4.4 Using a Magnetic Flux Return

Based on the EDS data in Table 6.1, traces of chromium (Cr) and iron (Fe) were found on the surface of the deposited films. Such impurities are possibly from the walls of the source chamber and the gas injection unit. Hence, the gas unit was removed from the chamber and a carbon cylinder was used to fully cover the inside wall of the source chamber. Peak intensity of excited H atoms (H_β 486 nm) based on OES data is plotted as a function of H_2 pressure in Fig. 6.20a. I_B is set at 58 A and 70 A in the cases with and

without flux return, respectively, since they have nearly equal luminosity as seen in Fig. 5.16. In both cases, H emission intensities rise in increasing pressure to a peak value at 2 Pa. It was known that atomic hydrogen species in ECR plasma play an important role in preferential etching of amorphous carbon films.[12] In Fig. 6.20b, the dependence of CH:C_2 peak intensity ratio on H_2 pressure is displayed. It is evident that CH:C_2 is higher by 3 to 24% in the presence of flux return at pressures above 2 Pa. H intensity and CH:C_2 ratio began to decrease as H_2 pressure was increased above 2 Pa and 5 Pa, respectively, due to the shorter mean free path of the plasma particles at higher pressures.

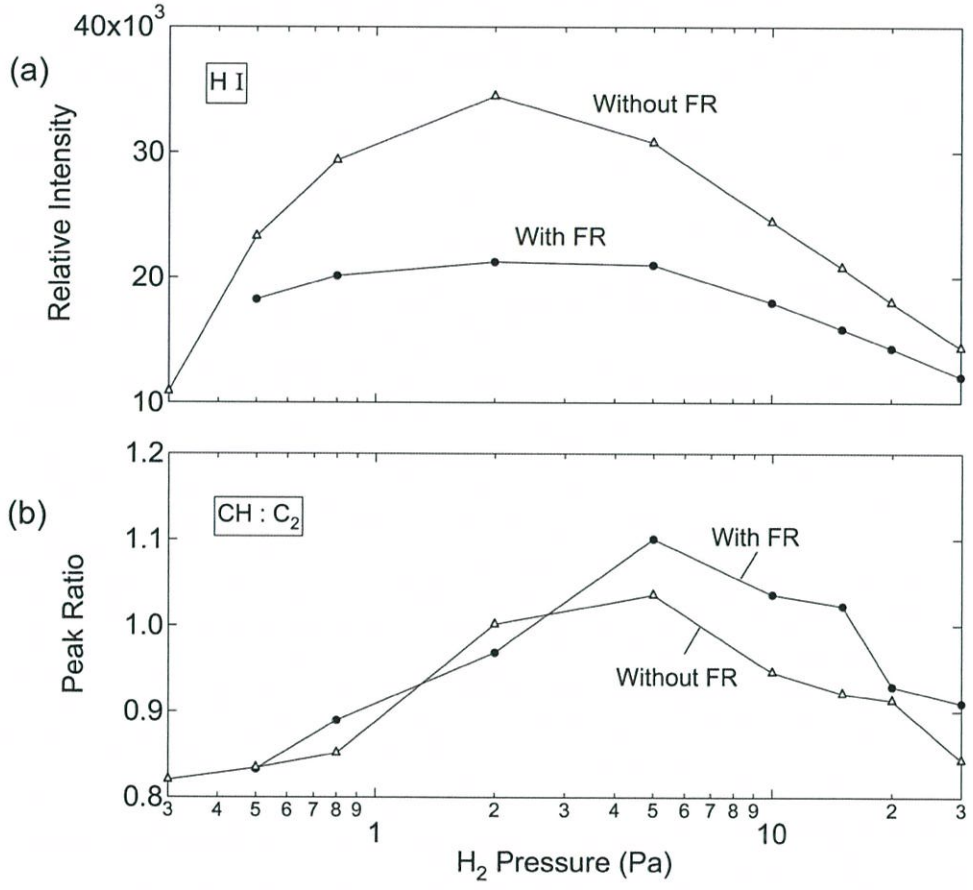

Fig. 6.20 (a) Relative emission intensity of H I (486 nm) species and (b) peak intensity ratio of CH to C_2 plotted as functions of H_2 pressure in the cases with and without flux return (FR).

6.5 Conclusion

The particle flux from the carbon target during plasma operation was monitored with a quadrupole mass analyzer, and the result had clearly indicated the presence of both physical and chemical sputtering. Carbon film was successfully formed on Si substrate by arranging a carbon target in ECR excited hydrogen plasma without supplying any hydrocarbon molecule. The formation rate and grain size distribution of the film are attributed to the dependence of production rate and species composition of hydrocarbon flux on antenna configuration and hydrogen pressure. The ECR source with carbon internal antenna operated stably for more than 5 h without any overheating and can be utilized to maintain a stable plasma for carbon film deposition.

Chapter 7

Conclusion

The electron cyclotron resonance (ECR) plasma source designed and developed in this study to couple microwave power to plasma using an internal antenna successfully generated well-matched discharges (P_r = 0) with high plasma densities (10^{16} m^{-3}) at low gas pressures (10^{-1} Pa) and low input power (100 W). Overall, the ECR plasma system worked well for the purposes of plasma generation and film deposition. Yet, it is strategic to evaluate not only the advantages that the present system provides, but also its disadvantages, to realize further improvements.

7.1 Advantages and Applications

The following points give some of the advantages of the ECR plasma system developed in this study and its possible applications in materials processing.

1. The ECR source does not have to use complex waveguide systems due to the low input power required to sustain a stable discharge.
2. The internal antennas are adaptive to coaxial cable which reduces the system size substantially and provides simple system construction.
3. The accumulation of ejected particles on dielectric windows is avoided by using an internal antenna for microwave coupling. The internal antenna offers easy maintenance of high-density plasma sources used in etching and deposition.

4. The system does not require additional supply of hydrocarbon gases, instead, the graphite target immersed in hydrogen plasma forms hydrocarbon flux suitable for carbon film deposition.
5. The production of excited atomic hydrogen species can be increased, by changing the position of the resonance zone relative to the antenna geometry, to improve the preferential etching of non-diamond carbon structures.
6. The magnetic field configuration (with flux return) of the ECR device enhances plasma uniformity and production of CH and C_2 radicals which are correlated to diamond growth rate and quality.

7.2 Disadvantages and Recommendations

1. The ECR plasma system requires dc magnetic field which makes it more complex than other high-density sources such as inductive coupled plasma (ICP) systems.
2. Strong electrostatic coupling can occur between the antenna and the plasma.
3. Coupling mode transition that affects the absorption of microwave power was observed over 0 to 90 A magnet current range.
4. Contamination from the tungsten heater and wall surfaces were observed. Additional carbon sheet and cylinder targets are needed to reduce impurities.
5. To monitor the ion energy distribution at the substrate region, a faraday cup is recommended to be installed in the device.
6. To further control the hydrocarbon species generated from the graphite target, it is recommended to add heating component to the sputtering target.

References

1. W. B. Ard, M. C. Becker, R. A. Dandl, H. O. Eason, A. C. England, and R. J. Kerr. "Neutron Production from a Steady-State, Hot-Electron, Deuterium Plasma." *Phys. Rev. Lett.* 10 (1963): 87.
2. D. B. Miller and G. W Bethke. "Cyclotron Resonance Thruster Design Techniques." *AIAA J.* 4 (1966): 835.
3. L. Bardos, G. Loncar, I. Stoll, J. Musil, and F. Zacek. "A Method of Formation of Thin Oxide Films on Silicon in a Microwave Magnetoactive Oxygen Plasma." *J. Phys. D: Appl. Phys.* 8 (1975): L195.
4. K. Suzuki, S. Okudaira, N. Sakudo, and I. Kanomata. "Microwave Plasma Etching." *Jpn. J. Appl. Phys.* 16 (1977): 1979.
5. S. Matsuo and M. Kiuchi. "Low Temperature Chemical Vapor Deposition Method Utilizing an Electron Cyclotron Resonance Plasma." *Jpn. J. Appl. Phys.* 22 (1983): L210.
6. H. Kawarada, K. S. Mar, and A. Hiraki. "Large Area Chemical Vapour Deposition of Diamond Particles and Films Using Magneto-Microwave Plasma." *Jpn. J. Appl. Phys.* 26 (1987): L1032.
7. Y. H. Shing and S. F. Pool. "Electron Cyclotron Resonance Deposition of Diamond-like Films." Vacuum 41,no. 4-6 (1990):1368.
8. O. A. Popov and H. Waldron. "Electron Cyclotron Resonance Plasma Stream Source for Plasma Enhanced Chemical Vapor Deposition." J. Vac. Sci. Technol. A 7 (1989): 914.
9. S. Y. Shapoval, V. T. Petrashov, O. A. Popov, A. O. Westner, M. D. Yoder, Jr., and C. K. C. Lok. "Cubic Boron Nitride Films Deposited by Electron Cyclotron Resonance Plasma." Appl. Phys. Lett. 57 (1990): 1885.
10. Y. Tanaka, Y. Kunitsugu, I. Suemune, Y. Honda, Y. Kan, and M. Yamanishi. "Low-Temperature GaAs Epitaxial Growth using Electron-cyclotron-resonance/ Metalorganic-Molecular-Beam Epitaxy." J. Appl. Phys. 64 (1988): 2778.
11. T. Ono, H. Nishimura, M. Shimada, and S. Matsuo. "Electron Cyclotron Resonance Plasma Source for Conductive Film Deposition." *J. Vac. Sci. Technol. A* 12 (1994): 1281.

12. W. Scharff, K. Hammer, B. Eibisch, O. Stenzel, S. Roth, and T. Frauenheim. "Deposition of Hydrogenated Amorphous Carbon Films by an ECR Microwave Plasma." *Phys. Stat. Sol. A* 112 (1989): 667.
13. J. Wei, H. Kawarada, J. Suzuki, J. S. Ma, and A. Hiraki. "Effects of Plasma Potential on Diamond Deposition at Low Pressure using Magneto-Microwave Plasma Chemical Vapor Deposition." *Jpn. J. Appl. Phys.* 30 (1991): 1279.
14. M. Kanoh, K. Suzuki, J. Tonotani, K. Aoki, and M. Yamage. "Inductively Coupled Plasma Source with Internal Straight Antenna." *Jpn. J. Appl. Phys.* 40 (2001): 5419.
15. K. Nakamura, Y. Kuwashita, H. Sugai. "New Inductive RF Discharge using an Internal Metal Antenna." *Jpn. J. Appl. Phys.* 34 (1995): L 1686.
16. S. M. Gorbatkin and L. A. Berry. "Contamination by Sputtering in Mirror Field Electron Cyclotron Resonance Microwave Plasma Sources." *J. Vac. Sci. Technol. A* 10 (1992): 3104.
17. M. Lieberman and A. Lichtenberg. *Principles of Plasma Discharges and Materials Processing*, 2nd ed. Hoboken, NJ: John Wiley and Sons, 2005.
18. R. A. Dandl. "Coaxial Microwave Applicator for an Electron Cyclotron Resonance Plasma Source." US Patent No. 5,707,452. San Marcos, CA, 1998.
19. J. E. Foster. "Very Large Area/Volume Microwave ECR Plasma and Ion Source." US Patent No. 7,493,869 B1. Strongsville, OH, 2009.
20. J. Mai, et. al. "ECR Plasma Source." US Patent No. 0242131 A1. New York, NY, 2009.
21. F. Chen. Introduction to Plasma Physics and Controlled Fusion, 2nd ed. New York, NY: Plenum Press, 1984.
22. R. J. Goldston and P. H. Rutherford. Introduction to Plasma Physics. Bristol: Institute of Physics Publishing, 1995.
23. R. d'Agostino. Plasma Deposition, Treatment, and Etching of Polymers. San Diego, CA: Academic Press, 1990.
24. O. A. Popov. "Effects of magnetic field and microwave power on electron cyclotron resonance-type plasma characteristics." *J. Vac. Sci. Technol. A* 9 (1991): 711.
25. J. E. Stevens. "Electron Cyclotron Resonance Plasma Sources." In *High Density Plasma Sources: Design, Physics and Performance*, ed. O. A. Popov. Park Ridge, NJ: Noyes Publications, 1995.
26. P. Tipler and G. Mosca. *Physics for Scientists and Engineers*. 5th ed. New York: W. H. Freeman and Co., 2004, p. 836.
27. T. S. Bastian. "Notes on Electromagnetic Waves in a Plasma." Last modified Dec. 4 2005. Accessed Oct. 5, 2017. https://hesperia.gsfc.nasa.gov/summerschool/lectures/bastian/Notes_on_Waves.pdf.
28. D. W. Mahaffey. "Microwave Propagation through a Plasma in a Magnetic Field." *Phys. Rev.* 129, no. 4 (1963): 1481.

29. O. A. Popov. "Electron Cyclotron Resonance Plasma Sources and Their Use in Plasma-Assisted Chemical Vapor Deposition of Thin Films." In *Physics of Thin Films: Plasma Sources for Thin Film Deposition and Etching* 18, ed. M. H. Francombe and J. L. Vossen. USA: Academic Press, 1994.
30. K. G. Budden. *Radio Waves in the Ionosphere*. Cambridge, UK: Cambridge University Press, 1966.
31. J. Asmussen. "Electron Cyclotron Resonance Microwave Discharges for Etching and Thin Film Deposition." *J. Vac. Sci. Technol. A* 7 (1989): 883.
32. "Plasma Physics." Accessed Oct. 16, 2017. http://www.physics.usyd.edu.au/~mmmb/plasma/Chapter5.pdf.
33. G. Dilecce. "Probe Diagnostics of Plasmas." In *Plasma Technology: Fundamentals and Applications*, ed. M. Capitelli and C. Gorse. New York: Plenum Press, 1992, p. 29.
34. "Langmuir's Probe." Accessed Oct. 17, 2017. http://www.physics.csbsju.edu/370/langmuir_probe.pdf.
35. L. Conde. "An Introduction to Langmuir Probe Diagnostics of Plasmas." Last modified May 28, 2011. Accessed Oct.17, 2017. http://plasmalab.aero.upm.es/~lcl/PlasmaProbes/Probes-2010-2.pdf.
36. R. L. Merlino. "Understanding Langmuir Probe Current-Voltage Characteristics." *Am. J. Phys.* 75 (2007): 1078.
37. N. Hershkowitz. "How Langmuir Probes Work." In *Plasma Diagnostics, Discharge Parameters and Chemistry*, ed. by O. Auciello and D. L. Flamm. Boston: Academic Press, 1989, p. 118.
38. F. Chen. "Langmuir Probe Diagnostics." Lecture presented at the annual IEEE International Conference on Plasma Science , Jeju, Korea, June 5, 2003.
39. M. Mehdizadeh. *Microwave/RF Applicators and Probes for Material Heating, Sensing, and Plasma Generation*, 2nd ed. Oxford: Elsevier Inc., 2015, p. 348.
40. S. Pathak. "Finite Difference Time Domain (FDTD) Simulation of Waveguide as a Heating Applicator." Paper presented at the International Conference on Antenna Technologies, Ahmedabad, February 23-24, 2005.
41. "Antenna Fundamentals: Propagation." A Royal Canadian Air Force Training Film. Accessed Oct. 27, 2017. https://www.youtube.com/watch?v=7bDyA5t1ldU.
42. "Dipole Antenna." Accessed May 10, 2018. https://upload.wikimedia.org/wikipedia/commons/d/da/Felder_um_Dipol.jpg.
43. S. Silver. Microwave Antenna Theory and Design. London: Peter Peregrinus Ltd., 1984, p. 37.

44. R. A. Scholl. "Forward and Reflected Powers: What Do They Mean?" Last modified 1998. Accessed Oct. 27, 2017. https://www.oz7amg.dk/antenneforedrag/advanced_energy_swr.pdf.
45. R. Wolfson. *Essential University Physics*, 2nd ed. Pearson Education, 2011.
46. P. K. Shufflebotham and D. J. Thomson. "Diagnostic Techniques for Plasma Stability in Electron Cyclotron Resonance Plasma Processing." *J. Vac. Sci. Technol. A* 8 (1990): 3713.
47. K. Cheng and D. J. Edwards. *Millimetre Wave Antennas for Gigabit Wireless Communcations*. UK: Wiley, 2008, p. 115.
48. K. Suzuki, k. Nakamura, H. Ohkubo, and H. Sugai. "Power Transfer Efficiency and Mode Jump in an Inductive RF discharge." *Plasma Sources Sci. Technol.* 7 (1998): 13.
49. K. Kishore. *Antenna and Wave Propagation*. New Delhi: I. K. Int'l Publishing House Pvt. Ltd., 2009, p. 42.
50. A. D. MacDonald. *Microwave Breakdown in Gases*. New York: Wiley, 1966.
51. E. S. Aydil, J. A. Gregus, and R. A. Gottscho. "Electron Cylotron Resonance Plasma Reactor for Cryogneic Etching." *Rev. Sci. Instrum.* 64 (1993): 3572.
52. N. Itagaki, Y. Ueda, N. Ishii, and Y. Kawai. "Production of Low Electron Temperature ECR Plasma for Thin Film Depostion." *Surf. Coat Technol.* 142-144 (2001): 546.
53. W. Scharff, K. Hammer, B. Eibisch, O. Stenzel, S. Roth, and T. Frauenheim. "Deposition of Hydrogenated Amorphous Carbon Films by an ECR Microwave Plasma." *Phys. Stat. Sol. A* 112 (1989): 667.
54. S. C. Kuo and E. E. Kunhardt. "Deposition of Diamond-like Carbon Film using Electron Cyclotron Resonance Plasma." *Appl. Phys. Lett.* 59 (1991): 2532.
55. C. Sun, W. J. Zhang, C. S. Lee, I. Bello, and S. T. Lee. "Nucleation of Diamond Films by ECR-enhanced Microwave Plasma Chemical Vapor Deposition." *Diamond Relat. Mater.* 8 (1999): 1410.
56. S. F. Yoon, K. H. Tan, Rusli, J. Ahn, and Q. F. Huang. "Effect of Microwave Power on Diamond-like Carbon Films Deposited using Electron Cyclotron Resonance Chemical Vapor Deposition." *Diamond Relat. Mater.* 9 (2000): 2024.
57. C. Y. Cheng and K. Teii. "Control of the Growth Regimes of Nanodiamond and Nanographite in Microwave Plasmas." *IEEE Trans. Plasma Sci.* 40 (2012): 1783.
58. J. C. Angus and C. C. Hayman. "Low-pressure, Metastable Growth of Diamond and Diamondlike Phases." *Science* 241 (1988): 913.
59. D. M. Gruen, C. D. Zuiker, A. R. Krauss, and X. Pan. "Carbon dimer, C2, as a Growth Species for Diamond Films from Methane/Hydrogen/Argon Microwave Plasmas." *J. Vac. Sci. Technol. A* 13 (1995): 1628.
60. S. J. Stuart, P. S. Krstic, T. A. Embry, and C. O. Reinhold. "Methane Production by Deuterium Impact at Carbon Surfaces." *Nucl. Instrum. Methods Phys. Res. B* 255 (2007): 202.

61. J. Robertson. "Diamond-like Amorphous Carbon." *Mater. Sci. Eng. R.* 37 (2002): 129.
62. C. Hopf, A. von Keudell, and W. Jacob. "Chemical Sputtering of Hydrocarbon Films by Low-energy Ar^+ Ion and H atom Impact." *Nucl. Fusion* 42 (2002): L27.
63. E. Salonen, K. Nordlund, J. Keinonen, and C. H. Wu. "Bond-breaking Mechanism of Sputtering." *Europhys. Lett.* 52 (2000): 504.
64. "Models RGA100, RGA200, and RGA300 Residual Gas Analyzer." Last modified May, 2009. Accessed Oct. 24, 2017. http://www.thinksrs.com/downloads/pdfs/manuals/RGAm.pdf.
65. R. E. March and R. J. Hughes. "Quadrupole Storage Mass Spectrometry". In Chemical Analysis: A Series of Monographs on Analytical Chemistry and its Applications 102. New York: Wiley, 1989.
66. "Gas Chromatography Mass Spectrometry." Accessed Oct. 23, 2017. http://www.bris.ac.uk/nerclsmsf/techniques/gcms.html.
67. H. P. Meyers. *Introductory Solid State Physics*. London: Taylor and Francis, 1990.
68. J. Torres, A. Perio, R. Pantel, Y. Campidelli, and F. Arnaud D'Avitaya. "Growth of Thin Films of Refractory Silicides on Si(100) in Ultrahigh Vacuum." *Thin Soild Films* 126 (1985): 233.
69. J. Roth. "Chemical Erosion of Carbon Based Materials in Fusion Devices." *J. Nucl. Mater.* 266 (1999): 51.
70. M. A. Elliott, P. W. May, J. Petherbridge, S. M. Leeds, M. N. R. Ashfold, and W. N. Wang. "Optical Emission Spectroscopic Studies of Microwave Enhanced Diamond CVD using CH_4/CO_2 Plasmas." *Diamond Relat. Mater.* 9 (2000): 311.
71. F. J. Gordillo-Vazquez and J. M. Albella. "Distinct Nonequilibrium Plasma Chemistry of C_2 Affecting the Synthesis of Nanodiamond Thin Films from $C_2H_2(1\%)/H_2$/Ar-rich Plasmas." *J. Appl. Phys.* 94 (2003): 6085.

Appendix

Conversion of PEF to PPM image file

1. Put images in a folder on desktop
2. Put *dcraw.exe* in the folder
3. Rename the folder to "images" (by preference, there should be no space)
4. Open *Command Prompt*
5. Enter "cd desktop/images"
6. Enter "dcraw -v -w -W -o 0 *.pef"

Mean luminosity calculation

1. Check "Notes on using the *photo.m* Octave script" in the following section
2. Put *photo.m* script in the images folder
3. Open *Octave CLI*
4. Enter "cd desktop/images"
5. Enter "photo;"

Notes on using the *photo.m* Octave script

1. Replace X Y L W in the "rect=[X Y L W]" line with the values given by,

$$X = X'\frac{x}{x'} \qquad Y = Y'\frac{y}{y'} \qquad L = X'\frac{l}{x'} \qquad W = Y'\frac{w}{y'}$$

where x, x', y, y', l and w are the measurements of the dimensions shown in Fig. A using the *Pixel Ruler* application. X' and Y' are the number of pixels (dimension) along the length and width of the photo, respectively.

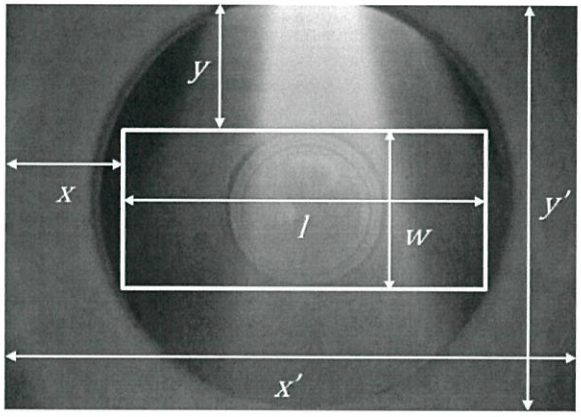

Figure A. Dimensions needed to obtain X, Y, L and W values

2. The script only works to image files with filename from numbers "1" to "90".
3. The script has two kinds of csv output files: the luminosity histograms and the mean luminosity.
4. The luminosity histograms files contain two-column data; the gray value and the number of pixels that has the corresponding gray value in the first and second column, respectively.
5. The mean luminosity file also contains two-column data; the filename of the image and the mean luminosity of that image in the first and second column, respectively.

The *photo.m* Octave script is as follows:

```
1;
clear;
pkg load image;
rect = [X Y L W];
for j=1:90
    cnt = mat2str(j, 2);
    si = strcat(cnt, ".ppm");
    chk = exist(si);
    if (chk != 0)
        I = imread(si);
        I = rgb2gray(I);
        I = imcrop(I, rect);
        [counts, x] = imhist(I);
        H = [x counts];
        so = strcat("hst_", cnt);
        csvwrite(so, H);
        v(end + 1) = mean2(I);
        a(end + 1) = j;
    endif;
endfor;
p = [a; v];
p = transpose(p);
csvwrite("batch_mean", p);
```